Master of Science Thesis:

— **Nonlinear Dynamics** —

Forced Oscillators

A Detailed Numerical Bifurcation Analysis

Supervisor: Erik Mosekilde

Klaus Baggesen Hilger
c928518

Dan Seriano Luciani
c928979

August 20, 1998

Center for Chaos and Turbulence Studies
Department of Physics
The Technical University of Denmark

Preface

This report is a Master Thesis in the field of nonlinear dynamics and chaos. The work has been carried out over a six month period from the 16th of February to the 20th of August at the Center for Chaos and Turbulence Studies, Department of Physics at the Technical University of Denmark.

We would like to extend our gratitude to Dr. Scient. Erik Mosekilde for supervising the project. We thank Thomas B. Markussen for excellent support on the Unix/Linux systems, and Morten D. Andersen and Niklas Carlsson for creating the ManicPackage for LaTeX. Also, a big thank you to Martin Bees, Peter Andresen, and Jacob Laugesen along with the rest of the Physics Department for creating a friendly atmosphere. Finally, we thank our families, girlfriends, and the pizzabar *Bon Appetit* for supporting us during the last part of the project.

Lyngby, August 20, 1998.

Klaus B Hilger
C928518

Dan S Luciani
C928979

Contents

List of Figures

CHAPTER 1

Introduction

Oscillating behaviour occurs on a wide range of spatial and temporal scales, from the self-sustained pulsatile secretion of hormones to the periodic variations of the seasons. In reality oscillating systems seldom function independently of each other. The ways in which oscillators interact, and the analysis of the resulting dynamics are thus interdisciplinary subjects of great interest.
One characteristic of an oscillating system is the period of the natural movement. When such oscillators interact, the resulting motion may be periodic but often has a characteristic frequency other than the one observed for the independent systems. The coupling of oscillators may also give rise to non-periodic or even chaotic behaviour.

Single oscillators subject to external periodic perturbations constitute an important sub-class of coupled self-oscillating systems, often encountered in the fields of biology, physics, chemistry and physiology. The existence of self-sustained oscillations usually depends on the value of one or more of the system parameters. When an oscillator is perturbed (forced), it is most commonly done by a periodic variation of such a parameter, with an amplitude and a frequency subject to external control.
In principle, such a forced oscillator can be viewed as two coupled oscillators, one of which (the external perturbation) is unaffected by the other. Subsequently, the analysis of a forced oscillator may also lead to a better understanding of the more general class of coupled oscillators.

Systems of forced oscillators, which have previously been examined, either experimentally or theoretically, include the forced continuously stirred tank reactor (CSTR) [Kevrekidis et al., 1986; Vance et al. (II), 1989], the forced

Brusselator [Knudsen et al., 1991], predator-prey systems in periodically operated chemostats [Pavlou and Kevrekidis, 1992], periodically forced Gunn diodes [Mosekilde et al., 1990], and the forcing of self-sustained oscillations in a glucose/insulin feedback system [Sturis et al., 1995].

The essence of the behaviour of such systems can often be represented by means of non-linear mathematical models. Consequently, numerical and analytical analyses of these models provide not only a theoretical foundation for the explanation of experimental observations, but also the opportunity to analyze aspects which are difficult or maybe even impossible to examine in practical experiments.

In this thesis, a mathematical model of a forced oscillator is constructed and subjected to a detailed numerical bifurcation analysis. This is done, not only to examine a particular system, but with the added intent of elucidating features common to the non-linear dynamics of the class of periodically perturbed oscillators.

First the terms and theory relevant for our examinations are introduced. This includes a discussion of various bifurcation scenarios in which curves of codimension one bifurcations connect.
After this the model is constructed. By modifying the generic normal form for a Hopf bifurcation, we obtain a system exhibiting self-sustained oscillations. These exist in a section of the parameter space enclosed by two distinct regions of equilibrium solutions. This unperturbed system is analyzed and subsequently exposed to a periodic forcing. Our choice of system parameters determine which regions are visited during one period of the forcing.

The effects of the forcing are examined by means of various numerical tools, which we have implemented and continuously modified during the course of the project. Before presenting the results, we give qualitative descriptions of these tools and the other methods employed in the bifurcation analysis.

Our results show two dimensional bifurcation structures organized into regions, so-called tongues, where the system responds in a periodic manner to the forcing. Inside this skeletal structure we find a wide variety of nonlinear phenomena, including quasiperiodic and chaotic states. The observations are presented with respect to the tongues with which they are associated.

In the last section we examine the effect of varying the initial periodic state of the system. The extent of the various tongues is dictated by the choice of this state. If forcing around a natural equilibrium state of the autonomous system, the tongue structure is not observed. In these cases the system exhibits different types of response, depending on the equilibrium region in which the initial state is located.

Finally, we briefly summarize our results.

CHAPTER 2

General Theory

In order to create a basis for further discussions some of the main notions and definitions are introduced. Hence, part of the motivation for this chapter is to provide a vocabulary for the later presentation of our nonlinear analysis. Discussion of topics in nonlinear dynamics can be found in, for example, [Ott, 1994] [Guckenheimer and Holmes, 1986], and [Nayfeh and Balachandran, 1995].

2.1 Periodically Forced Oscillators

A nonlinear oscillator subjected to periodic forcing may be *entrained* to oscillate with a period that is a multiple of the forcing period. Let ω_0 be the natural frequency of the oscillations in the system without the forcing and ω_F the forcing frequency. For small values of the forcing amplitude, A, entrainment occurs in wedge-shaped regions in the (ω_F/ω_0,A) parameter plane. Outside the entrainment regions the oscillatory system responds in a quasiperiodic manner. Increasing the amplitude of the forcing causes many different phenomena to occur including overlap and closing of entrainment regions, and various routes to chaos. When the amplitude of the forcing is sufficiently large, the entrainment will be the simplest possible: a one-to-one synchronization with the forcing frequency.

The later study shall be dealing with a subclass of forced oscillators, in which the system is forced across a first-order Hopf bifurcation. Consider an autonomous system described by an N-dimensional system of coupled, nonlinear, ordinary differential equations:

$$\frac{d\mathbf{x}}{dt} = \dot{\mathbf{x}} = \mathbf{F}(\mathbf{x}(t), \mathbf{M}), \qquad \mathbf{x} \in \mathbb{R}^N,\ t \in \mathbb{R},\ \mathbf{M} \in \mathbb{R}^P. \tag{2.1}$$

$\mathbf{x}$ is a vector of N state variables of the system, t is time, and $\mathbf{M}$ is a vector of P system parameters. $\mathbf{F}$ represents the model equations describing the system rates, i.e. the nonlinear vector field.
Let $\mathbf{x}_{eq}$ be an equilibrium solution, to Eq. (2.1), that experiences a bifurcation in which it changes stability and gives rise to a periodic solution. Let the bifurcation occur under variation of a *critical parameter* μ at a critical value μ_c. At the bifurcation point the eigenvalues, $\lambda_\pm$, of the equilibrium point cross the imaginary axis transversally as a complex conjugate pair. The conditions for μ_c to be the point at which the system experiences a generic Hopf bifurcation can be expressed by:

$$\mathbf{F}(\mathbf{x}_{eq})|_{\mu_c} = 0, \tag{2.2}$$

$$\lambda_{\pm}|_{\mu_c} = \hat{\lambda} \pm i\omega_H \qquad \hat{\lambda} = 0,\ \omega_H \neq 0,\ \text{and} \tag{2.3}$$

$$\frac{d\,\hat{\lambda}}{d\mu}|_{\mu_c} \neq 0. \tag{2.4}$$

The first of these equations implies that $\mathbf{x}_{eq}$ is an equilibrium point, the second that the point is non-hyperbolic, and the third condition that the eigenvalues cross the imaginary axis transversally (a nonzero speed crossing). When all the conditions are satisfied, a periodic solution of period $2\pi/\omega_H$ is born at $(\mathbf{x}_{eq}, \mu_c)$. Depending on whether the periodic solution is unstable or stable, the bifurcation is classified as sub- or supercritical. This bifurcation is also called a *Poincaré-Andronov-Hopf* bifurcation, giving credit to the analysis done on the bifurcation preceding the work of Hopf.[Nayfeh and Balachandran, 1995]

To force the system the critical parameter is varied sinusoidally. This parameter will also be referred to as the *forcing parameter*. In introducing the forcing, the system becomes nonautonomous, $(\mathbf{F} \rightarrow \mathbf{F}(\mathbf{x}(t), t, \mathbf{M}))$, and the resulting dynamical behavior not only depend on the amplitude and the frequency of the forcing, but also on the location of the so-called *workpoint* - the point around which the forcing parameter is varied. Examinations of these systems include studies in which the workpoint is located on either side of the Hopf bifurcation point μ_c. Whether or not we actually force across the bifurcation depends on the choice of workpoint as well as the amplitude of the forcing.

2.2 The Entrainment Regions

The dynamic of a forced oscillator will typically be studied by means of a stroboscopic map. This is obtained by sampling the solution at regular time intervals corresponding to the period of the forcing. A period-p fixed point in the stroboscopic map is thus a solution with a period of p times the forcing period $T_F = 2\pi/\omega_F$. For a two-dimensional forced system the

periodic solutions are characterized by two frequencies - i.e. the natural, ω_N, and the forcing frequency, ω_F. When the ratio $\omega_N/\omega_F = q/p$ is a rational number, with q and p integers, the system exhibits a periodic solution that oscillates in $p:q$ synchronization with the forcing.

Fig. 2.1 illustrates examples of different $p:q$ periodic solutions of a two-dimensional nonautonomous system that has synchronized with its forcing. Time-series of 2:1 and 2:3 resonance solutions are portrayed. The motion of the solutions in the state space is presented in Fig. 2.2.

When the frequencies are incommensurate the ratio ω_N/ω_F is irrational, indicating a quasiperiodic solution. Such a motion can be visualized as a motion on the surface of a two-torus. The quasiperiodic orbit never closes on itself and the surface of the torus is densely covered with the trajectory as time goes to infinity. The *rotation number* is determined by $\rho = \omega_N/\omega_F$. It corresponds to the number of times a periodic or a quasiperiodic motion winds around the meridian of the torus per period of the forcing. Note that the value of ρ is equivalent to q/p.

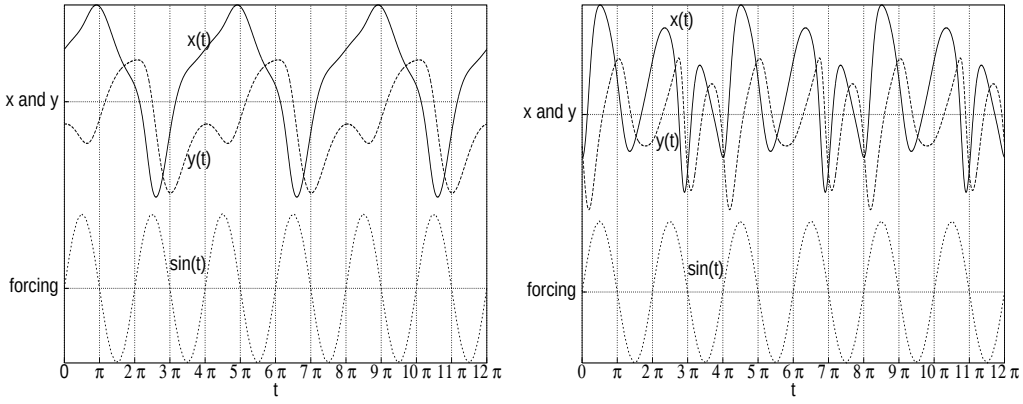

Figure 2.1 The left and the right subfigures illustrate the 2:1, and the 2:3 solutions respectively. Notice that the solutions have q peaks over p periods of the forcing.

As an example of a quasiperiodic solution Fig. 2.3 is included. The figure

illustrates both the time evolution of the state variables and a phase diagram of a quasiperiodic solution. ρ is determined to be $1.5248 \simeq 3/2$ rotations per period of the forcing so the quasiperiodic solution is close to a 3:2 periodic solution. Notice how the quasiperiodic motion on a two-torus is reduced to discrete points in the state space, and how, as time passes, an infinite set of points will form an invariant circle.
Note: It is not possible to discriminate numerically between a quasi-periodic attractor and a periodic attractor of very high period.

Entrainment regions will be referred to as $p : q$ *resonance horns* or *Arnol'd tongues*. The tongues are often presented in an *excitation diagram*, thus indicating the loci of transitions between qualitatively different types of dynamic behavior in $(\omega_F/\omega_0, A)$ parameter space. The transitions are generic local bifurcation curves of codimension one (CD1), coming together in codimension two (CD2) bifurcation points.

At zero amplitude of the forcing $\omega_N = \omega_0$. Thus, the tongues will emanate from points where $A = 0$ and $\omega_F/\omega_N = \omega_F/\omega_0$ is rational and broaden as

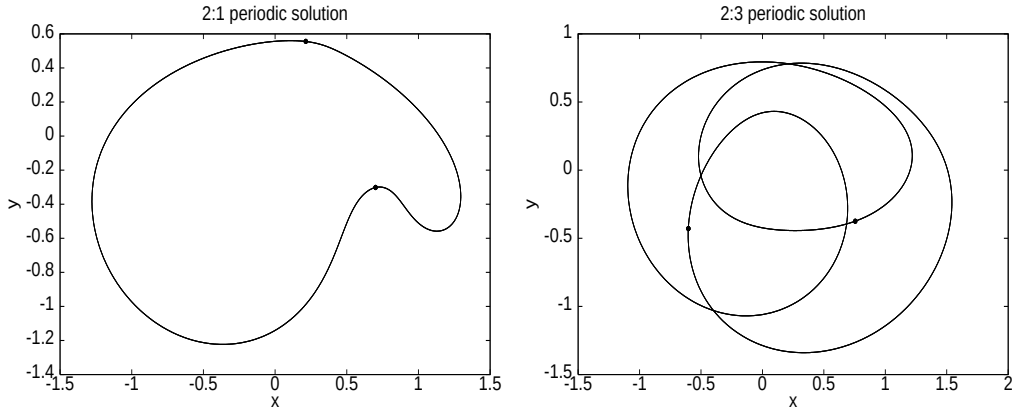

Figure 2.2 The left and the right subfigures illustrate the 2:1 and the 2:3 solutions respectively. The points on the solution are the points located as fixed points in the stroboscopic mapping.

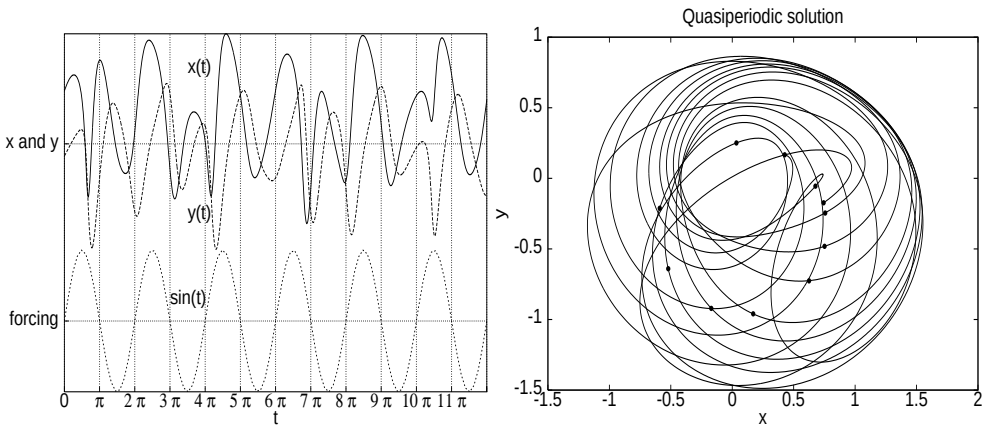

Figure 2.3 To the left is portrayed the time-series of a quasiperiodic solution. The evolution of the solution in the state space is illustrated to the right. The points on the solution trajectory result from the stroboscopic mapping and as time passes they will constitute an invariant circle.

the amplitude is increased. The rotation number has been calculated as a function of the forcing frequency and illustrated in Fig. 2.4. The figure corresponds to a scenario where the workpoint is within a region in which the autonomous system exhibits oscillations. The forcing amplitude is constant while low enough not to bring the forcing parameter across the Hopf bifurcation. The horizontal steps correspond to regions containing periodically entrained solutions, and between these steps the motion may be of a higher order resonance or quasiperiodic. Because there are an infinite number of rational numbers distributed between any two rational numbers, a similar structure is observed at all scales. This is, however, impossible to prove numerically as the digital computers cannot represent irrational numbers. This structure is known as *the Devil's staircase*. The figure corresponds to an amplitude of the forcing at which the entrainment regions do not yet overlap.

The universal manner in which the tongues close at larger amplitudes has been given great attention by e.g. [Kevrekidis et al., 1986], [Norris, 1993],

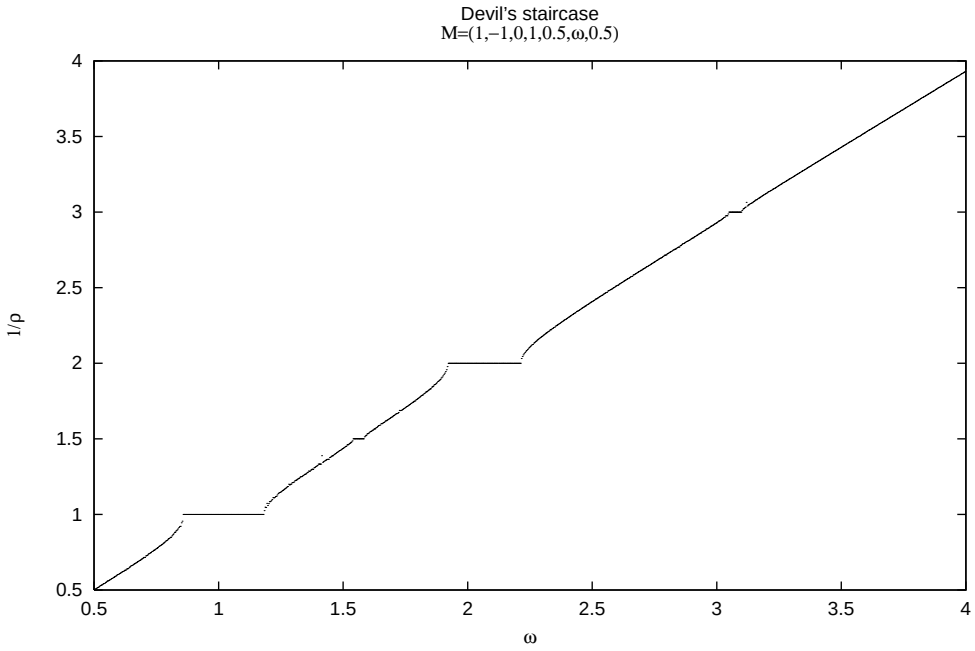

Figure 2.4 A Devil's staircase calculated for the forced oscillator presented in Eq. (3.6) - the parameters are indicated in the vector $\mathbf{M}$ found in the title of this figure. $1/\rho = p/q$ is plotted as a function of $\omega \equiv \omega_F/\omega_0$. Notice that the dominant entrainment regions are the 1:1 and the 2:1 synchronization. The workpoint is located in a region in which the autonomous system oscillates, there is no forcing across the Hopf bifurcation, and no overlap of the entrainment regions.

and [Taylor and Kevrekidis, 1991]. Their examinations are mainly concerned with so-called strong resonances, i.e., the tongues with $p \leq 4$.

The basis of our investigations is a two-dimensional nonautonomous system in which the fixed points of the stroboscopic map possess two Floquet mul-

Periodic Solution Curves	
Type	*Description*
-Np	Unstable node of period p. $\lambda_{1,2}$ are real and $\|\lambda_{1,2}\| > 1$.
+Np	Stable node of period p. $\lambda_{1,2}$ are real and $\|\lambda_{1,2}\| < 1$.
-Fp	Unstable focus of period p. $\lambda_{1,2}$ are complex conjugates and $\|\lambda_{1,2}\| > 1$.
+Fp	Stable focus of period p. $\lambda_{1,2}$ are complex conjugates and $\|\lambda_{1,2}\| < 1$.
Sp	Saddle of period p. $\lambda_{1,2}$ are real and $\lambda_1 < -1, \lambda_2 > 1$.

Table 2.1 Five distinct classes of periodic solutions. The type indicates the nature of the associated fixed point as determined by the Floquet multipliers.

tipliers λ_1 and λ_2. These eigenvalues may be real or complex conjugates, and their nature and magnitude classify the periodic solutions into the categories presented in Table 2.1.When referring to the eigenvalues of a periodic solution they are the Floquet multipliers of a corresponding fixed point in the stroboscopic map. The periodic solutions are classified corresponding to the type of the associated fixed points and can, therefore, be either stable or unstable node (±N), focus (±F), or saddle (S) solutions.

Where a solution changes from a node to a focus or vice versa so-called *equal-eigenvalues* (EE) points are founds. It is possible to trace these points and construct curves in the parameter space at which the eigenvalues of a solution changes from real to complex conjugates. In Table 2.2 the curves are classified into two groups corresponding to whether a stable or unstable node/focus is involved.

The boundaries of the entrainment regions in an excitation diagram are local bifurcations of the periodic solutions (fixed points of the associated map). All these bifurcations are structurally unstable but may be of different codi-

Equal-Eigenvalues Curves	
Type	*Description*
EEp+	Transition point for a stable period-p solution changing between +Np and +Fp. $\lambda_{1,2}$ are real and $\lambda_1 = \lambda_2, \|\lambda_{1,2}\| < 1$.
EEp-	Transition point for an unstable period-p solution changing between -Np and -Fp. $\lambda_{1,2}$ are real and $\lambda_1 = \lambda_2, \|\lambda_{1,2}\| > 1$.

Table 2.2 There are two types of equal-eigenvalues curves. They are associated with the transitions, in which a fixed point changes its nature as its Floquet multipliers change from being real to complex conjugates or vice versa.

mension. When a vector field is structurally unstable to a single bifurcation parameter, the bifurcation is of codimension one. Similarly, if two parameters need to have unique values the bifurcation is of codimension two and so forth. The local bifurcation curves can be considered a result of the interference of the forcing with the Hopf bifurcation of the underlying autonomous system [Kevrekidis et al., 1986].

2.3 Local Bifurcations of Periodic Solutions

The possible local generic bifurcations found in our system are: 1) the saddle-node bifurcation (SN) also referred to as cyclic fold, tangent bifurcation, or turning point. 2) second-order Hopf bifurcation also called Neimark-Sacker bifurcation or torus bifurcation (T), and 3) the flip/period-doubling bifurcation (PD). The bifurcation curves will be referred to by the abbreviation. Where relevant it will also be indicated whether the bifurcations are sub- or supercritical along with the period of the solutions involved. Thus, the one-parameter local bifurcation curves are classified into five distinct groups as represented in Table 2.3.

The codimension one bifurcation curves connect in codimension two sin-

Codimension One Bifurcations	
Type	*Description*
SNp+	Saddle to stable node bifurcation of a period-p solution. $\lambda_{1,2}$ are real and $\lambda_1 = 1 \vee \lambda_2 = 1$.
SNp-	Saddle to unstable node bifurcation of a period-p solution. $\lambda_{1,2}$ are real and $\lambda_1 = 1 \vee \lambda_2 = 1$.
Tp	Supercritical torus bifurcation of a period-p solution. $\lambda_{1,2}$ are complex conjugate and $\|\lambda_{1,2}\| = 1$.
PDi,j+	Supercritical period-doubling bifurcation. A period-i solution loses stability while doubling to a period-j solution. The period-i solution has the eigenvalues $\lambda_{1,2}$ that are real and $\lambda_1 = -1 \vee \lambda_2 = -1$. The period-j solution has the eigenvalues $\tilde{\lambda}_{1,2}$ that are real and $\tilde{\lambda}_1 = 1 \vee \tilde{\lambda}_2 = 1$.
PDi,j-	Subcritical period-doubling bifurcation. A period-i solution gains stability while doubling to a solution of period-j. The period-i solution has the eigenvalues $\lambda_{1,2}$ that are real and $\lambda_1 = -1 \vee \lambda_2 = -1$. The period-j solution has the eigenvalues $\tilde{\lambda}_{1,2}$ that are real and $\tilde{\lambda}_1 = 1 \vee \tilde{\lambda}_2 = 1$.

Table 2.3 Local bifurcations of the periodic solutions. The type indicates the nature of the bifurcation. The system exhibits all generic codimension one bifurcations.

Codimension Two Bifurcations	
Type	*Description*
SN-SN	A *cusp or wedge point* where two SNi curves connect. At the point, the period-i solution has two real eigenvalues $\lambda_{1,2}$ and $\lambda_1 = 1 \vee \lambda_2 = 1$.
SN-PD	A *degenerate period-doubling point* (DPD) in which an SNj bifurcation curve connects to a PDi,j curve. The point marks a change of the PD curve from sub- to supercritical. The period-i solution has two real eigenvalues $\lambda_{1,2}$ and $\lambda_1 = -1 \vee \lambda_2 = -1$. The period-j solution also has two eigenvalues $\tilde{\lambda}_{1,2}$ that are real and $\tilde{\lambda}_1 = 1 \vee \tilde{\lambda}_2 = 1$.
T-SN	A *Takens-Bogdanov point* (TB) where a Ti and an SNi connect. A period-i solution has two real eigenvalues $\lambda_{1,2} = 1$.
T-PD	A Ti and/or a Tj connect to the PDi,j curve at a point in which the PD curve changes from sub- to supercritical. In the point the period-i solution has two real eigenvalues $\lambda_{1,2} = -1$, the period-j solution has two real eigenvalues $\tilde{\lambda}_{1,2} = 1$.

Table 2.4 Different classes of codimension two bifurcations where local codimension one bifurcations connect.

gularities of which different types are presented in Table 2.4. In the table, points are found corresponding to where saddle-node curves connect (SN-SN). Also, points where a saddle-node connects on a period-doubling (SN-PD) or on a torus bifurcation curve (T-SN) are represented. Finally, are represented points (T-PD) in which torus bifurcation curves connect to a period-doubling curve.

The SN-SN codimension two bifurcation occurs in so-called **cusp or wedge points** depending on whether the connecting SN bifurcation curves are tangent to each other or not. The bifurcation SN-SN is depicted in a three-dimensional representation of a two-dimensional bifurcation diagram

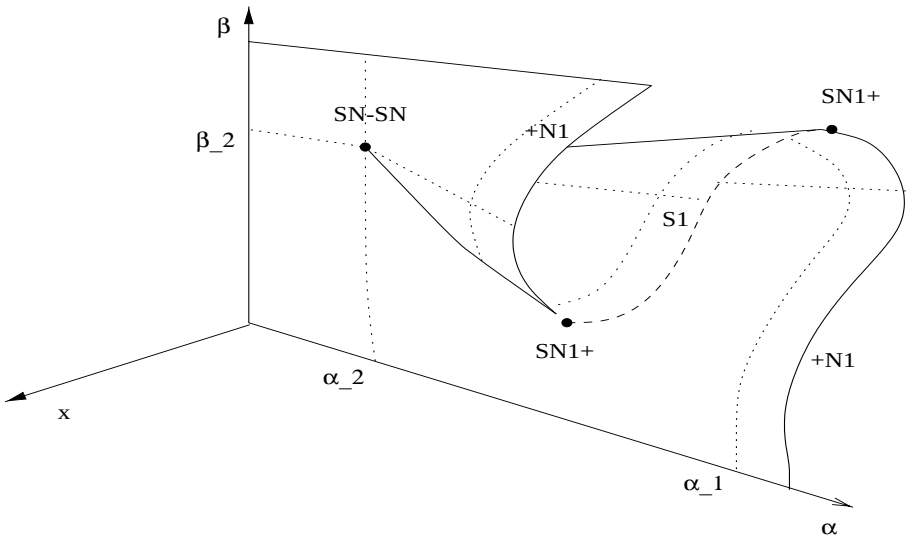

Figure 2.5 The SN-SN bifurcation scenario for a period-one solution. The codimension two point is located at (α_2, β_2). Any small perturbation of the control parameters will destroy it. For $\alpha = \alpha_1 > \alpha_2$ the cusp is replaced by two SN1+ bifurcations. The cusp scenario looks like a folded sheet where the folds are the SN1+ bifurcations.

in Fig. 2.5
Only when the two bifurcation parameters α and β are exactly at the point (α_2, β_2) is the CD2 bifurcation found. A scan through the bifurcation diagram in Fig. 2.5 at constant $\beta = \beta_2$, varying α through the SN-SN point, is presented in Fig. 2.6. As seen from this one-dimensional bifurcation diagram, a node changes stability in the bifurcation point and in the process two new nodes emerge.

Fig. 2.7 depicts a bifurcation diagram corresponding to scans in the control parameter β at constant values of α. In Subfigure 1 is presented a scan performed at $\alpha = \alpha_1$, passing near the cusp point, and in Subfigure 2 a scan

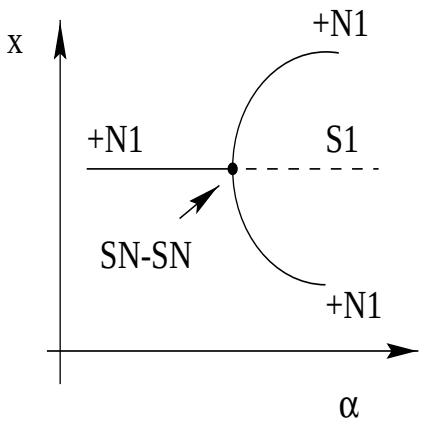

Figure 2.6
A scan through the SN-SN bifurcation point. Note how a stable node loses stability in passing the point and becomes a saddle solution. The saddle is the separator of the basin of attractions for the two new stable nodes that arise through the CD2 bifurcation.

at $\alpha = \alpha_2$ that passes through the codimension two point. Both Fig. 2.6 and Fig. 2.7 can be compared with Fig. 2.5.

In order to ease the understanding of how the solution curves behave near **the SN-PD (Degenerate Period-Doubling - DPD) codimension two bifurcation**, representative bifurcation diagrams are presented. Fig. 2.8 illustrates a possible connection between an SN2- and a PD1,2 curve in the (α, β) parameter plane. Notice that the PD curve changes from sub- to supercritical at the SN-PD point (α_2, β_2).
A scan is illustrated in Subfigure 1 of Fig. 2.9. It passes to the right of the SN-PD point at constant $\alpha = \alpha_1$ for varying β,. In Subfigure 2 a scan through the degenerate period-doubling point is presented.
A period-one solution doubles in a supercritical period-doubling creating a period-two saddle solution that loses stability through a saddle-unstable-node bifurcation. The two bifurcations move closer to each other as the CD2 point is approached, to finally merge and create the degenerate period-doubling point. The scan that passes through the DPD point illustrates how the period-one solution loses stability changing from a saddle to an unstable node for decreasing β. The period-two solution that arises through the degenerate period-doubling point is an unstable node, causing the bifurcation to appear as a subcritical period-doubling of codimension one.
Studies of the bifurcation structure with $\alpha < \alpha_2$, and β as the control pa-

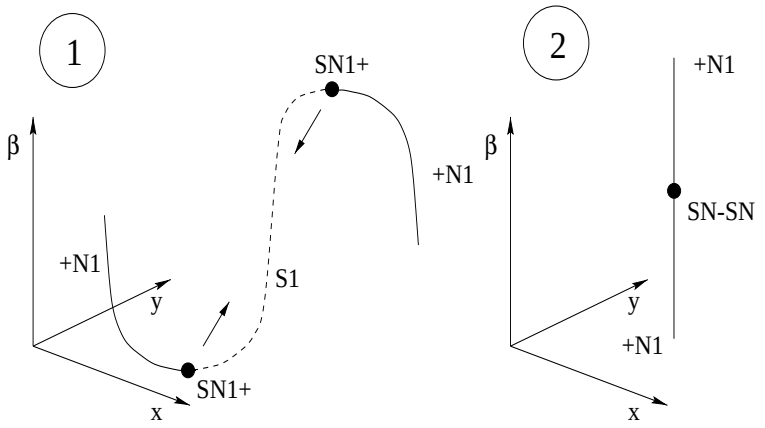

Figure 2.7 Subfigure 1 illustrates a scan through the bifurcation structure for $\alpha = \alpha_1$ near the SN-SN bifurcation. A stable node of period one passes through an SN1+ bifurcation becoming a saddle that bifurcates back to a stable node through another SN1+. The arrows indicate how the local bifurcation points will move relative to each other when α is varied towards α_2, for which the solution passes through the SN-SN bifurcation as depicted in Subfigure 2.

rameter, would result in diagrams similar to Subfigure 2 in Fig. 2.9. The only difference is that the local bifurcation PD1,2- of codimension one replaces the SN-PD codimension two point.
The CD2 bifurcation can be viewed as a destruction or, if you will, a creation point of a saddle-node bifurcation along a period-doubling curve.

Interesting observations can be made concerning the scenario near the DPD points. Let the period-doubling curve be a PDi,j and the saddle-node bifurcation curve an SNj. Consider the case where no other bifurcation curves are involved in a given neighbourhood of the DPD point. Emanating from the SNj curve towards the PD curve are two branches of period-j solutions. One of the period-j solutions is destroyed at the PDi,j bifurcation curve and the other continues past the bifurcation line. Let the period-j solution that crosses the PD curve be a node of the same sign ($\pm$) as indicated on the

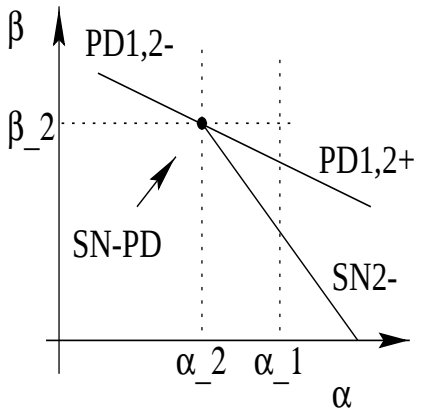

Figure 2.8

Example of a scenario near an SN-PD/DPD codimension two point. A SN2- connects to a PD1,2 bifurcation curve.

SNj± bifurcation curve. Then the PDi,j curve, that is crossed by the period-j solution, **must** be of opposite sign to the SNj curve. Hence, in these cases, when the saddle-node bifurcation curve is either an SNj+ or an SNj-, the period-doubling curve "above" it must be sub- or supercritical respectively. The above can be realized by scanning in a closed loop around the DPD point and tracking the different solutions.

The T-SN bifurcation is also known as the **Takens-Bogdanov (TB)** codimension two bifurcation point. It can be interpreted as a collision of a saddle-node and a torus bifurcation, which destroys the torus bifurcation but leaves the saddle-node behind. On the other hand, the Takens-Bogdanov bifurcation can also be viewed as the birth of a Torus bifurcation from a saddle-node bifurcation. Fig. 2.10 illustrates how a T1 connects to an SN1 bifurcation curve in the (α, β) parameter space. We refer to the similar case in which a connection of an SN2 on a PD1,2 curve caused the PD curve to change from sub- to supercritical. A T1 connects to an SN1 curve at (α_2, β_2) causing it to change from an SN1+ to an SN1-.
The destruction (birth) of a supercritical torus bifurcation T1 of a period-one solution through a Takens-Bogdanov bifurcation is illustrated in Fig. 2.11. The figure corresponds to two scans performed at α_1 and α_2 and can be compared with Fig. 2.10. If no other bifurcations are involved, and when a quasiperiodic attractor exists below the T1 curve, the SN curve above it must be an SN+ curve in the neighbourhood of the TB point.

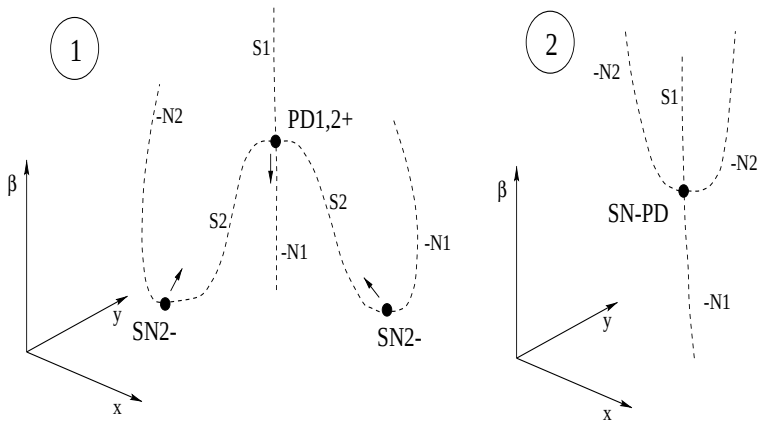

Figure 2.9 Subfigure 1 illustrates the scenario for a scan through the bifurcation structure in Fig. 2.8 for $\alpha = \alpha_1$. Following the S1 solution through a supercritical period-doubling for decreasing β, it doubles to an S2 solution through loss of stability and continues as a -N1. The S2 solution experiences an SN2- bifurcation and becomes a -N2. The arrows indicate how the SN2- and the PD1,2+ bifurcations move relative to each other as α is decreased towards α_2. The scenario for which the solutions pass through the SN-PD/DPD point is illustrated in Subfigure 2. The local CD1 bifurcation points have collided creating the CD2 bifurcation.

The last codimension two point presented is the **T-PD bifurcation**. Looking at an example in which both a T1 and a T2 connect at the same point on a PD1,2 curve, the scenario in (α, β) parameter space is illustrated in Fig. 2.12. The T-PD point is located at the parameter values (α_2, β_2). The connection point is of codimension two as the bifurcations do not occur for the same solution, and marks a change from sub- to supercritical bifurcations on the PD curve. Again, two bifurcation diagrams are presented corresponding to β equal β_1 or β_2 with α as the control parameter.

From Fig. 2.13 it is seen that the T-PD CD2 bifurcation can be perceived as the destruction or birth of torus bifurcations on a period-doubling curve. In

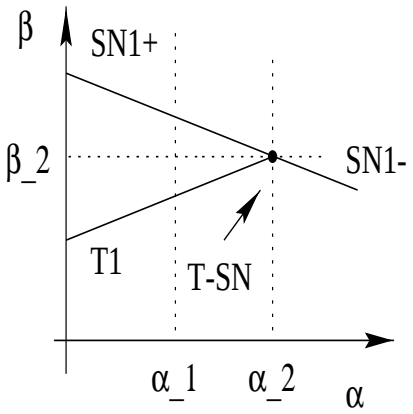

Figure 2.10

Example of a scenario near a T-SN (TB) codimension two point. A T1 connects to an SN1 bifurcation curve.

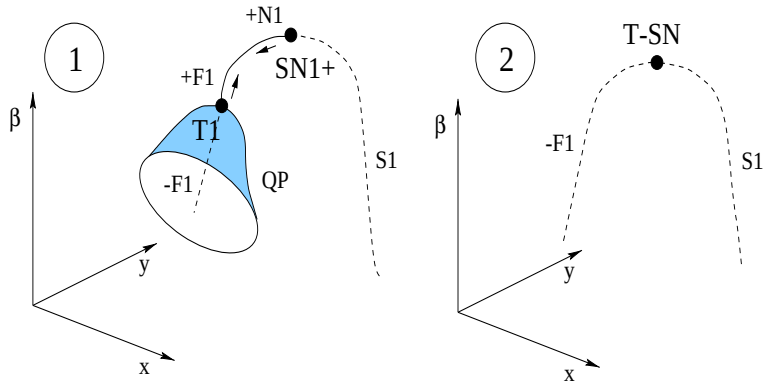

Figure 2.11 Subfigure 1 illustrates a -F1 that passes through a T1 becoming a +F1. It then changes to a +N1 and turns in an SN1+ becoming an S1. The arrows illustrate how the T1 and the SN1+ bifurcations will move closer to each other if α is increased towards α_2. Subfigure 2 illustrates the scenario in which the period-one solution passes through a T-SN / Takens-Bogdanov codimension two point.

Subfigure 1 is shown how a stable focus passes through the torus bifurcation becoming unstable. Thereafter it regains stability to a saddle in a subcritical

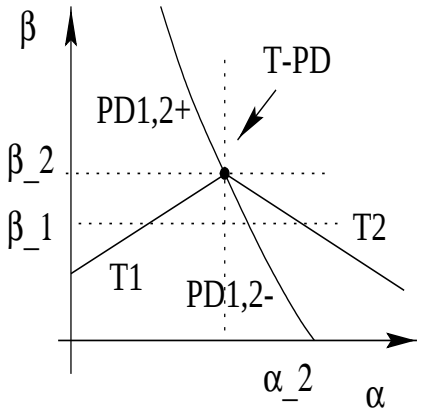

Figure 2.12

The T-PD bifurcation scenario. A T1 and a T2 connects on the PD1,2 curve in the codimension two point T-PD.

period-doubling. This scenario corresponds to a scan near the CD2 point at $\beta = \beta_1$. The solution that emerges through the period-doubling bifurcation is an unstable node which, after changing to an unstable focus, passes through a torus bifurcation and gains stability. On the figure, arrows indicate how the local bifurcation points will move towards each other if β is increased from β_1 to β_2 at which the CD2 point exists.

Scans for $\beta > \beta_2$ result in diagrams similar in structure to Fig. 2.13 - Subfigure 2 but the local bifurcation is now a simple supercritical period-doubling of codimension one instead of the T-PD bifurcation. Consequently, above the codimension two point, a stable node of period-one doubles to a period-two stable node while losing stability. The period-one solution continues as a saddle after the bifurcation.

2.4 Resonant Hopf Bifurcation Points

At certain points in the $(\omega_F/\omega_0, A)$ parameter plane so-called *resonant Hopf bifurcation points* (or just *resonance points*) are located. These are defined as points on a T1 bifurcation curve at which the multipliers of the period-one solution are complex roots of unity. R^p is a resonance point in which $(\lambda_{1,2})^p = 1$.
The p complex roots of unity are $e^{\pm 2\pi i q/p}$ where $q = 1, 2, \cdots, p$. Passing the

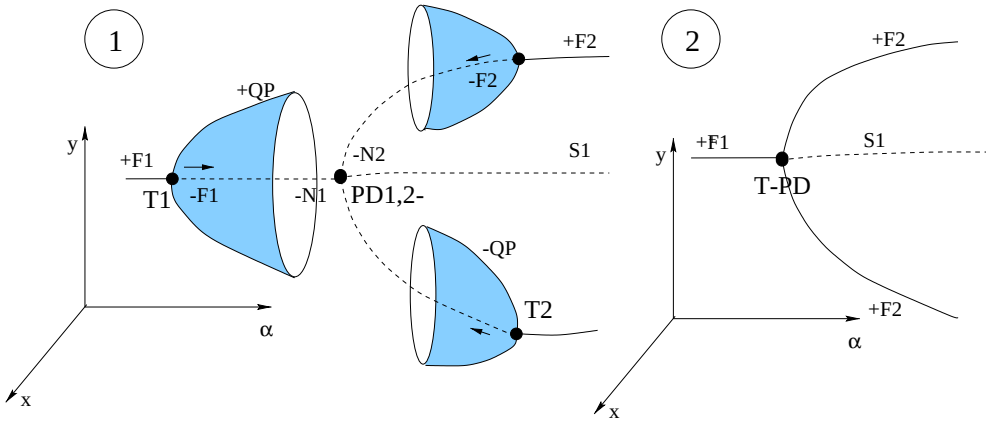

Figure 2.13 Subfigure 1 depicts how a +F1 passes through a T1 becoming a -F1 and giving rise to a quasiperiodic (QP) solution. The -F1 passes through an EE1- point (not shown) in order to double as a -N1. This causes it to lose stability and continue as an S1. The -N2 solution changes in an EE2- point (not shown) to a -F2 thereafter gaining stability in a T2 and becoming a +F2. In Subfigure 2 is seen how the QP solutions are destroyed at the T-PD bifurcation point.

T1 bifurcation curve the multipliers of the period-one solution cross the unit-circle and can be expressed by $\lambda_{1,2} = e^{\pm 2\pi i\theta}$ where $2\pi\theta$ is the angle at which they cross. Therefore, at a resonance point, θ must be a rational number. Thus, a R^p-point must be located in a resonant $p : q$ region, inside or on the border of the Arnol'd tongue. More specifically, resonance points can be found in the codimension two points where CD1 bifurcation curves connect (T1-SN1, T1-PD1,2 and SNp-SNp) and in singular points in which a period-p solution crosses itself and becomes identical to a period-one solution.
The Arnold tongues must contain at least one such resonance point and are divided into weak, $p \geqslant 5$, and strong, $p \leqslant 4$, resonance [Vance et al., 1989], [Taylor and Kevrekidis, 1991].

2.5 Global Bifurcations

In forced oscillators global bifurcations are typically found near the codimension two points. In fact, the existence of a homoclinic bifurcation is guaranteed in the neighbourhood of a Takens-Bogdanov bifurcation [Thompson and Stewart, 1986]. This is not evident from Fig. 2.11 but referring to Subfigure 1 one can see how the quasiperiodic attractor can collide with the inset of the saddle solution of period-one resulting in a Blue Sky Catastrophe. This is also proved in [Knudsen et al., 1991] along with a theorem for the existence of global bifurcations near T-PD codimension two points.

2.6 Summary

- A class of forced oscillators, in which the systems were forced across a Hopf bifurcation, was introduced.
- Entrainment regions in the excitation diagram were discussed. Related terms such as rotation numbers, resonance horns and Arnol'd tongues were introduced.
- Abbreviations for the possible types of periodic solutions were presented.
- Equal-eigenvalues curves were introduced along with a presentation of the generic codimension one bifurcations that may occur.
- Codimension two points were discussed in some detail. These included points where codimension one bifurcation curves connected and resonant points on a period-one torus bifurcation curve.

CHAPTER 3

The Model

THE MODEL to be considered in this work is a modified version of the generic normal form for a Hopf bifurcation subjected to an external sinusoidal forcing. In this chapter, the model is constructed and the various parameters of the system are presented and explained. Some of these are introduced as a result of transformations of the normal form, the effect of which will also be discussed. An analysis of the system dynamics is performed with the purpose of providing a basis for a discussion of the results obtained when forcing the system.

3.1 Choosing a Model

When faced with the task of deciding which system should be the basis of our investigation, several considerations had to be made. First of all it is of course desirable to be able to determine which features are generic for forced oscillators. Secondly, it should allow for alterations in the bifurcation structure of the autonomous system. This is desired because it provides several perspectives for future work with the model.
If an already existing model of an oscillating system was chosen, the results could be directly related to actual events be they biological, physical, or economic in nature, but such a choice would leave the question of which observations were generic and which were system specific unsettled.

With this in mind, the generic normal form for a Hopf bifurcation was chosen as the basis of the work in this thesis. Since this model must have dynamics common to all self-oscillating systems, the approach seemed to be ideal for an examination of generic aspects. Closer examination of the model reveals which parameters are responsible for the different parts of the autonomous oscillations such as period, amplitude, and location of the Hopf bifurcation. In addition to this, it is possible to decide if the Hopf bifurcations involved should be sub- or supercritical. These factors are important as they give a rather high degree of control over the oscillations, which provides a foundation for conversions of the underlying bifurcation structure.

Initial examinations of the forced system proved it necessary to make some modifications to the normal form. In its generic form it exhibited symmetries to a degree that made it impossible to attain a coupling between the external forcing and the internal oscillations, and thus no entrainment was observed. Unfortunately this transformation of the system required the generic aspect of the results be reconsidered. On the other hand, it provided the basis for an examination of different types of destruction of the resonance regimes. In addition to the breaking of the symmetry, a transformation of the time variable was performed. This was necessary in order to be able to use the period of the forcing as a control parameter for one- and two-dimensional

continuation schemes. The nature of the transformations will be elaborated on in the following.

3.2 The Normal Form for a Hopf Bifurcation

The normal form for a Hopf bifurcation is a system of two coupled differential equations. In Eq. (3.1) and Eq. (3.2) it is presented in Cartesian coordinates [Nayfeh and Balachandran, 1995].

$$\dot{x} = \mu x - \Omega y + (\alpha x - \beta y)(x^2 + y^2) \tag{3.1}$$
$$\dot{y} = \mu y + \Omega x + (\beta x + \alpha y)(x^2 + y^2) \tag{3.2}$$

For reasons, which will be explained, the numerical examinations have all been performed with the parameters α, β, and Ω fixed at values of -1, 0, and 1 respectively.

One equilibrium point exists for this system, namely $(x, y) = (0, 0)$. The stability of this equilibrium point is determined by the eigenvalues that are found to be $\lambda_{1,2} = \mu \pm i\Omega$, and the system thus undergoes a Hopf bifurcation at $\mu = 0$. Here, the set of complex-conjugate eigenvalues cross the imaginary axis transversally as discussed previously.

3.2.1 Parameter Significance

If the system is transformed to polar coordinates, a better understanding of the significance of the individual parameters for the autonomous oscillations is obtained. By doing so, information about the amplitude and frequency of the oscillations is acquired.
The transformation to polar coordinates is performed by setting $x = r\cos\theta$ and $y = r\sin\theta$. This gives $\dot{x} = \dot{r}\cos\theta - r\dot{\theta}\sin\theta$ and $\dot{y} = \dot{r}\sin\theta - r\dot{\theta}\cos\theta$, from which it is deducted that $\dot{x}\cos\theta + \dot{y}\sin\theta = \dot{r}$ and $\dot{x}\sin\theta - \dot{y}\cos\theta = -r\dot{\theta}$. Substitution of these relations into Eq. (3.1) and Eq. (3.2) yields expressions for the time derivatives of the amplitude and phase of the oscillation.

$$\dot{r} = \mu r + \alpha r^3 \tag{3.3}$$
$$\dot{\theta} = \Omega + \beta r^2 \equiv \omega_0 \tag{3.4}$$

Since $\dot{r}$ is a measure of the rate at which the amplitude r increases, the amplitude of the limit cycle can be found by solving $\dot{r} = 0$ with respect to r. This yields $r = 0$ or $r = \sqrt{-\mu/\alpha}$ which only makes physical sense when $\alpha > 0 \wedge \mu \leqslant 0$ or $\alpha < 0 \wedge \mu \geqslant 0$

For $\alpha > 0 \wedge \mu \leqslant 0$ we see that $\dot{r} = \mu r + \alpha r^3 > 0 \Rightarrow r > \sqrt{-\mu/\alpha}$ and similarly $\dot{r} < 0 \Rightarrow r < \sqrt{-\mu/\alpha}$ indicating that the amplitude will increase when the system is outside the limit cycle and decrease inside the limit cycle. So it is an unstable periodic solution, and since $\mu = Re(\lambda) < 0$ it is enclosing a stable equilibrium. When $\alpha > 0$, the system thus undergoes a subcritical Hopf bifurcation as the parameter μ is reduced through 0.

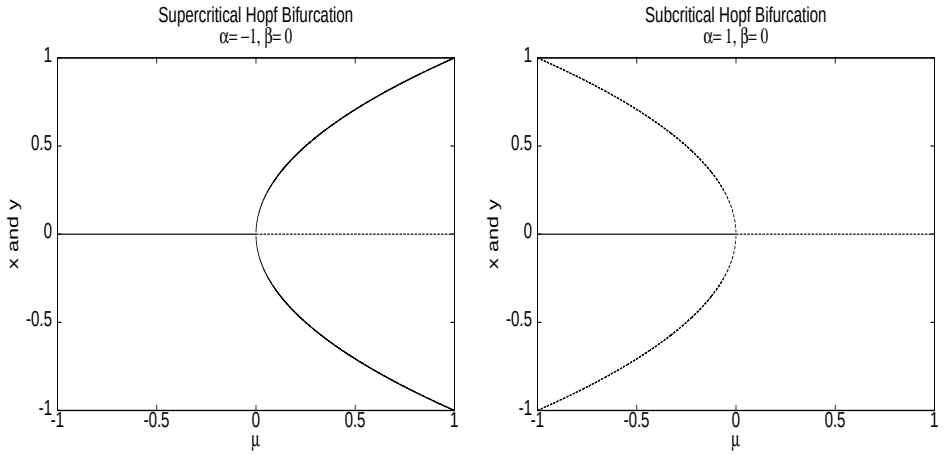

Figure 3.1 Super- and subcritical Hopf bifurcations occurring in the generic system. The bifurcations happen at $\mu = 0$ for $\alpha < 0$ and $\alpha > 0$ respectively.

By similar arguments, it is seen that when $\alpha < 0$ and $\mu \geqslant 0$ a stable limit cycle of amplitude $r = \sqrt{-\mu/\alpha}$ encloses an unstable equilibrium point, the oscillations are thus born through a supercritical Hopf bifurcation. Fig. 3.1 illustrates the two scenarios, and Fig. 3.2 shows the dynamics of the vector field around the isoclines and the limit cycles.

The crossing of the isoclines marks an equilibrium point. The isoclines are observed to be symmetric with respect to x and y, causing the limit cycles to be circular, and crossing it in points where it has vertical and horizontal tangents. In Section 3.4 it will be illustrated how these flow- symmetries are broken by a necessary transformation of variables.

It is now known that the sign of the parameter α decides if the bifurcation is super- or subcritical, that μ is the bifurcation-parameter, and that μ and α together determine the amplitude of the limit cycle. By looking at Eq. (3.4) further deductions regarding the parameters can be made. In addition to

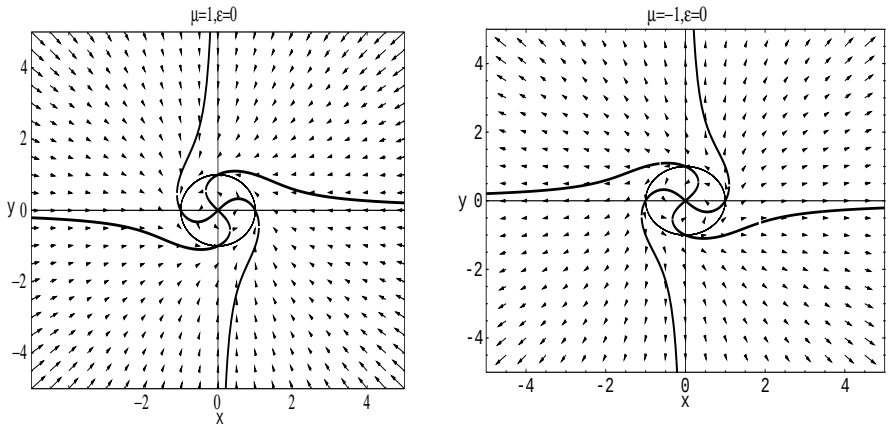

Figure 3.2 Vector fields and isoclines of the unmodified normal form, illustrating the stable and unstable limit cycles respectively. Isoclines are drawn with thick lines and limit cycles with thin lines.

a direct dependence on Ω, the frequency ω_0 of the autonomous oscillations depends on β, μ, and α through the second term in Eq. (3.4). Setting $\beta = 0$, the frequency and consequently the period become constant thus simplifying the dynamics of the unforced system significantly. As mentioned earlier, the numerical simulations have all been carried out with $\alpha = -1$, $\beta = 0$ and $\Omega = 1$. This leads to a system where oscillations of constant period 2π and amplitude $\sqrt{\mu}$ are born through a supercritical Hopf bifurcation at $\mu = 0$.

3.3 Modifying the Normal Form

The initial hope was that a periodic variation of the bifurcation parameter μ in the system Eq. (3.1)-Eq. (3.2) would yield the Arnol'd tongue structure of entrainment regions characteristic of forced oscillators. What was observed, however, was that entrainment occurred solely where the ratio of the forcing to the natural (autonomous) frequency was a rational number irrespective of the amplitude of the forcing, i.e. there was no opening of the Arnol'd tongues. We speculated that the high degree of symmetry of the normal form was the cause of this lack of entrainment. If no significant changes occurred in the dynamics through which the system was forced, how could any response to the modulation be expected?!? Variations in the parameter β were made, making the period of the autonomous oscillations depend on the value of μ, but without any effect. This observation was somewhat in accordance with both theoretical and experimental examinations made elsewhere. Entrainment was observed for a system forced in a region where the autonomous oscillations showed only little variation in the period [Sturis et al., 1995]. This led us to the conclusion that the simplification obtained by setting $\beta = 0$ would not prevent the results from being common to forced oscillators.

3.3.1 Breaking the Symmetry

The coupling to the forcing was instead achieved by a transformation of the system, leading to a parameter dependence in the location of the equilibrium point. Substituting x by $(x - \epsilon\mu)$ in the normal form one obtains the new

equilibrium point $(x, y) = (\epsilon\mu, 0)$. No substitution was made in the x^2 term since it was not necessary to introduce the parameter dependence. The new parameter ϵ dictates the slope of the set of equilibrium points in the (μ, x) plane. This change in the location of the equilibrium causes the system to experience the necessary variations in the transients as μ is varied periodically.

The transformation alters the system in such a way that the eigenvalues of the Jacobian, evaluated at the new equilibrium point, become $\lambda_{1,2} = \mu(1 + \alpha\epsilon^2\mu) \pm i\Omega$. As a result, a second Hopf bifurcation is introduced at $\mu = -1/\alpha\epsilon^2$. The new set of bifurcation curves in the (μ, ϵ) parameter plane is shown in Fig. 3.3. When tracing the bifurcation structure of the forced system in subsequent chapters, the effect of varying the workpoint in the (μ, ϵ) plane will also be examined.

The second Hopf bifurcation is also supercritical and will, for increasing μ, mark the end of the the autonomous oscillations. Setting $\epsilon = 0$ leads to

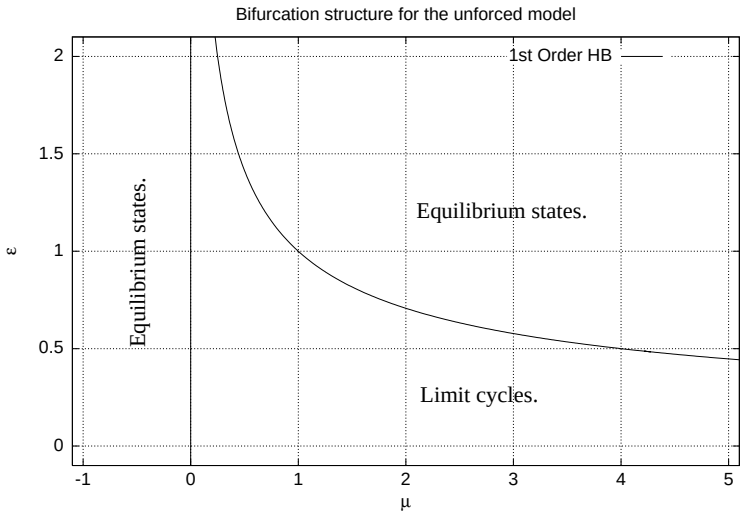

Figure 3.3 Supercritical Hopf bifurcation curves in the (μ, ϵ) plane.$\alpha = -1, \Omega = 1, \beta = 0$.

the original situation with only one bifurcation at $\mu = 0$. As ϵ is increased, the second Hopf bifurcation moves closer to the first one thus gradually reducing the region of oscillations. Fig. 3.4, which shows the equilibrium as well as the maximum amplitude of the autonomous oscillations, illustrates the effects of an increase in ϵ on the region of oscillations and the position of the equilibrium solution.

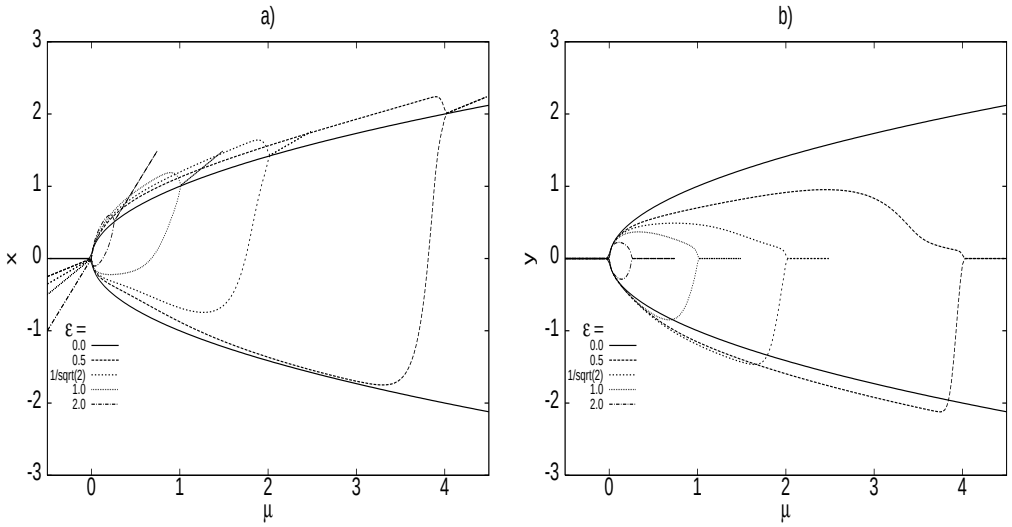

Figure 3.4 Maximum amplitude plots illustrating the autonomous oscillations for various values of ϵ.

By comparing Fig. 3.4 and Fig. 3.1 one notices that the amplitude no longer takes on the regular shape it did in the original system. In addition to the termination of the oscillations, the $x \rightarrow (x - \epsilon\mu)$ substitution causes variations in the amplitude and the frequency of the autonomous oscillations. A transformation of the modified system to polar coordinates yields more complex analytical expressions for $\dot{r}$ and $\dot{\theta}$.

$$\begin{aligned}\dot{r} &= \mu r + \alpha r^3 - \mu^2\epsilon\cos\theta - \Omega\mu\epsilon\sin\theta - r^2\epsilon\mu(\alpha\cos\theta + \beta\sin\theta) \\ \dot{\theta} &= \Omega + \beta r^2 + \epsilon\mu r(\alpha\sin\theta - \beta\cos\theta) + \frac{\epsilon\mu^2\sin\theta - \epsilon\mu\Omega\cos\theta}{r}\end{aligned} \quad (3.5)$$

It is no longer possible to obtain simple expressions for the amplitude and period - even if $\beta = 0$. A significant change is the phase dependence in the frequency and amplitude which tells us that at a given μ the limit cycle of the unforced system will no longer be circular, and will be traversed at a rate which varies with position. If not for the fact that r and θ are still 2π periodic (for $\Omega = 1$), the position at which the Arnol'd tongues originate would be difficult to predict. The system does, however, behave as expected.

3.4 The Dynamics of the Autonomous System

At this point, the bifurcation structure of the unforced system has been examined, and two distinct Hopf bifurcations have been located in the (μ, ϵ) plane. These bifurcations separate this into three regions; two regions containing only steady state solutions separated by a stretch supporting autonomous oscillations. When forcing is introduced, the system will be varied through these areas of different flow in a periodic manner. The autonomous states visited in the course of one period will vary according to the choice of workpoint and amplitude of the forcing.

To gain a better understanding of the dynamic of the underlying system, a series of plots, illustrating the vector fields at different locations in the regions, is presented in Fig. 3.5. The chosen points lie either on the $\mu = 1$ or the $\epsilon = 0.5$ grid lines seen in Fig. 3.3, and are representative of areas forced into in Section 5.6. Additional plots can be found in Appendix A.

The first plot (moving left to right and top to bottom) illustrates the flow in the leftmost region of steady state solutions. By comparison with Fig. 3.2 the displacement of the stable focus from the origin is noticed. This is an effect of the symmetry-breaking transformation. Keeping ϵ fixed at 0.5 and increasing μ brings us to the next plot which is exactly in the first bifurcation

point at $\mu = 0$. A characteristic feature of the bifurcation points is the perpendicular crossing of the isoclines. Since the limit cycle is just born it is of zero amplitude and thus not seen.

Further increase of μ leads to the following two figures in which the limit cycle is seen. The flow has become irregular in the sense that the limit cycle is not circular and the isoclines no longer symmetric as in Fig. 3.2. Had μ been followed to higher values, yet another perpendicular crossing of the isoclines would have been observed at the second bifurcation. This is also seen when keeping μ fixed and increasing ϵ as is done in the last two plots with $\mu = 1$.

There are points in the plane (as can be seen in Appendix A) where closed loops of null- or ∞-clines emerge. This is the effect of a curve folding to the extent of touching itself. Since the isoclines by definition cannot cross themselves transversally, any 'homoclinic' connection causes the fold to be pinched off, thus causing the creation of a separate loop and the connection of the two remaining pieces. Such loops exist in the rightmost steady-state region, but neither kind of loop has been found to the left of $\mu = 0$. Consulting the figures in the appendix it is seen that the loops enclose areas of the state space in which the flow is directed away from the equilibrium point.
Two kinds of Arnol'd tongue destruction have been observed. It is suspected that the flow differences in the various regions of the autonomous system are what cause the two types of collapse to differ.

Figure 3.5 Vector fields and isoclines illustrating the flow in the x-y plane at various points in the $\epsilon - \mu$ plane. Isoclines are drawn with thick lines and limit cycles with thin lines.

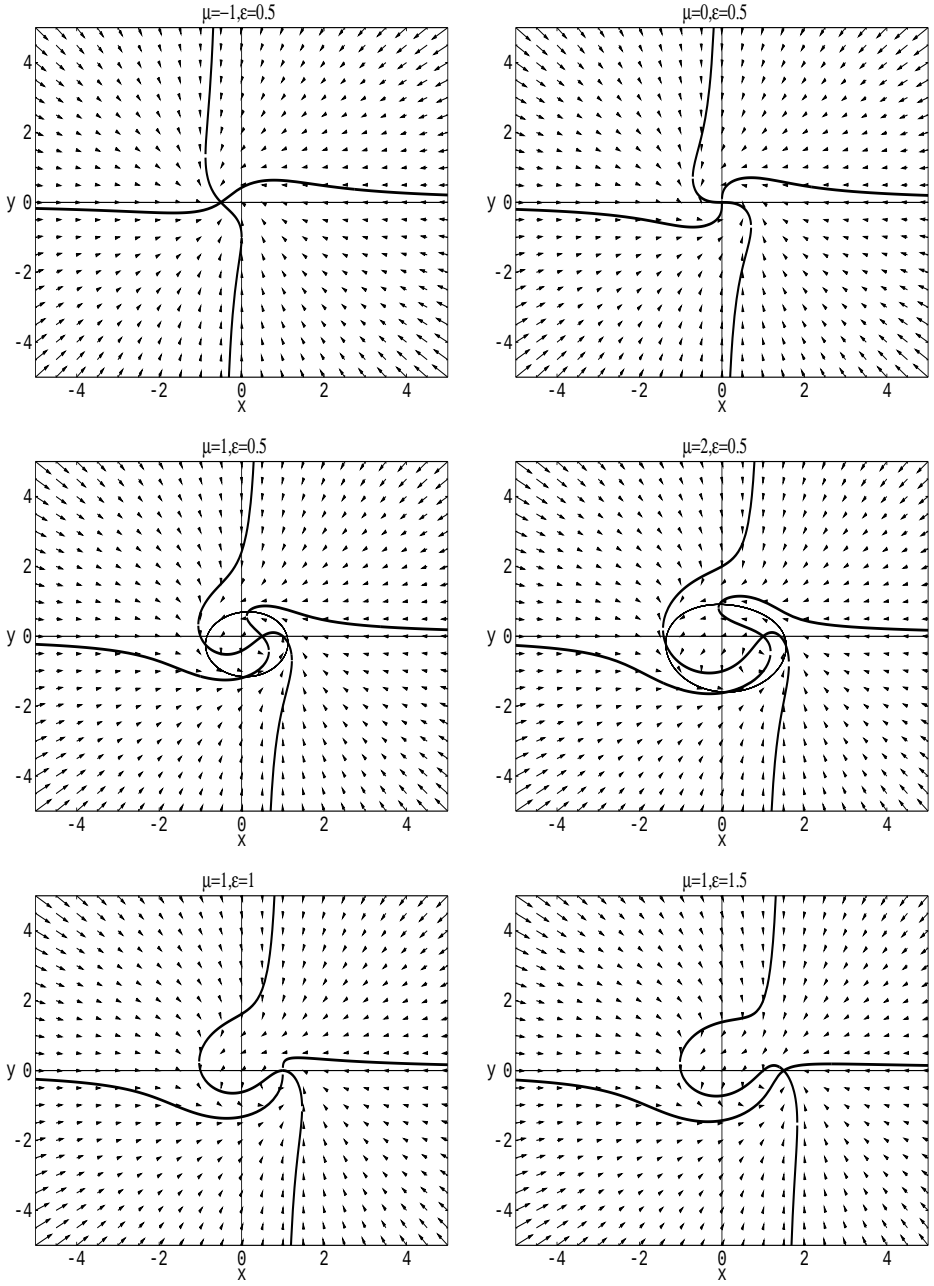

3.5 Forcing the System

The forcing of the oscillator is done by periodically varying the bifurcation parameter μ i.e. an actual forcing of the system in the vicinity of and across a Hopf bifurcation.

In practice the periodic forcing is introduced by the substitution $\mu \rightarrow (\mu_0 + A\sin\omega t)$, and so the workpoint is (μ_0, ϵ). Three new parameters μ_0, A, and ω have been introduced. These play key roles in the later analysis of the bifurcation structures.

3.5.1 Transformation of the Time Variable

When analyzing the dynamics of forced oscillators it is valuable to follow bifurcation curves in the frequency-amplitude plane, in order to locate possible regions of periodic entrainment and trace the resonance tongues. For this purpose, so-called continuation schemes are employed in one and two dimensions. The use of this technique will be discussed in the following chapter and reference is made to Appendix B for a more detailed description of the implementation. The $\sin\omega t$ term in the forcing poses a problem when trying to trace bifurcation curves in the (ω, A) plane. This is overcome by introduction of a new time variable $\tau = \omega t$. Letting superscripts t or τ denote the time frame of interest, and subscript F terms associated with the forcing, it is found that $T_F^\tau = T_F^t \omega_F^t = 2\pi$. The period of the forcing is thus constant and equal to 2π in the new time frame.

In the limit of zero forcing amplitude, the characteristic frequencies of the system are the frequency of the forcing ω and the natural oscillation frequency ω_0. p and q are invariant to the transformation of the time variable, and so the rotation number is unaltered and is found as

$$\rho = \frac{T_F^t}{T^t} = \frac{2\pi/\omega_F^t}{2\pi} = \frac{1}{\omega_F^t} \equiv \frac{1}{\omega}$$

The 2:1 tongue is thus known to originate at $1/\rho$=p/q=$2/1=\omega$, the 4:5 tongue at $1/\rho=\omega=4/5$ etc.

3.6 The Final Model

At this point, the generic normal form has been modified to reach the final form shown in Eq. (3.6). This is the system examined in this work. A list and brief description of the parameters is given in Table 3.1. Throughout this report, the actual set of parameters will be referred to by the parameter-vector $\mathbf{M} = (\mu_0, \alpha, \beta, \Omega, A, \omega, \epsilon)$.

$$\begin{aligned} \dot{x} = \frac{dx}{d\tau} &= \frac{1}{\omega}(\mu(x - \epsilon\mu) - \Omega y + (\alpha(x - \epsilon\mu) - \beta y)(x^2 + y^2)) \\ \dot{y} = \frac{dy}{d\tau} &= \frac{1}{\omega}(\mu y + \Omega(x - \epsilon\mu) + (\beta(x - \epsilon\mu) + \alpha y)(x^2 + y^2)) \\ & \qquad \textit{where} \quad \mu = \mu_0 + A\sin\tau \end{aligned} \tag{3.6}$$

Table 3.1 Model Parameters and Their Significance

$$\mathbf{M} = (\mu_0, \alpha, \beta, \Omega, A, \omega, \epsilon)$$

μ_0	:	Workpoint parameter. Value around which the bifurcation parameter μ is forced.
α	:	Parameter controlling the nature of the Hopf bifurcation: $\alpha < 0 \Rightarrow$ Supercritical Hopf bifurcations, $\alpha > 0 \Rightarrow$ Subcritical Hopf bifurcations
β	:	Parameter weighing the influence of the amplitude on the natural oscillation frequency: $\beta = 0 \Rightarrow$ the only variations in ω_0 are due to the $x \rightarrow (x - \epsilon\mu)$ substitution.
Ω	:	The constant part of the natural oscillation frequency, ω_0.
A	:	Amplitude of the periodic forcing.
ω	:	Frequency of the periodic forcing.
ϵ	:	Workpoint parameter. Determines the slope of the curve of equilibrium solutions in the x-μ plane.

The model is no longer the generic normal form for a Hopf bifurcation, but a high degree of parameter control allows for the forcing and many aspects of the underlying autonomous system to be adjusted.

One of the future perspectives of the model is the examination of the forcing over two supercritical Hopf bifurcations separated by a region of steady state solutions. When considering the eigenvalues of the linearization of the autonomous vector field around the equilibrium point, it is seen that the desired bifurcation structure of the underlying system can be achieved by a proper transformation of the bifurcation parameter. In the case of the pure normal form, this is particularly simple as it can be done by replacing μ with a term quadratic in μ e.g. $\mu \to (\mu - a)^2 - b$ (still keeping in mind that $\mu = \mu_0 + A \sin \tau$). This would cause the eigenvalues, $\lambda_{1,2} = \mu \pm \Omega$, to cross the imaginary axis twice leading to two Hopf bifurcations. By variation of the parameters a and b, the location and separation of the bifurcations can be controlled.

An analogue approach can be used in the case of the system Eq. (3.6). Since $\lambda_{1,2} = \mu(1+\alpha\epsilon^2\mu) \pm i\Omega$ is already quadratic in μ, a substitution similar to the one mentioned would result in $Re\{\lambda_{1,2}\}$ being a fourth order polynomial in μ. By adjusting the parameters one can ensure four crossings of the imaginary axis resulting in four Hopf bifurcations. Instead of the unbounded regions of oscillations one would obtain with the generic normal form, the regions are bounded. The extent of the different regions is dictated by the shape of the fourth order polynomial.

In the present thesis the attention will be restricted to the case of one autonomously oscillating region. This scenario in itself, contains a wealth of interesting bifurcation structures which we felt should be examined in some detail prior to any analysis of the forcing over two bifurcations.

3.7 Summary

- The generic normal form for a Hopf bifurcation was presented and discussed as it is the basis of the model considered in this work.
- Various transformations of the generic normal form were carried out. A periodic variation of the bifurcation parameter and a transformation of the time variable were introduced, both without affecting the bifurcation structure of the autonomous system. It was necessary to perform a symmetry-breaking transformation to get entrainment. This led to a second curve of Hopf bifurcations bounding the region of autonomous oscillations in the plane.
- An analysis of the underlying autonomous system was performed to provide a basis for the numerical investigations of the forced system. The flows in the two regions of stable equilibrium solutions were found to differ.
- The significance of the model parameters was discussed in relation to the analysis of the autonomous system and the effect of the transformations. A vector containing the parameters of the forced system was defined; $\mathbf{M} = (\mu_0, \alpha, \beta, \Omega, A, \omega, \epsilon)$.
- Suggestions were made for future work with the model, which could involve forcing across two Hopf bifurcations. By substituting the control parameter with an appropriate polynomial, the system can be altered to have two regions of autonomous oscillations separated by a region with a stable equilibrium.

CHAPTER 4

Methods and Tools

HAVING PRESENTED some of the relevant theory and introduced the model, attention is now turned to the methods and tools used in the numerical analysis. The purpose of this chapter is not to give a detailed description of each method. It is meant to give an overall view, introducing the different numerical tools. It will be discussed (i) when a method is relevant to apply, (ii) how the methods depend on each other, and (iii) what the advantages and disadvantages of the different methods are. The interested reader is referred to Appendix B in which the methods are described in more detail.

4.1 Locating Solutions

In this section the numerical approximation of an integral curve related to an initial value problem is briefly discussed. Different techniques to locate various types of solutions are outlined and at the end of the section a method is presented of how to construct one-dimensional invariant manifolds. Construction of these can be very useful in locating solutions and in understanding the dynamics of the system.

4.1.1 Numerical Integration

Let a dynamical system be described by an N dimensional nonautonomous system:

$$\dot{\mathbf{x}} = \mathbf{F}(\mathbf{x}(t), t, \mathbf{M}), \qquad \mathbf{x} \in \mathbb{R}^N,\ t \in \mathbb{R},\ \mathbf{M} \in \mathbb{R}^P,\ \ \mathbf{x}(t_0) = \mathbf{x}_0. \tag{4.1}$$

$\mathbf{x}$ is a state vector of N variables, t is time, and $\mathbf{M}$ is a parameter vector of P parameters. $\mathbf{x}_0$ is the initial condition for the system and $\mathbf{F}$ represents the time varying nonlinear vector field.

If $\mathbf{F}$ is a nonlinear function Eq. (4.1) generally cannot be solved analytically. Instead numerical methods must be applied to solve the nonlinear system approximating $\mathbf{x}(t)$. Naturally, we cannot solve numerically for a continuous solution, but have to settle with an approximation of the states $\mathbf{x}_0, \mathbf{x}_1, \mathbf{x}_2, \cdots$ at a discrete set of points in time $t_0, t_1, t_2, \cdots$.

The numerical methods are numerous and all have different advantages. In choosing between the methods one has to weigh the speed against the precision and stability of a method. Moreover, the choice depends on the specific system and on the type of phenomena one wishes to study.

Methods by which $\mathbf{x}_n$ is calculated at the time t_n based only on the knowledge of the state at t_{n-1} are called *one-step methods*. If the methods require information of a time series with k elements - e.g. the system states at the times $t_{n-k}, t_{n-k+1}, \cdots, t_{n-1}$ - the methods are called *multi-step methods*. Furthermore, the methods are classified as *implicit* or *explicit methods*, depending on whether $\mathbf{F}$ has to be solved implicitly or explicitly. Finally, the

methods are classified depending on whether they use *fixed step-length* or *variable step-length*.

Though multi-step methods are often more stable, one-step methods generally appear more flexible requiring knowledge of the solution at just one point t in time in order to proceed with the integration. Implicit methods have the advantage of being generally more stable than explicit methods and can therefore use larger step-length. However, one also has to consider the amount of extra work it takes to solve $\mathbf{F}$ implicitly. This work can be quite extensive, since $\mathbf{F}$ often has to be solved a number of times depending on the number of the sub-steps for the particular method.

We have chosen to apply two different explicit one-step methods, one of which is the Runge-Kutta 4 method which uses a fixed step-length; the second one is the Runge-Kutta 5/6 method employing a variable step-length. Further discussion of these methods is found in Section B.1. Both methods are very popular and are described as being among the most efficient and accurate codes available [Lambert et al., 1990],[Kampmann, 1995].

4.1.2 Poincaré Sections

A number of different types of solutions can be found in a dynamical system. They can be of different dimension and the simplest solutions are equilibrium points. These can be determined by

$$\mathbf{F}(\mathbf{x}, t, \mathbf{M}) = 0 \tag{4.2}$$

and are of zero dimension. Examples of higher dimensional solutions are one-dimensional periodic solutions, Q-dimensional quasiperiodic solutions ($Q \leq 2$), and chaotic solutions of non-integer dimension. The solutions can be studied using Poincaré sections (P-section/P-mapping). For an N-dimensional autonomous system, a P-section is a sampling of the trajectory of the solution in an $(N-1)$-dimensional subspace of the state space. For a nonautonomous system, we work in the extended state space and typically choose to sample the integral curve in the time dimension at evenly spaced intervals. Such a P-section is often referred to as a *stroboscopic P-section*.

Higher order P-sections are based on the idea of multi-sampling. Each sampling reduces the dimension of the system by one, making them useful in identifying quasiperiodic solutions.

In order to be able to study periodic solutions the continuous-time system is transformed to a discrete-time system using the P-section. As we shall be dealing with a forced nonautonomous system, we choose a P-section equivalent to sampling the trajectory at a rate equal to the forcing frequency of our system.

If $T_F = 2\pi/\omega_F$ is the period of the forcing (ω_F being the angular forcing frequency), then the stroboscopic P-section can be described by:

$$\mathbf{x}_0 \to \mathbf{x}_k = \mathbf{P}^k(\mathbf{x}_0) = \mathbf{x}_0 + \int_{t_0}^{t_0+kT_F} \mathbf{F}(\mathbf{x}(t), t, \mathbf{M})dt \qquad k = 1, 2, \cdots \tag{4.3}$$

A period-k solution of our system is now found as a kth-order fixed point of this map, and is determined by

$$\mathbf{x}_0 - \mathbf{x}_k = \mathbf{x}_0 - \mathbf{P}^k(\mathbf{x}_0) = 0 \tag{4.4}$$

For a given fixed point we can calculate the *Floquet multipliers*, the eigenvalues of the P-map. They can be used to classify the stability of the periodic solution.

4.1.3 The Brute Force and the Newton Raphson Approach

For a given set of parameter values there are many different methods one can apply in order to locate the different solutions of a dynamical system. Here we present the *Carpet Bombing* (CB) technique. As the name indicates, we begin by choosing different initial conditions scattered over the state space. At each of these states one can use different approaches to locate the solutions in the neighbourhood. These approaches have different advantages and disadvantages. Two different techniques are presented: (i) the *Brute Force* approach and (ii) the *Newton Raphson* approach.

Brute Force

Brute Force (BF) is a method in which the system is integrated and iterated until steady state is achieved. Thus, stable solutions can be located, and by integrating in reverse time, unstable solutions as well. Saddle solutions cannot be located by this method since they have both stable and unstable insets. Brute Force is general and simple but has slow convergence, and it is difficult to tell when steady state has been achieved. Note that as long as the initial condition is in the basin of attraction of an attractor, the BF method always converges. The method is easy to implement and all that it requires is a numerical integration scheme.

Newton Raphson

The Newton Raphson (NR) approach is more sophisticated than the BF. The problem of locating a limit set is transformed into a task of calculating the zeros of a system of nonlinear equations. The NR algorithm is then applied to either Eq. (4.2) in order to locate equilibrium points or Eq. (4.4) to locate fixed points of the P-map. The NR algorithm is explained in Section B.5. The main advantages of using the NR approach are quadratic convergence and the fact that any type of equilibrium point or fixed point can be located. If one is using higher-order P-sections, quasiperiodic solutions may also be located. The approach suffers from the drawbacks that it cannot locate chaotic solutions, and that the initial states have to lie close to the solutions in order to guarantee convergence. To locate different solutions by the NR method tools of integration and construction of P-sections are necessary.

4.1.4 Manifolds

One way of constructing a one-dimensional unstable half-manifold of a fixed point is by simply iterating a point chosen near the fixed point on the eigenvector corresponding to the direction one wishes to study. By reverting time, stable manifolds may also be studied in a similar manner. Even if the initial points lie near the fixed point, their iterates can be quite far apart resulting

in a poor approximation of the manifolds. The stretching is especially common in chaotic systems. A better technique is to slide a window of points along the manifolds trying to construct a reasonable density of points. This method is reasonably fast and can be constructed in such a way as to have the number of points in the window increased when the dynamic along the manifold becomes very strong or when the manifold is winding.

When able to construct the stable and unstable invariant manifolds of a fixed point the advantages one gains are considerable. The information can be used, not only in understanding the transient dynamics in the state space, but naturally also in explaining global bifurcation since homoclinic and heteroclinic orbits can be constructed. Furthermore, when trying to locate all solutions in the state space, one would often choose to construct the stable manifolds of different saddle fixed points. These manifolds separate the basins of attraction, and through construction of these information is obtained, indicating whether all areas of the state space have been analyzed sufficiently.

We refer to Section B.4 in which the numerical technique is presented for construction of one-dimensional invariant manifolds. Although the technique for construction manifolds of a equilibrium point is easier, the presented method only applies to manifolds of a fixed point. Naturally, the method depends on the integration method and on setting up a P-section.

4.2 Tools to Analyze the Solutions

Having located different solutions in the state space, different techniques of retrieving information from the solutions are presented. In the following we shall not be interested in equilibrium solutions, but only in solutions that are not constant in time.

4.2.1 Rotation Number

For a two-dimensional nonautonomous system the rotation number was defined in Chapter 2 as the ratio of the two dominant frequencies in the system.

We shall briefly explain how the rotation number is calculated for a periodic or a quasiperiodic solution: In order to calculate ρ a technique is used in which a one-sided P-section is applied to our nonautonomous system. In this case the one-sided P-section corresponds to a sampling every time the line $y = 0$ is crossed by the trajectory of a solution moving from negative to positive values of the x variable. This map is iterated towards infinity (in principle) while keeping track of the time needed for the system to get close to its initial condition. This simulation is repeated for infinitely (in principle) many initial conditions.

The technique gives us the average number of iterations q and the average time T_q it takes to get back to the initial condition on the one-sided P-section. By dividing T_q with the period of the forcing, p is found. This is used to estimate the rotation number as the fraction $q/p = q\ T_{forcing}/T_q$ with respect to the stroboscopic mapping. Applying the method to a chaotic solution we can expect some problems since the number of iterations needed to get close to the initial values will appear random.

4.2.2 Lyapunov Exponents

The *Lyapunov exponents* are measures of average divergence of neighbouring trajectories. The absolute value of the exponents indicate the speed with which the curves converge, respectively diverge. Negative exponents express convergence and positive exponents divergence. Zero Lyapunov exponents indicate neither convergence nor divergence. Note that for dissipative systems the sum of the exponents will be negative and equal to the dissipation in the system.

An N-dimensional nonautonomous system have $N+1$ exponents, but as the rate of change of the time-variable is constant, one exponent is always zero. For periodic solutions an additional exponent is found to be zero, and for a Qth-order quasiperiodic solution $Q+1$ Lyapunov exponents will be zero. As a positive exponent implies divergence we use this as an indicator of chaos, provided that the dynamic remain bounded.

The Lyapunov exponent of an N-dimensional nonautonomous system can be calculated by studying $N+1$ neighbouring orbits/curves in the state space.

From one of the curves we span N orthonormalized vectors to the other curves. This is done in a way such that all the vectors originate from the same point and end on different curves at the same instant in time. The average growth in time of the length of a vector corresponds to the largest Lyapunov exponent. The sum of the two largest Lyapunov exponents is calculated as the average growth of an area spanned between two vectors and so-forth. To avoid numerical problems, the vectors are orthogonalized from time to time, and to get the best estimates of the Lyapunov exponents, one should in principle run the simulation towards infinity. In practice this is done by simulating over a time period that is many times (typical factor 10) longer than the normal period of the dynamics. The technique is relatively fast and effective. Note that the method does not need a P-section for calculating the Lyapunov exponents.

4.3 Construction of Solution and Bifurcation Curves

After locating solutions in the state space, it may be of interest to follow the solutions into system space. Naturally, one could just apply the carpet bombing technique for different sets of parameter value but this is a very slow technique. We now present two different methods used to follow solutions under variation of a control parameter. The methods can be useful in determining bifurcation points and in constructing bifurcation curves in system space.

4.3.1 Brute Force Scanning

This is a general method for calculating bifurcation diagrams of stable steady-state solutions. Its advantages are generality and simplicity. Let m be the control parameter that we wish to vary over the interval m_{min} to m_{max}. The system is then simulated for S evenly spaced parameter values in the interval. For the sth simulation, the P-map of the system is iterated a fixed number of times. After discarding a transient, the system is assumed to be in the steady state and the remaining iterations are saved. The drawbacks of

the method are a long simulation time and an inability to locate saddle-node solutions.

One trick to speed up the technique is to use adiabatic initial conditions. We simply use the last values of the state of the system from the sth simulation as the initial conditions for the next simulation $s+1$. If S is reasonably large, so that m_s is close to m_{s+1}, and there has been no bifurcation over the interval, then the steady state solutions at m_s and m_{s+1} are approximately the same. We can therefore assume that the adiabatic approach reduces the duration of the transient considerably.

The adiabatic technique leads to an interesting artifact called *bifurcation transient*. Bifurcation transients appear on a BF-diagram just after a bifurcation when the simulation does not achieve the steady state. We speak of a *delayed response* in passing the bifurcation point. This artifact is mainly found for non-catastrophic bifurcations and can be explained by the following. Assuming that the simulation before the bifurcation achieved steady state, then the initial condition for the simulation just after the bifurcation lies nearly on the now unstable solution. One of the eigenvalues of the P-map has just passed through the unit circle and must have a magnitude only slightly greater than 1. Therefore, the simulation length is often too short for the orbit to move significantly far from the weakly repelling solution.

BF-scanning with adiabatic initial conditions is useful when locating coexisting solutions. This involves an analysis in which an interval is scanned with both increasing and decreasing control parameter. In such analysis we may experience hysteresis effects indicating the existence of a catastrophic bifurcation.

4.3.2 The Continuation Method

Consider a solution determined as the root of the function $H = H(\mathbf{x}, \mathbf{M})$. By calculation of the gradient at a point $(\mathbf{x}_0, \mathbf{M}_0)$, the solution can be followed into system space by a method of prediction and correction. Determining the differential $DH(\mathbf{x}, \mathbf{M})$ we find that

$$D\mathbf{H}(\mathbf{x}, \mathbf{M}) = D_x\mathbf{H}(\mathbf{x}, \mathbf{M})d\mathbf{x} + D_{\mathbf{M}}\mathbf{H}(\mathbf{x}, \mathbf{M})d\mathbf{M} = 0 \qquad (4.5)$$

If the system is of dimension N and P is the number of system parameters, then $D_x\mathbf{H}(\mathbf{x},\mathbf{M}) \in \mathbb{R}^{N\times N}$ and $D_{\mathbf{M}}\mathbf{H}(\mathbf{x},\mathbf{M}) \in \mathbb{R}^{N\times P}$. Thus, Eq. (4.5) is a system of $N+P$ variables and only N equations. The system is therefore singular, and to solve for the gradient we need to establish P extra conditions. In Section B.6 we explain how to solve the system of equations including either one or two-dimensions of the parameter space following solution curves or bifurcation curves.

Note: When applying the continuation methods to a forced system with the intent of studying solutions of the system under variation of the forcing frequency ω^t, one can encounter serious problems. The problems arise if a stroboscopic mapping is used. If we do not transform the system into a time dimension in which the forcing frequency ω^τ is constant, we will not be able to use the frequency ω^t as a control parameter.
Consider a case in which we wish to study a period-one solution of the system found at the frequency $\omega^t = \omega_1^t$. In an attempt to follow the solution the continuation method will try to locate a solution of the period $T_1^t = 2\pi/\omega_1^t$ at a new value $\omega^t = \omega_2^t$. But here a period-one solution has a period of $T_2^t = 2\pi/\omega_2^t \neq T_1^t$, thus making the task impossible for the continuation method. The problem can be solved by transforming the system into a new time dimension in which the stroboscopic mapping is unaffected by the variation of the forcing frequency in the old dimension. This is typically done by the transformation $\tau = \omega^t t$, which stretches or compresses time depending on the forcing frequency. Such a transformation has been used in Chapter 3.

1D Continuation

Including one-dimension of the parameter space allows us to study equilibrium and periodic solutions curves in a bifurcation diagram. We have the possibility of finding local bifurcation and of locating equal-eigenvalues points. The method implemented uses variable step-length and is relatively fast and stable. We employ a step-reducing method when locating the bifurcation/EE points, guaranteeing convergence and high accuracy.

2D Continuation

Including yet another dimension of the parameter space, 2D continuation gives us a method of constructing codimension one bifurcation curves. Compared to 1D continuation, the extra amount of numerical work 2D continuation demands is unfortunately quite significant, thus reducing the attractiveness of the method. Furthermore, the stability of the method also seems reduced as branch jumping, convergence problems, and problems of controlling the direction of construction are increasingly troublesome. Adjusting step-lengths and tolerances will of course help 2D-continuation past some of its problems. Keep in mind, though, that this would probably have to be done not only for the different types of bifurcation curves but perhaps also several places along a single bifurcation curve.

1D Continuation with alternating control parameters.

Bifurcation/EE curves can be constructed using only 1D continuation. Having found a bifurcation point using m_1 as a control parameter, we simply change to a different control parameter m_2, and choose a direction to travel away from the bifurcation point. We thus move a small distance away from the bifurcation point, then change the control parameter back to m_1, and start the search back towards the bifurcation curve. We thereby construct the bifurcation curve in m_1, m_2-parameter space. The technique proves to be a fast and stable method. Moreover, while navigating in parameter space, one quickly gains insight in complicated bifurcation structures.

Using this method we can rather easily construct bifurcation curves where 2D continuation had serious problems converging or was very slow. Due to the type of technique 1D continuation uses in locating bifurcation/EE points, we are guaranteed to stay on one side of a bifurcation curve in parameter space. This aspect proves important and allows us to e.g. travel deep into a cusp. It also helps us to differentiate between different bifurcation curves that lie close in the system space. Of course, the method has a drawback since it does not automatically follow the bifurcation curve and therefore has to be controlled closely. Some automation is possible, and after evaluation the method appears to be an excellent alternative to 2D-continuation in that it

speeds up construction and understanding of the bifurcation structure. In order to visualize how the technique tracks the bifurcations in system space, reference is made to Fig. 2.5. As long as control is maintained, maneuvering on the +N1 solutions that continues up towards larger β, it will be possible to construct the lower SN1+ bifurcation curve. The curve can be constructed without interference from the upper SN1+ bifurcation. By applying the technique it is possible to differentiate between the lower and the upper SN1+ bifurcations with high numerical accuracy.

4.4 Summary

- Families of numerical integration schemes were briefly presented, that will give the foundation for more advanced numerical tools.
- The stroboscopic Poincaré-section was set up in order to study the dynamical solutions of a forced oscillator.
- Different techniques useful to locate solutions in the state space were presented - this included the Brute Force and the Newton Raphson Approach.
- Techniques that construct one-dimensional invariant manifolds of fixed points of the stroboscopic map were introduced.
- A tool that can calculate the rotation number of a periodic or a quasiperiodic solution was described. Additionally, a technique to calculate the Lyapunov exponents was presented. These tools are especially useful in analyzing a dynamical solution.
- Brute Force scanning was explained. Related terms such as bifurcation transient and delayed response were introduced.
- Continuation methods were presented, whereby both the 1D and the 2D technique were introduced. A technique that applies 1D continuation with alternating control parameters was also presented. The latter technique proved itself as an attractive alternative to 2D continuation.

CHAPTER 5

Results

ATTENTION is now turned to the results of the computations. The foundation of these discussions will be the excitation diagram, which is the bifurcation structure in the frequency-amplitude plane of the forcing.
First the connection of entrainment regions in a representative excitation diagram is outlined and, subsequently, the focus will be on the individual tongues for a specific set of parameter values. The tongues are discussed according to the period of the entrained solutions, some of them in more detail than others. The nature of the local and global bifurcations is elucidated primarily by means of one-dimensional bifurcations diagrams and stroboscopic phase portraits. Finally, the destruction of Arnol'd tongues is discussed in relation to variations of the workpoint.

5.1 The Excitation Diagram

An excitation diagram of the forced system is shown in Fig. 5.1. The diagram consists mainly of the dominant 1:1 and 2:1 entrainment tongues, but shown are also the 3:1, 4:1, and lesser tongues of 2:3, 4:5, and 3:2 locking. An infinite number of tongues exist, but as the period of the entrained solutions increases, the tongues become very thin and thus difficult to trace numerically. The tongues may also overlap. Such regions of overlap are seen in Fig. 5.1, and they lead to coexisting attractors of various types.

Unless it is stated otherwise, the results presented in the following sections are found at the same set of parameter values at which this diagram is obtained, that is with $\mu_0 = 1, \epsilon = 0.5$, $\alpha = -1, \beta = 0$ and $\Omega = 1$. As expected, the tongues originate at values of the forcing frequency equal to the respective p/q ratio of the entrainment and gradually widen at higher forcing amplitudes. It is noted, that no tongue structures are present at forcing amplitudes larger than approximately A=2. The corresponding region of the (μ, ϵ) parameter plane, over which the system is forced, can be seen in Fig. 3.3. This involves a forcing across one of the Hopf bifurcations.

In addition to the bifurcation curves, the period-one equal-eigenvalues curves have been plotted in Fig. 5.1. This is to observe their location relative to the set of entrainment regions. Their form and location is somewhat dictated by the Arnol'd tongues and corresponding resonance points.

The boundaries of the entrainment regions consist mainly of saddle-node bifurcation curves, but also curves of period doubling and torus bifurcations separate the different frequency-locking regions or mark the transitions from quasiperiodicity to periodic solutions.

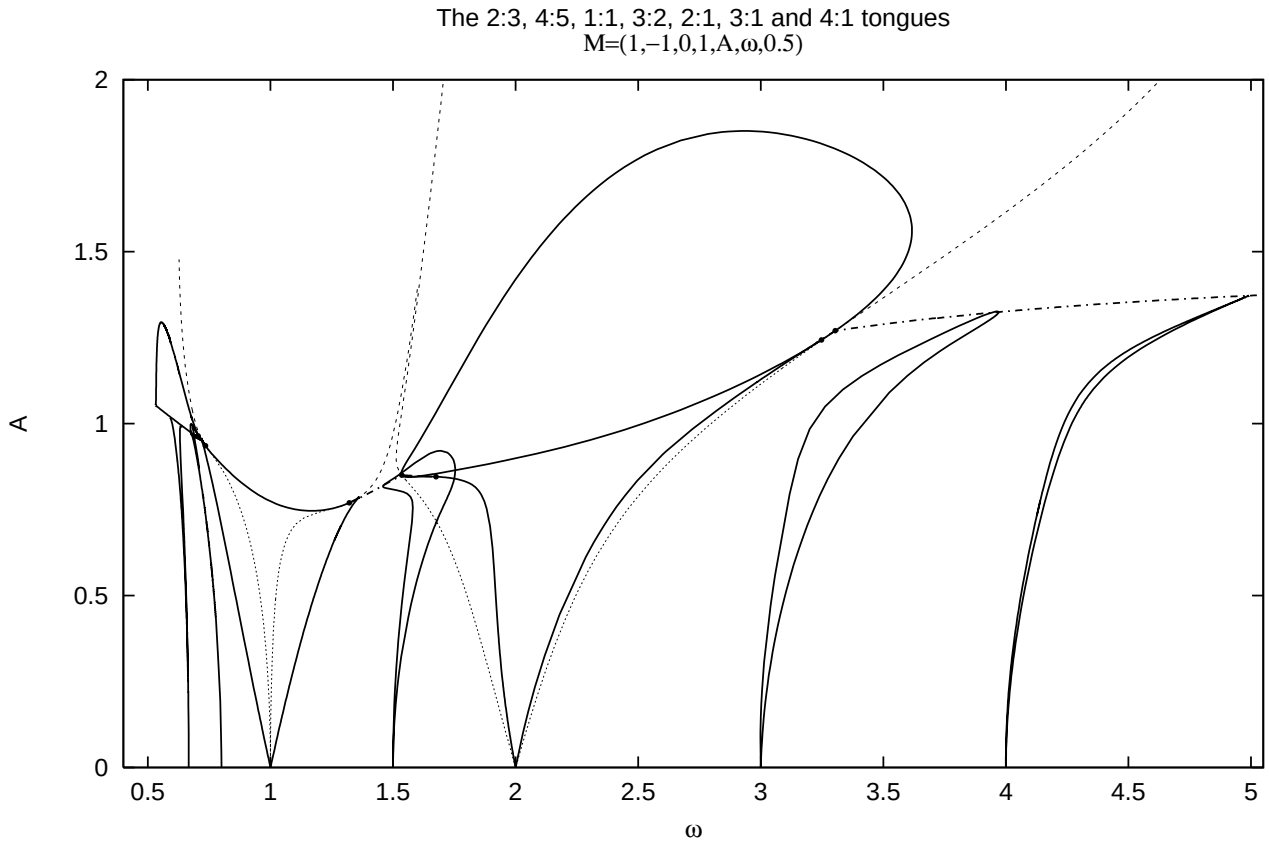

Figure 5.1 Excitation diagram. The solid lines are bifurcation curves either SN or PD, the dashed-dotted are T bifurcations, the dashed EE1+, and the dotted EE1- curves.

5.1.1 The T1 Curve and R^p Resonance Points

Most of the tongues close on- or around a curve of torus bifurcations where a stable torus collapses onto an enclosed unstable focus of period one (-F1), leaving behind only a stable focus of period one (+F1). Only few of the dominant tongues are observed to exist above this connecting curve at large forcing amplitudes ($A > 1$). TB and T-PD codimension two bifurcations mark the connection of the T1 curve to the 1:q and 2:q tongues. Each tongue has two such resonance points - one on each side.
Examinations of the 3:1, 3:2, 4:1, and 4:5 tongues show only one resonance point to be associated with each of these. The period three tongues close smoothly, overlapping the T1 line and enclosing the R^3 points. Another scenario is seen for the period four tongues. As the torus bifurcation line is approached, they gradually become narrower until they connect in the R^4 point on the T1 curve. These observations are in agreement with other numerical observations made by [Pavlou and Kevrekidis, 1992] and [Vance and Ross, 1989], and analytical examinations by [Norris, 1993] in which 4:q are claimed to close in wedges. [Pavlou and Kevrekidis, 1992] observe the SN4+ curves to stay below the T1 curve, but apparently there is some uncertainty as to the closure of the period four tongues. That the 4:q tongues are allowed to close in different ways relative to the T1 bifurcation curve is strongly supported by our numerical results in which differences are observed in the behaviour of the 4:1 and 4:5 tongues.

5.1.2 The Equal-Eigenvalues Curves

When tracing the bifurcation diagram in the (ω, A) plane, it becomes clear that focus-node transitions of *at least* the period one and two solutions must occur in the parameter plane. A quasiperiodic solution on a torus always encloses an unstable focus immediately after its birth, so the regions between the Arnol'd tongues contains such unstable period one solutions with complex conjugate eigenvalues. Since these undergo a torus bifurcation on T1, stable focus solutions exist above this line. No solutions whose corresponding eigenvalues are complex conjugates, can undergo neither a period doubling

nor a saddle-node bifurcation, so the observed bifurcation structure would be impossible were it not for the existence of these transitions. By methods described earlier, the locus of the focus-node transitions were traced in the (ω, A) plane. Even though they do not constitute a bifurcation of the solutions, their importance is evident, and they become no less interesting when one sees the tongue-like shape of the EE1 curves in Fig. 5.1. Closed loops of higher period equal-eigenvalues curves are also found, and are an intrinsic part of the bifurcation structure inside the tongues. The various equal-eigenvalues curves will be discussed briefly in connection with the presentation of the different entrainment regions.

As can be seen in the diagram, the EE1- curves emanate from the same point as the tongues. This is no coincidence, but not a must either. The unstable period one solution is known to be a descendant of the unstable equilibrium point of the autonomous system. This allows for the determination of the points on the ω axis from which the EE1- curves open. The eigenvalues evaluated at the autonomous equilibrium solution are $\mu(1+\alpha\mu\epsilon^2) \pm i\Omega$, so at zero amplitude the stroboscopic map shows this solution to have Floquet multipliers $\lambda_{1,2} = e^{(\mu(1+\alpha\mu\epsilon^2)\pm i\Omega)T_{forcing}}$. The tip of EE1- must originate where $Im\{\lambda_{1,2}\} = 0$. This is satisfied where $\Omega T_{forcing} = 2n\pi$ or $\Omega T_{forcing} = 2(n-1)\pi$. With $\Omega = 1$,

$$
\begin{aligned}
T_{forcing} &= 2n\pi \Rightarrow \omega = \frac{2\pi}{2n\pi} = \frac{1}{n} \qquad \text{or} \\
T_{forcing} &= (2n-1)\pi \Rightarrow \omega = \frac{2\pi}{(2n-1)\pi} = \frac{2}{(2n-1)}
\end{aligned}
$$

For $n = 1, 2, ...$ this coincides with the point of origin of the 1:1, 1:2,... tongues in the first case, and the 2:1, 2:3,... tongues in the latter case. This is specific for our system, as it depends on the parameters. [Kevrekidis et al., 1986] have determined similar equal-eigenvalues curves and found them to originate at points outside the tongues.

5.2 The 1:1 Tongue

At large forcing amplitudes the system entrains to the forcing in the simplest possible way in a 1:1 frequency locking. Intuitively, this is also what one would expect when the external perturbation is sufficiently strong.

When the forcing is of lower amplitude, the system behaves in a more diverse manner, as seen in Fig. 5.1, but also at these amplitudes the 1:1 entrainment is quite dominant. The 1:1 resonance tongue has a triangular shape, and opens at a larger angle than the other frequency locking regions.
The appearance of the tongue is deceptively simple, however. The outer boundary of saddle-node bifurcation curves encloses a variety of phenomena such as coexisting periodic and quasiperiodic solutions, global bifurcations, and the connection of codimension one bifurcation curves in codimension two points.

5.2.1 The Tongue Boundary

Fig. 5.2 shows the 1:1 Arnold tongue which consists of codimension one SN1+ and SN1- bifurcation curves to which T1 curves connect in the upper left and right corners.

Points, labeled A, B1, B2, and C, mark areas containing various types of solutions. In Fig. 5.3 and Fig. 5.4 these solutions are depicted in a one-parameter bifurcation diagram and four phase plots. A and C lie outside the tongue where no entrainment is observed. Points B1 and B2 both lie within the entrainment region but inside and outside of the equal-eigenvalues, horn respectively.
As can be seen in the bifurcation diagram, the quasiperiodic attractor disappears the instant a period-one saddle and stable node pair is born in an SN1+ bifurcation. The unstable period one focus continues through the tongue, but on a stretch inside the tongue it is an unstable node. This is when it passes through the EE1- region seen in Fig. 5.2. At the other side of the entrainment region, the S1,+N1 pair collides and disappears in another SN1+ bifurcation, leaving only the unstable period-one focus and a quasiperiodic attractor.

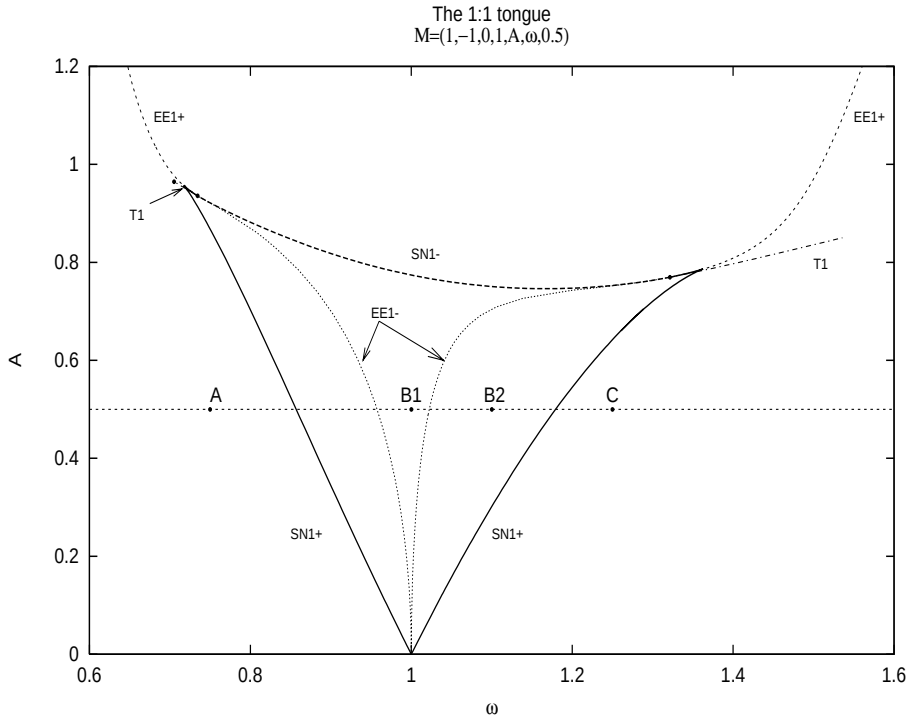

Figure 5.2 The 1:1 tongue and the period one Equal-Eigenvalues curves associated with it.

The scenario can also be followed in Fig. 5.4. These plots show the continuous and stroboscopic phase portraits of the stable and unstable limit cycles, and the quasiperiodic solutions. It is observed how the -F1 limit cycle lies inside the torus on both sides of the tongue.
The discrete points of the quasiperiodic attractors will eventually lie densely on a curve. This outlines the torus surface in the stroboscopic section and forms an invariant circle. In the two plots, A and C, an equal number of iterations are shown, clearly illustrating how the solution winds differently in the two cases. For the two quasiperiodic solutions the rotation number is

calculated to be 1.2995 and 0.8738 rotations per period of the forcing.

The appearance/disappearance of the saddle-node pair happens in a quite interesting fashion that is of consequence to the direction of the flow outside the tongue. At the point of the SN1+ bifurcation, the S1, +N1 pair appears on the invariant circle. Hence, the quasiperiodic attractor ceases to exist, but the invariant circle remains in the form of a heteroclinic connection of the saddle and stable node solutions. This is the scenario at low forcing amplitudes. Stroboscopic phase portraits of the solutions and their invariant manifolds are shown in Fig. 5.5, Fig. 5.6, and Fig. 5.7.

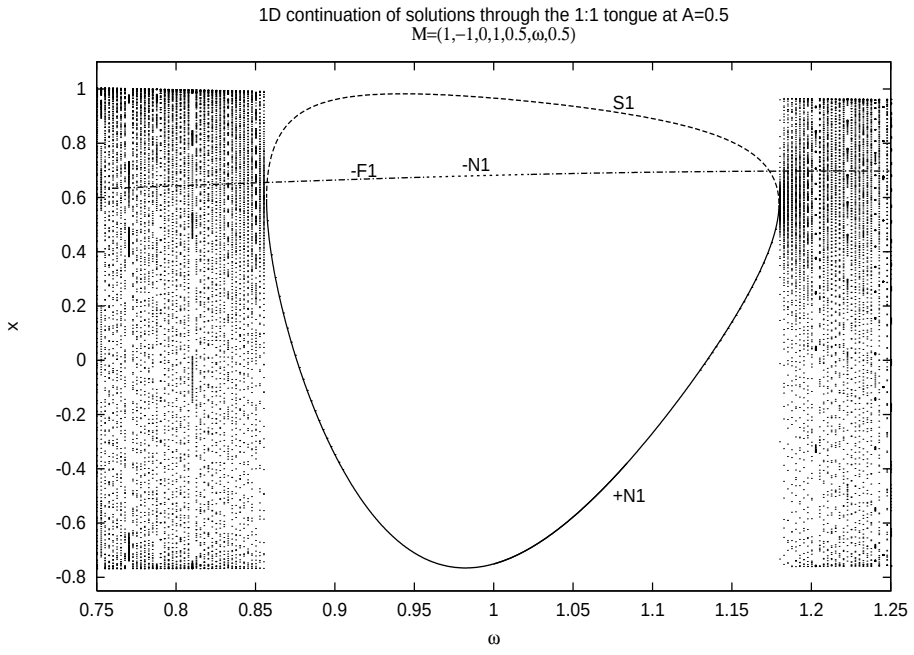

Figure 5.3 One parameter bifurcation diagram showing the co-existing period one solutions inside and just outside the 1:1 tongue at A=0.5. The quasiperiodic attractor is shown by dots obtained by Brute Force scan.

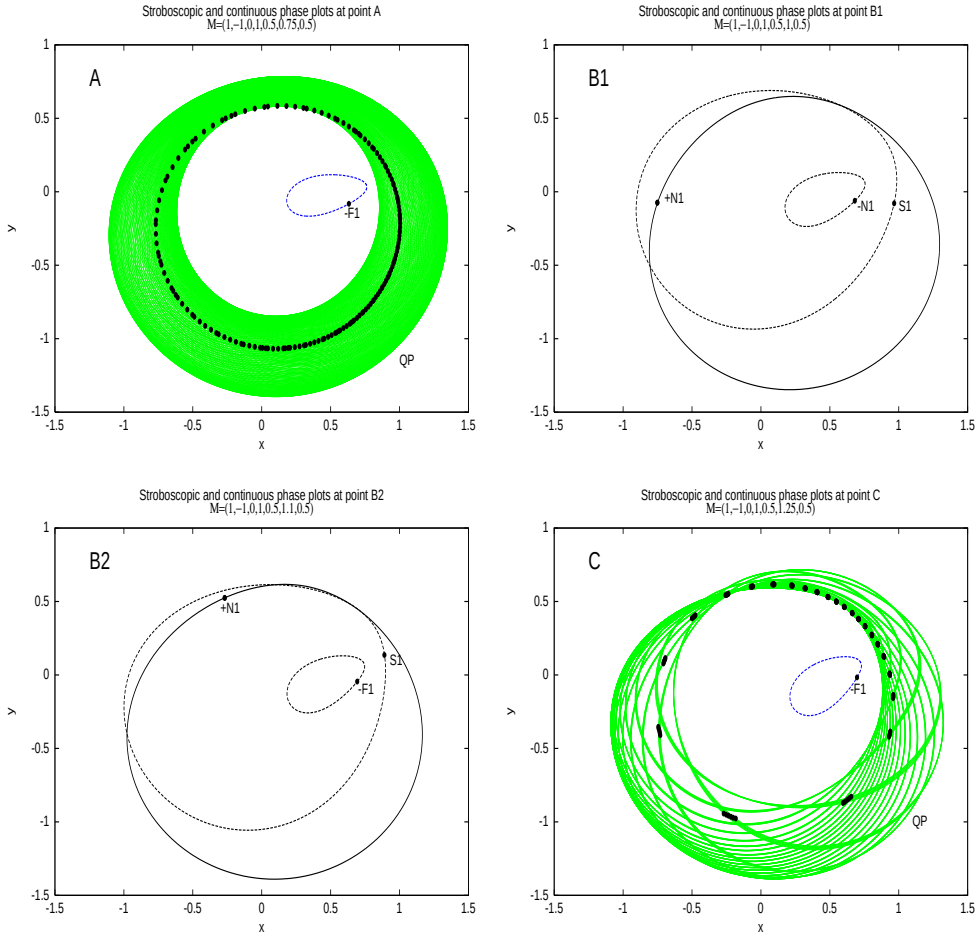

Figure 5.4 The stable and unstable periodic limit cycles and the quasiperiodic solutions are portrayed in the x-y plane. The solutions are obtained at the points marked A, B1, B2, and C in Fig. 5.2.

Fig. 5.5 corresponds to a point just inside the 1:1 tongue on the left side. The location at which the entrained period-one solutions appear can be seen in Fig. 5.4 - plot A, as a region on the invariant circle with a larger density.

This is a result of a 'slowing down' of the dynamics. As the forcing frequency is increased and the tongue traversed, the saddle and the node move around the invariant circle clockwise and counterclockwise respectively. Fig. 5.6 to Fig. 5.7 illustrate this. Fig. 5.7 is just prior to the SN1+ bifurcation on the right tongue boundary. Once again the point, at which the saddle-node pair collide, attracts a higher density of points on the subsequent torus seen in the last frame of Fig. 5.4.

A result of this movement of the solutions is a change in direction of the flow on the quasiperiodic attractors on the two sides of the tongue. It cannot be seen in Fig. 5.4, but the flow on (and toward) the torus is counterclockwise in A and clockwise in C. If the unstable manifolds of the saddle point in Fig. 5.5 - Fig. 5.7 are compared, the directional change is seen to correspond to the change in the flow along these invariant sets as the tongue is crossed.

Smooth invariant circles, of the kind seen in the previous, exist in a large part of the tongue, but there are regions at higher amplitudes where they become increasingly irregular, leading to the homoclinic and heteroclinic crossing of the manifolds. This is the topic of Section 5.2.3.

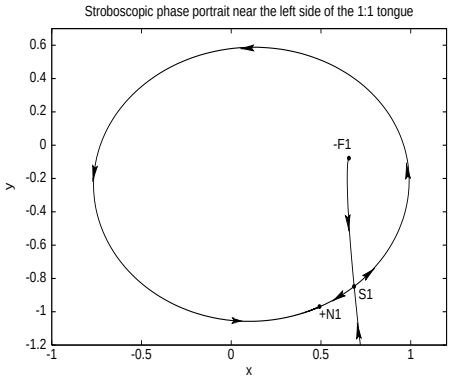

Figure 5.5

The invariant circle formed by the heteroclinic connection of the saddle and the unstable node. The plot is shortly after the appearance of the saddle-node pair on the torus seen in Fig. 5.4(Point A)

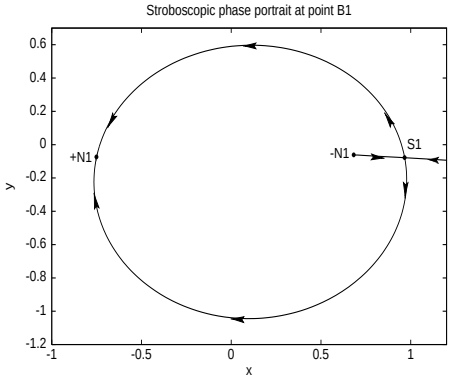

Figure 5.6

The invariant circle at the point B1 in Fig. 5.2. The saddle and node points are moving around the invariant circle counterclockwise and clockwise, respectively.

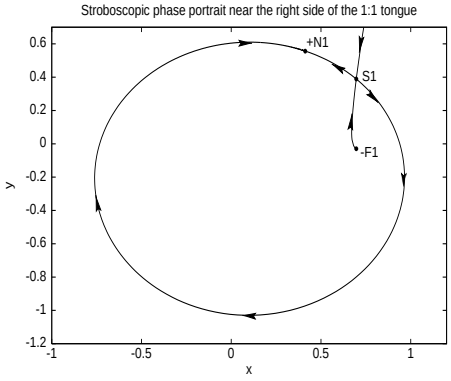

Figure 5.7

The invariant circle at the right side of the tongue just before the two points disappear in the saddle-node bifurcation, leaving behind the torus depicted in Fig. 5.4(Point C).

5.2.2 The Top of the Tongue

The 1:1 tongue is seen to have an upper bound of SN1- bifurcations closing it. Above this we still have 1:1 entrainment, but only stable node and focus orbits of period one exist - there are no saddle solutions. As discussed, this high amplitude region of stable 1:1 entrainment is bounded mainly by torus bifurcation lines.

On the 'lid' of the tongue the T1 curves connect to the SN1 curves. The Floquet multipliers define the points of connection to be R^1 resonance points, but they are also Takens-Bogdanov points. There is one TB point on each side of the lid, and the T1 bifurcation lines extend from these to the neighbouring 2:3 and 2:1 tongues, to which they also connect in codimension two points (T-PD/R^2).
The plots in Fig. 5.8 are magnifications of the upper left and right corners respectively. The figures show the same scenario to take place on both sides; the side and top saddle-node bifurcation curves meet in a cusp close to which a T1 curve connects tangentially in the TB point and marks the transition between SN1+ and SN1- bifurcations. The lid thus consists of both types of saddle-node bifurcations. Also plotted are the equal-eigenvalues curves.

Since the left and right corners are of similar structure, only the left side has been examined. One effect of the T1 line crossing the side of the tongue is the coexistence of quasiperiodic and stable periodic attractors inside it. This scenario is found for ω values to the left of the TB point, i.e. where the lid consists of SN1+ bifurcations and the torus bifurcation curve lies beneath it. Fig. 5.9 to Fig. 5.11 show one parameter bifurcation diagrams using the amplitude as bifurcation parameter. The diagrams are obtained on either side of the codimension two point. The solution-curves are followed by means of the one-dimensional continuation scheme and have been supplemented by Brute Force scans showing the non-periodic attractors.

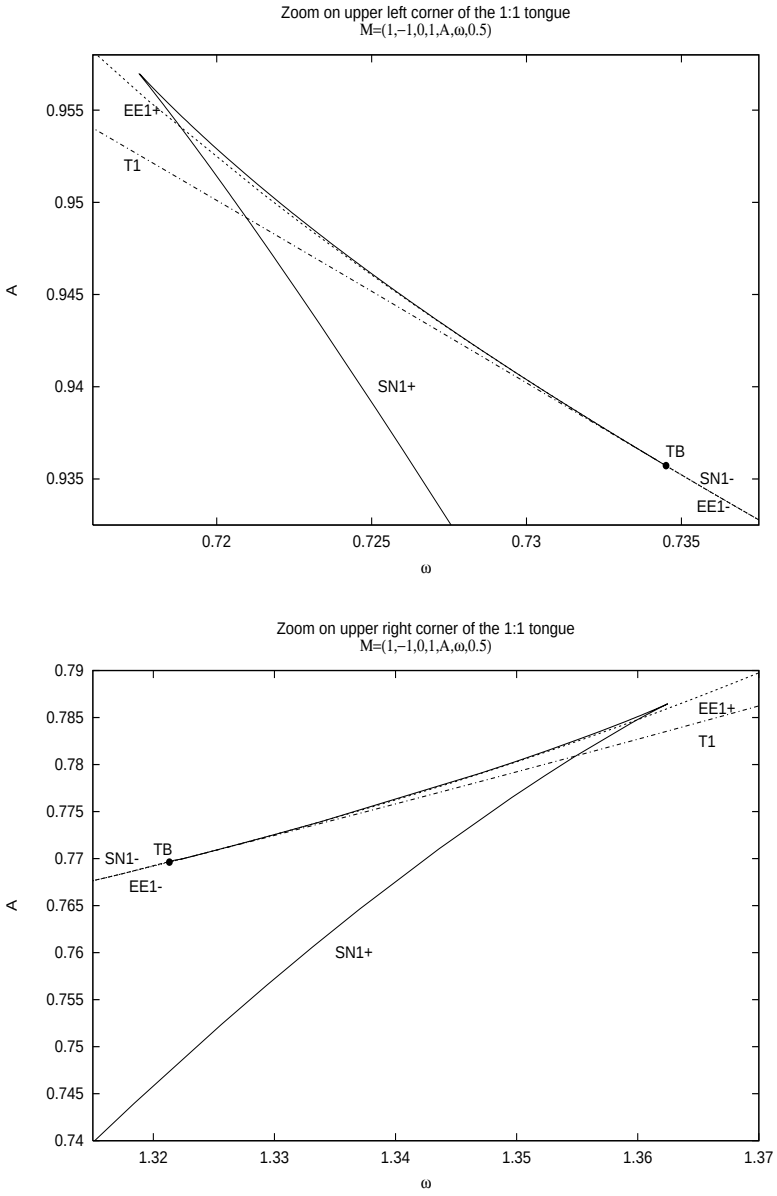

Figure 5.8 Magnification of the upper left and right corners of the 1:1 tongue illustrating the connection of the period one torus (Neimark-Sacker) bifurcation curve to the saddle-node boundary. Shown are also the period one equal-eigenvalues curves.

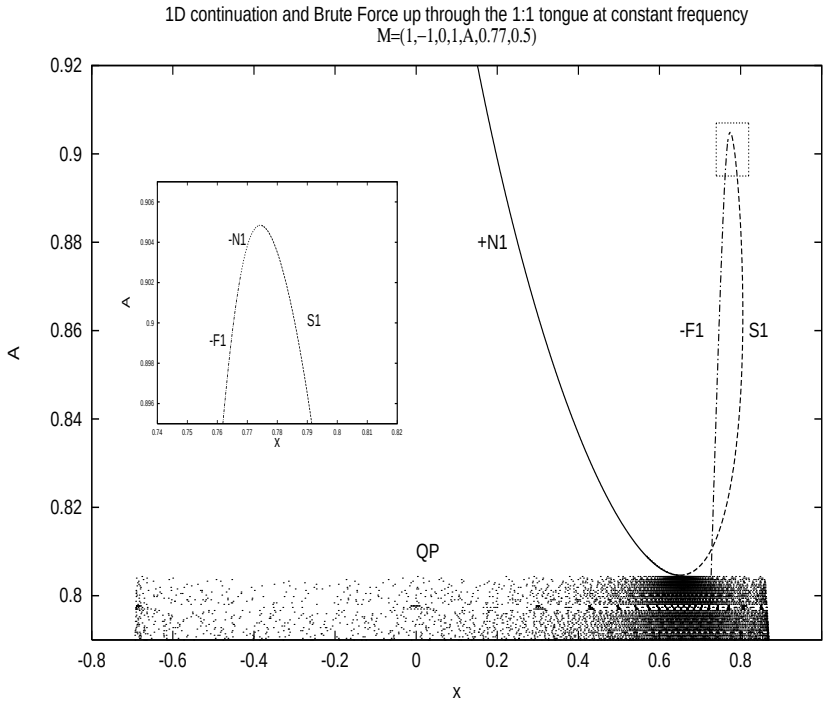

Figure 5.9 One-dimensional bifurcation diagram at $\omega = 0.77$ through the left part of the 1:1 tongue, but to the right of the left most TB point. The subfigure is a magnification of the SN1- bifurcation.

Fig. 5.9 is at a forcing frequency of 0.77, to the right of the Takens-Bogdanov point.
Starting at the bottom of the diagram is a stretch of quasiperiodic and unstable focus solutions. At an amplitude just above $A = 0.8$ the first saddle-node bifurcation is encountered. This is on the SN1+ curve constituting the left side of the tongue. The bifurcation scenario is the same as described in Section 5.2.1 with the S-N pair emerging on the invariant circle. Above this point three solutions exist; a stable node +N1, a saddle S1, and the unstable focus -F1. Following the -F1 solution for increasing amplitude, the lid of the

tongue is approached. As can be seen in the inset, the solution changes type prior to reaching the top SN bifurcation curve. This is when the EE1- curve is crossed. The unstable node collides with the coexisting saddle in an SN1-bifurcation, leaving only the +N1 solution at higher amplitudes.

In a similar scan to the left of the codimension two point, the torus bifurcation curve is also crossed. Fig. 5.11 clearly shows the effect of this. In addition to the quasiperiodic attractor outside the tongue one such also exists inside

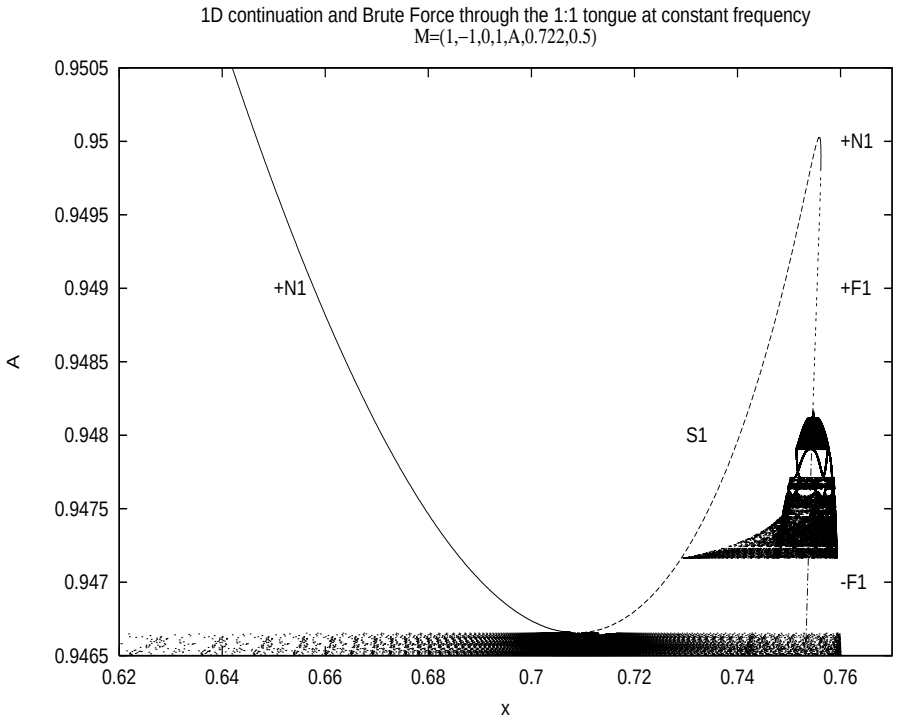

Figure 5.10 One-dimensional bifurcation diagram at $\omega = 0.722$. The scan is to the left of the Takens Bogdanov point and illustrates the emergence and destruction of a quasiperiodic attractor inside the 1:1 tongue.

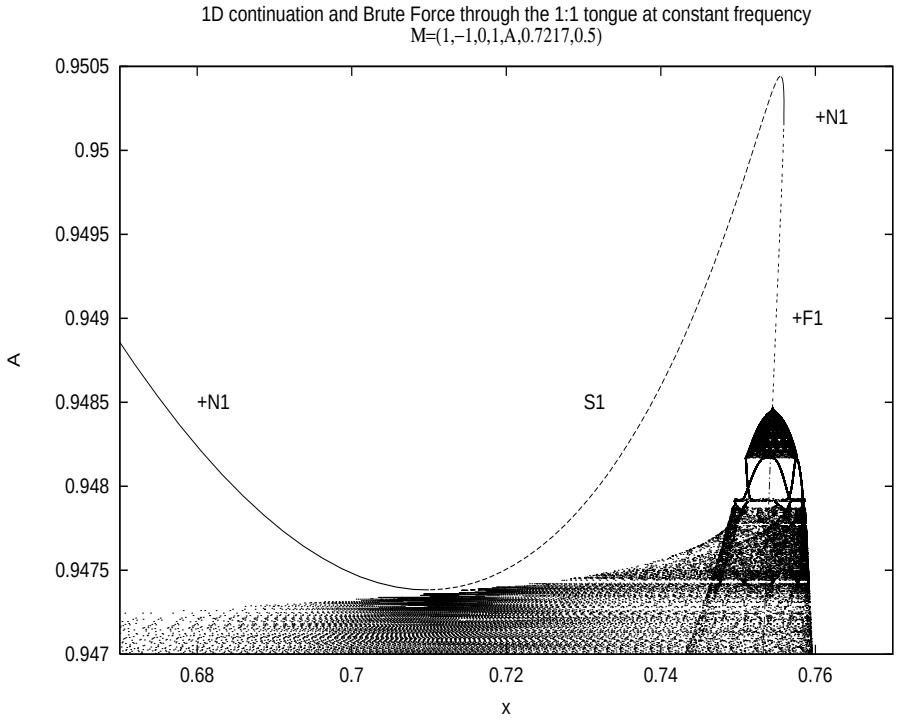

Figure 5.11 One-dimensional bifurcation diagram at $\omega = 0.7217$. The scan is to the left of the Takens Bogdanov point where the curve of global bifurcations no longer exists. Note the difference in the lower saddle-node bifurcation compared to Fig. 5.9 and Fig. 5.10.

the tongue. It encircles the unstable focus and exists simultaneously with the saddle-node pair. The Brute Force scan inside the tongue also shows other attractors to exist. Amongst these is seen a window of stable period-five solutions. This is due to other smaller tongues overlapping the 1:1 tongue. The BF method converges to these solutions, but they are not part of the period-one entrainment scenario as such.

The attractor disappears abruptly in a catastrophic bifurcation. In Fig. 5.10 this is seen to happen when the attractor collides with the saddle solution. This is actually a collision with the unstable invariant manifold of the saddle, an event discussed in more detail in Section 5.2.3. At an amplitude of approximately 0.9482, the -F1 solution becomes stable in the torus bifurcation. Since the focus is now stable, the bifurcation closing the tongue must be an SN1+. This clearly illustrates how the saddle-node bifurcation changes in the Takens-Bogdanov point. The EE1 curve will be discussed later.

Moving even further toward the corner of the tongue the global bifurcation disappears. Also a change in the lower SN1+ bifurcation is observed. Instead of the saddle-node pair appearing on the torus, forming an invariant circle, their emergence does not cause the destruction of the quasiperiodic attractor. In addition to this, there is no collision involving the quasiperiodic attractor, and thus the saddle-node pair coexists with this most of the way to the torus bifurcation. This scenario is seen in Fig. 5.11. Hence, it must be concluded that the global bifurcation curve has ended prior to this point. The bifurcation curve cannot cross the T1 curve and must thus have connected to the lower SN1+ curve in a point that shall be referred to as a G-SN point.

In accordance with Fig. 5.11 and Fig. 5.10, the G-SN point marks the transition from the S,+N1 pair emerging *on* the invariant circle to it happening *off* the invariant circle.

5.2.3 The Global Bifurcations

To examine the global bifurcation scenario in greater detail once again consider Fig. 5.10 and compare this with the various stages of manifold dynamics illustrated in Fig. 5.12. The first frame is at an amplitude above the torus bifurcation just below the uppermost SN1+ bifurcation. The unstable manifolds of the saddle point end in the two +N1 points, one of which is close to a collision with the saddle point. When the amplitude is reduced the EE1+ curve is crossed and the latter node becomes an +F1 point (frame 2).

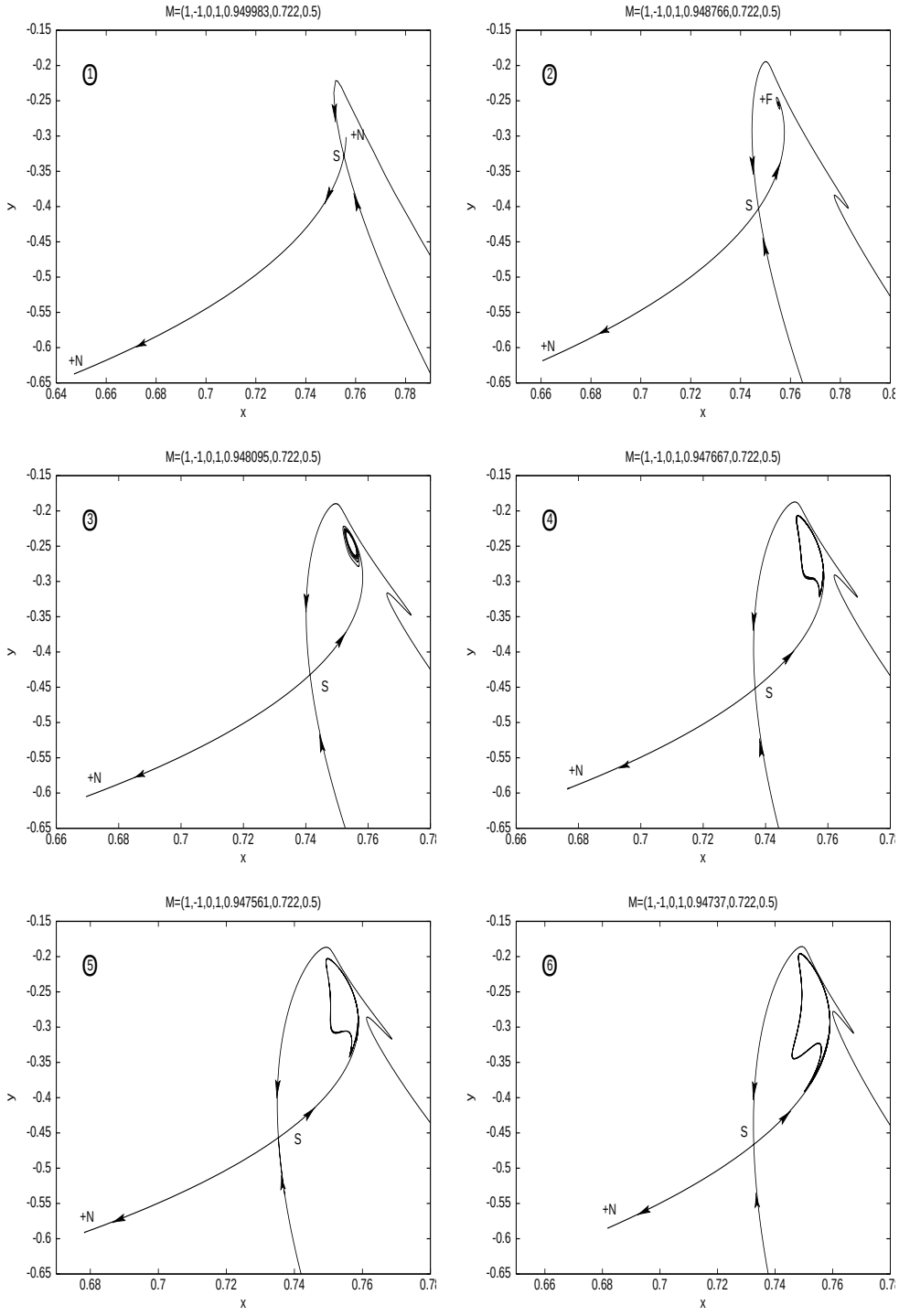
M=(1,-1,0,1,0.949983,0.722,0.5)
①
+N
S
+N
M=(1,-1,0,1,0.948766,0.722,0.5)
②
+F
S
+N
M=(1,-1,0,1,0.948095,0.722,0.5)
③
S
+N
M=(1,-1,0,1,0.947667,0.722,0.5)
④
S
+N
M=(1,-1,0,1,0.947561,0.722,0.5)
⑤
S
+N
M=(1,-1,0,1,0.94737,0.722,0.5)
⑥
S
+N
x
y

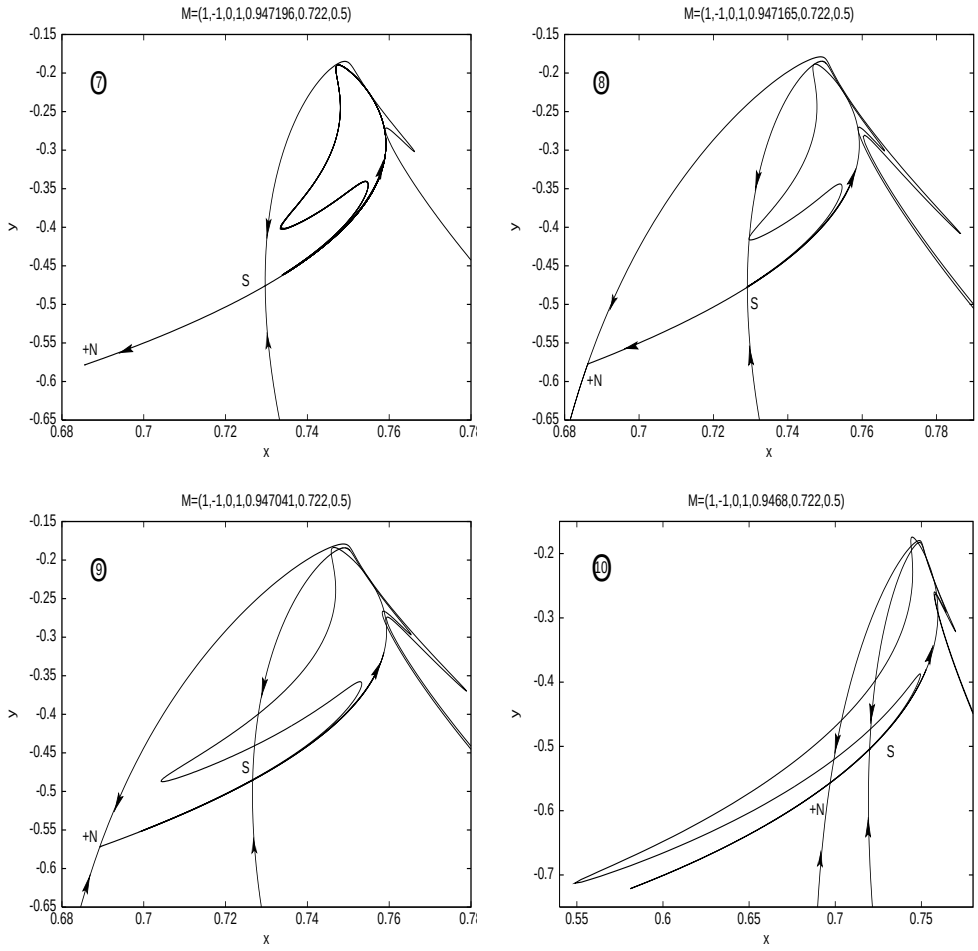

Figure 5.12 Series of phase portraits illustrating the homoclinic and heteroclinic crossing of the manifolds. The plots show the phase dynamics corresponding to various points of decreasing amplitude in Fig. 5.10.

The focus becomes unstable through the T1 bifurcation and the quasiperiodic attractor emerges around it (frame 3). The unstable manifold now winds around this attractor approaching it asymptotically.
Just after its birth, the quasiperiodic attractor is still rather smooth, as can be seen in the third frame. As the forcing amplitude is reduced, the invariant circle expands and becomes increasingly folded, developing 'fingers' that stretch out. Since the unstable half-manifold encircles/bounds the attractor it also takes on this shape (frames 4-7).
The stretching and folding taking place are characteristics of chaotic dynamics. Hence, it is likely that we have a torus breakdown leading to a chaotic attractor. This is in accordance with [Knudsen et al., 1991] who located such an attractor in a similar scenario.

The tips of the folded invariant circle move closer and closer to the stable half-manifold of the saddle. By frame eight, the forcing amplitude has been reduced to a point at which they touch. Frames seven and nine are just prior to and after the *homoclinic crossing* of the unstable and stable manifolds. The initial contact occurs simultaneously at several points along the manifold. If one follows the iteration of points along the invariant manifold, it becomes clear, that the contact points are connected by subsequent iterations.

It is not completely evident from looking at the figure, but the initial crossing leads to an infinite number of crossings in which the unstable manifold becomes increasingly folded and stretched as it approaches the saddle along the stable manifold (frame 9). This is a so-called *homoclinic tangle*. Any contact with the invariant inset of a saddle corresponds to a contact with the saddle point itself and leads to the destruction of a stable attractor. The homoclinic tangle is thus associated with the destruction of an attractor in a *catastrophic* bifurcation.

In the last three frames the strong stable manifold of the stable node has been included. In addition to the stretching of the unstable manifold, the saddle and stable node move closer to each other as the lower SN+ bifurcation is approached. Between frames 9 and 10 a *heteroclinic crossing* of the unstable manifold of the saddle and the strong stable manifold of the node takes place

and a *heteroclinic tangle* is formed. Homo- and heteroclinic orbits are seen to coexist. The tangles unfold one by one, as the amplitude is further decreased, to finally form an invariant circle.

In order to illustrate the unfolding/folding into a smooth invariant circle, the examinations of the manifolds are moved to a slightly greater frequency.

At $\omega = 0.73$, with increasing forcing amplitude from below the 1:1 tongue, a quasiperiodic attractor is destroyed as the SN1+ bifurcation occurs. The manifolds of the saddle-node pair form an invariant circle as the amplitude is further increased. Fig. 5.13 illustrates how the quasiperiodic attractor just outside the 1:1 tongue is practically coinciding with the manifolds of the saddle and the stable node inside the tongue.

As A increases, the invariant circle loses smoothness and develops a cusp. Fig. 5.14 illustrates how the invariant circle gradually changes, as it gets closer and closer to the heteroclinic connection. The figure includes unstable manifolds of the saddle at different values of A. Stable manifolds of the saddle and the strong manifolds of the node are also presented, but only those corresponding to the initial case where the deformation of the circle

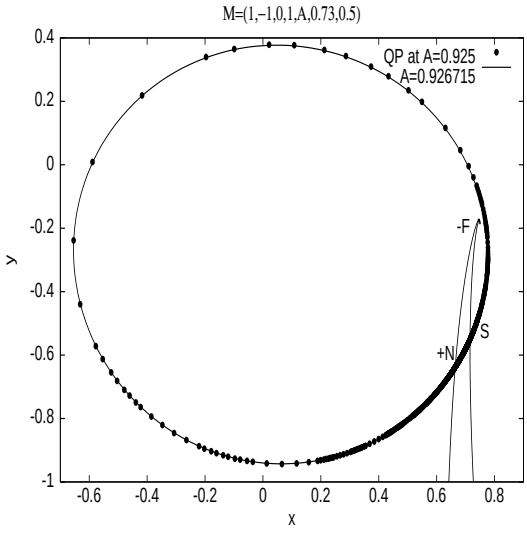

Figure 5.13

A quasiperiodic attractor is plotted along with the manifolds of a saddle-node pair existing at a slightly greater amplitude.

has just begun. Naturally, the fixed points move in the state space as A is varied. The unstable focus within the invariant circle moves closer to the rim of it, while the saddle approaches it from beneath. The stable node moves back and forth in the interval $0.4 < x < 0.6$.

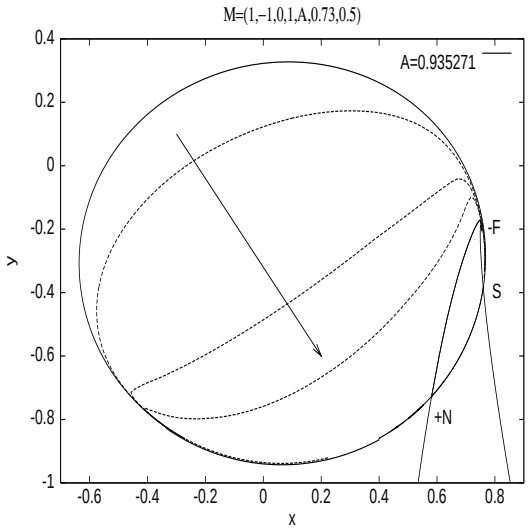

Figure 5.14

The invariant circle deforms as it approaches the heteroclinic connection.

The unstable manifold of the saddle eventually connects with the strong manifold of the stable node and the heteroclinic tangle is created. The tangle is presented in Fig. 5.15. No homoclinic tangle is present yet, only an heteroclinic orbit exists. The figure includes a zoom near the unstable focus, illustrating that the manifolds tangle both near the stable node - and near the saddle. Similar observations concerning the deformation of the invariant circle have been made by [Pavlou and Kevrekidis, 1992] and [Vance and Ross, 1989].

Vertical scans through the corner of 1:1 entrainment region located only one heteroclinic and one homoclinic transition. The set of these connect to the lower SN1+ curve in the G-SN point somewhere in the interval $0.7217 < \omega < 0.722$.

Fig. 5.16 illustrates the location of global homoclinic and heteroclinic connections in parameter space. In the figure, shaded areas indicate where homo-

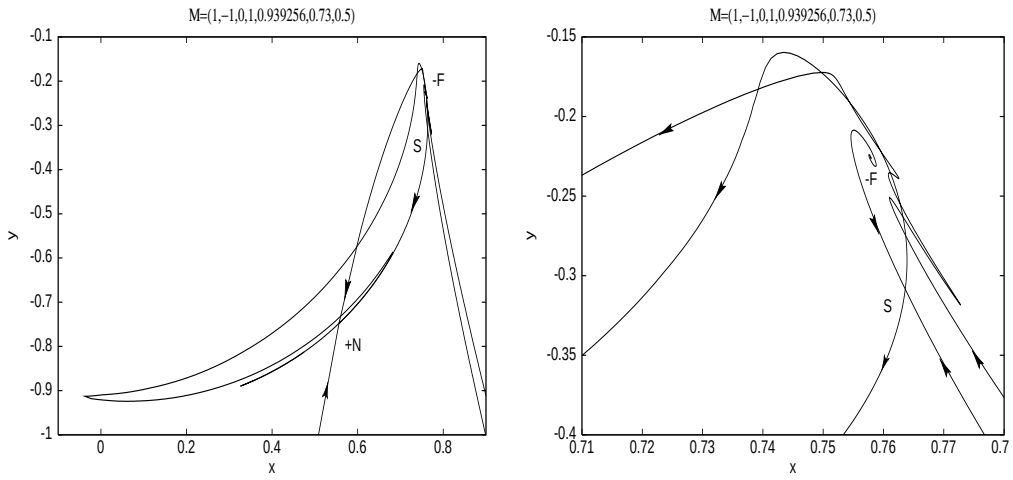

Figure 5.15 The heteroclinic tangle between the unstable manifold of a saddle and the strong manifold of a stable node.

and heteroclinic tangles, and thus orbits, exist. Near the connection point the shading is darker indicating that they where found to coexist.

The homoclinic bifurcation set originates at the TB point and must stay beneath this curve. In this work the point of termination of the heteroclinic transition curve has not been examined in detail, but it is assumed to connect to the SN1- bifurcation curve. [Pavlou and Kevrekidis, 1992] and [Vance and Ross, 1989] have traced the heteroclinic transition curve in a similar scenario, and in both cases it is estimated to connect on the SN1- lid of the tongue. The G_{he} curve is able to cross the EE1- curve that lies 'beneath' the SN1- bifurcation. Note that the heteroclinic curve could have terminated on a EE1+ curve. Then the stable fixed point would changes from a node to a focus, in effect destroying its strong invariant stable manifolds.

The 1:1 tongue has the same structure in both its corners. Therefore, it is possible to find a similar global bifurcation scenario near the upper right cusp of the tongue.

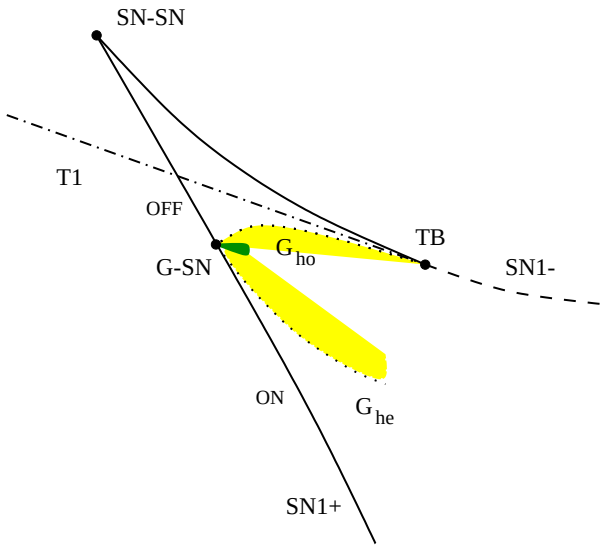

Figure 5.16 Schematic illustration of the regions of homo- and heteroclinic tangles. G_{ho} indicates the homoclinic bifurcations curve and the shaded area just below the part of the parameter plane in which homoclinic orbits exist. Likewise G_{he} indicates the heteroclinic transition and the shaded area just above a region of heteroclinic orbits. The darker shaded area near the G-SN point is a region of coexisting homo- and heteroclinic orbits. The labels ON/OFF indicate where the SN1+ bifurcation occurs on or off the invariant circle.

5.2.4 The Equal-Eigenvalues Curves

Before ending the discussion of the 1:1 entrainment region, some final comments are made regarding the associated period-one equal-eigenvalues curves. There are many ways in which the observed structures can be described. One way of viewing the EE1 transition in the 1:1 tongue, is as a necessary prerequisite to the saddle-node bifurcations constituting the upper bound. Since the period-one solution is a focus outside the tongue it *must* change to a node before turning on the lid.

It has already been established where on the ω axis the curves emerge and how this can be explained. Due to the nature of the equal-eigenvalues transitions they are often found in association with torus bifurcations. Consequently, they are also closely related to the various codimension two bifurcation points involving torus bifurcations. The fact that they run inside the 1:1 tongue is a consequence of the location of the Takens-Bogdanov points through which the EE1 curves are observed to pass on either side.
In the TB points they change from EE1- to EE1+. This must be so since the T1 bifurcation changes the unstable focus to a stable focus, or put another way, because of the change in the type of saddle-node bifurcation above this line.

5.2.5 Summary

- The structure of the 1:1 Arnol'd tongue was examined. It had a triangular shape and its boundary consisted of SN bifurcations; the sides of SN1+ bifurcations, and the lid primarily of SN1- bifurcations.
- Above the SN lid, the 1:1 entrainment region was bounded primarily by curves of period-one torus bifurcations. These connected to the upper SN curve in Takens-Bogdanov codimension-two points. These points are also R^1 resonance points of the T1 curve.
- At low amplitudes the period-one saddle and node solutions were born on a smooth torus. As the tongue was traversed, these were observed to move around the invariant circle in opposite directions. This caused the flow on the invariant circle to change direction.
- A global bifurcation scenario was examined in the upper left corner of the tongue. Based on these examinations a schematic bifurcation diagram was presented. Homoclinic and heteroclinic orbits were found to coexist near the connection point of the global bifurcation curve on the side of the tongue.
- The period-one equal-eigenvalues curves associated with the 1:1 tongue were discussed. They were seen to change type when passing through the TB points tangent to the SN curve.

5.3 The 2:1 and 2:3 Tongues

This section contains a discussion of the period two entrainment regions. The structure of these are exemplified by calculations of the bifurcation diagrams of the 2:1 and 2:3 tongues. The focus will mainly be on the 2:1 tongue where the numerical analysis has been carried out in detail.
In addition to the usual tongue boundaries consisting of saddle-node bifurcations, the upper bound of the period-two tongues consist of closed loops of period-doubling bifurcation curves. Phase-locked period-two solutions are thus primarily obtained either through the transition from quasiperiodicity via an SN2 bifurcation or by a period-doubling of the high amplitude 1:1 locked solutions.

Like the 1:q tongues, the 2:q tongues have a period-one equal-eigenvalues horn associated with them. These are included in Fig. 5.1. This figure does, however, only show the tip of the iceberg. The bifurcation diagram in Fig. 5.17 shows the 2:1 tongue in detail which includes equal-eigenvalues transition curves of period-two solutions, period-two torus bifurcation curves, a nested loop of period-doubling loops leading to chaos, and various codimension two connections of bifurcation curves.

5.3.1 The Tongue Boundary

At low forcing amplitudes, the 2:q tongues are qualitatively similar to the 1:q tongues. The tongue boundary, which consists of SN2+ bifurcations. It originates at a forcing frequency equal to the p/q ratio and becomes wider as the forcing amplitude is increased. Like the 1:1 tongue there is also a transition from saddle-stable-node to saddle-unstable-node bifurcations at a Takens-Bogdanov codimension two point. Unlike the period-one tongues this does not happen on the upper bound of the entrainment region but on the sides. The TB point is located at relatively high values of the forcing amplitude where the scenario becomes much different from the one observed in the 1:1 tongue. At amplitudes slightly higher than the TB point, the SN2 curves connect to the period-doubling loop which then acts as the tongue boundary.

In Section 5.3.4 is considered how the connections of codimension one curves can take place relative to each other. We believe at least three different scenarios to be possible, two of which have been confirmed through our numerical computations. A one parameter bifurcation diagram, corresponding

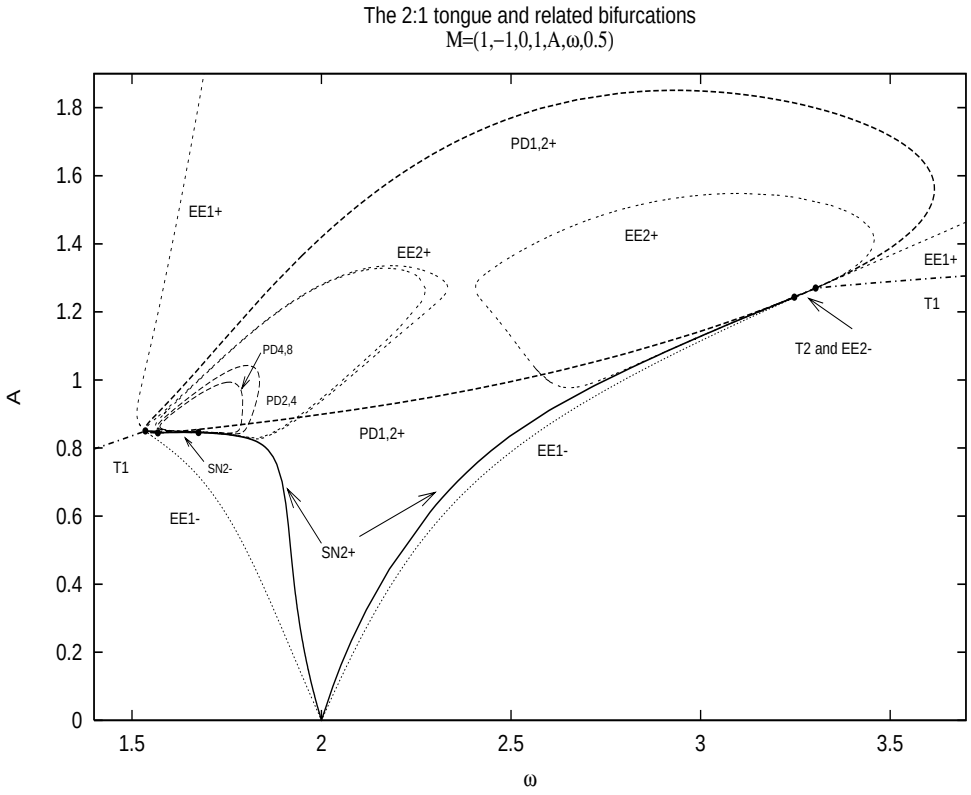

Figure 5.17 The 2:1 tongue and the main bifurcation and equal-eigenvalues curves associated with it.

to a horizontal cut through the tongue, is shown in Fig. 5.18. It is seen to be somewhat similar to Fig. 5.3 in the sense that stable solutions appear simultaneously with the disappearance of the quasiperiodic attractor. Fig. 5.19

confirms the similarities in the birth of the saddle and node solutions and the change in rotational direction as the tongue is crossed. The difference in pairing on the two sides of the tongue is a necessary result of their occurrence on the same invariant circle. Here it is mainly the +N2 solutions that move around the invariant circle, and their intersection in Fig. 5.18 marks the frequency at which they lie at the same x-coordinate but on opposite sides of the circle. This is at approximately $\omega = 2.13$ and is seen in the third frame of Fig. 5.19.

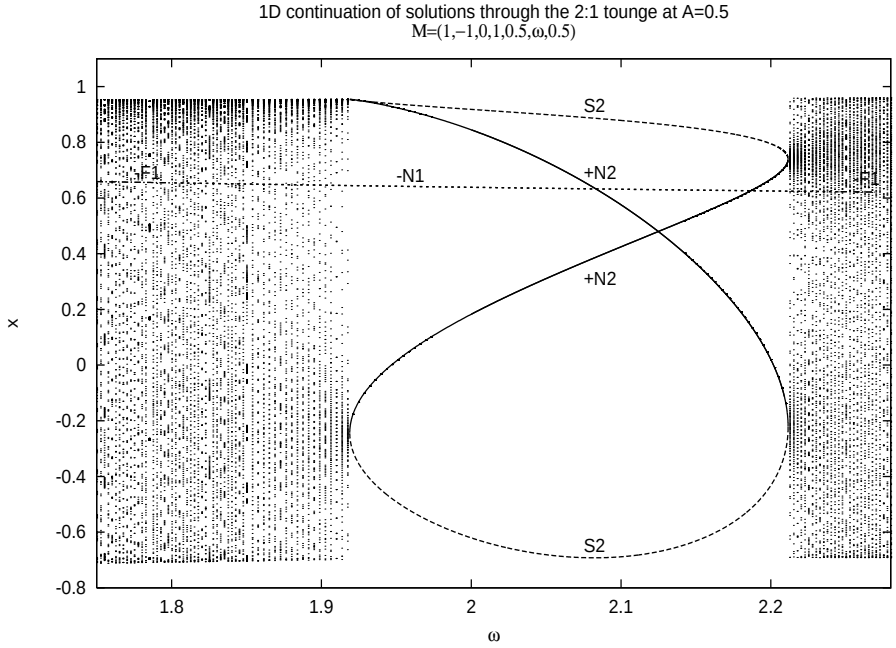

Figure 5.18 One parameter bifurcation diagram showing the co-existing period-one and two solutions inside and just outside the 1:1 tongue at A=0.5. The quasiperiodic attractor is shown by dots obtained by Brute Force scan.

Once again the unstable period-one solution can be traced through the

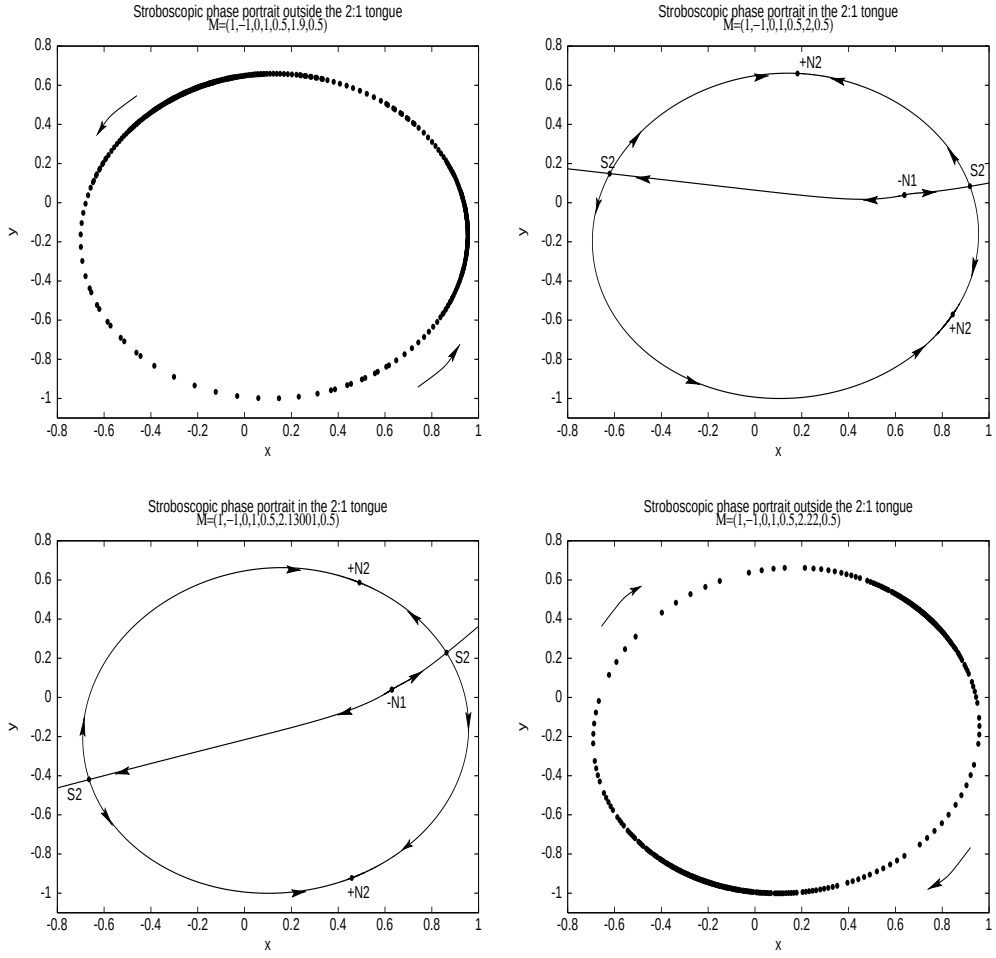

Figure 5.19 Stroboscopic phase portraits through the 2:1 tongue at A=0.5. It is seen how the quasiperiodic attractor and the invariant manifolds form a similar invariant circle. The third frame corresponds to the crossing of the +N2 solutions in Fig. 5.18.

tongue and is seen to undergo a change in solution type, as the EE1- curve is crossed. Unlike the 1:1 scenario this curve now lies on the outside of the Arnol'd tongue, hence, only a -N1 solution is found inside.

5.3.2 High Amplitude Bifurcation Structure

At amplitudes above 0.8 the 2:1 tongue displays quite complex behaviour. Even though it is not obvious from Fig. 5.17, the two sides of the tongue are in most respects qualitatively similar. On the right side, the bifurcation curves lie very close and are hard to distinguish. Details of the diagram are thus illustrated near the left boundary.

A magnification of the lower left part of the PD1,2 loop reveals important

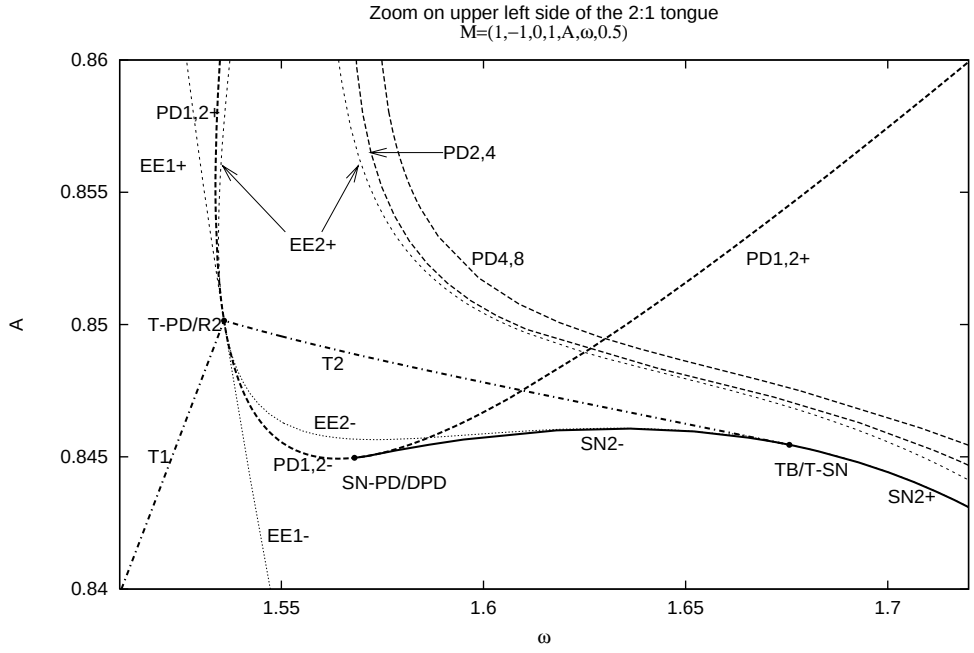

Figure 5.20 Magnification of the lower left part of the Period-doubling loop.

details of the bifurcation diagram. In Fig. 5.20 this is seen to be an area where many of the bifurcation curves come together in various types of codimension two points. The general nature of these points were discussed in Chapter 2. Postponing a discussion of the equal-eigenvalues curves for later, the solutions in the vicinity of the codimension two points will now be examined.

The Takens-Bogdanov Point

The T2 curve extends from the T-PD/R2 point and connects to the curve of saddle-node bifurcations in a Takens-Bogdanov point. The diagram in Fig. 5.21 shows the locations and bifurcations of the period-one and two solutions to the right of this point. The solutions are traced all the way to the top of the PD1,2 loop and so, in order to see the details relevant in the context of Fig. 5.20, a magnification of the bottom has been included.
Starting at the top of the loop, the stable node loses stability in the PD1,2+ bifurcation and continues as a saddle solution through the PD loop. The stable period-two node born in the bifurcation becomes a stable focus in a very short interval, returns to a stable node, and then becomes a saddle in a PD2,4+ bifurcation. No solutions of a period higher than two are plotted, as it would crowd the bifurcation diagram. The fates of the S1 and S2 solutions are seen in the magnification.
In the bottom frame of Fig. 5.21 the solutions can be followed as they cross the bifurcation curves displayed in Fig. 5.20. The S2 solution continues down to an amplitude of approximately 0.846. Here it once again becomes a stable node as it crosses the bottom of the PD2,4 bifurcation loop (indicated with an arrow in the figure). Before reaching the SN2+ tongue boundary, the solution must pass through the narrow space between two EE2+ loops inside which it is a stable focus. The outermost EE2+ loop lies very close to the SN2+ curve. This causes the emerging stable node to exist only a very short period of time before it collides with a period-two saddle.

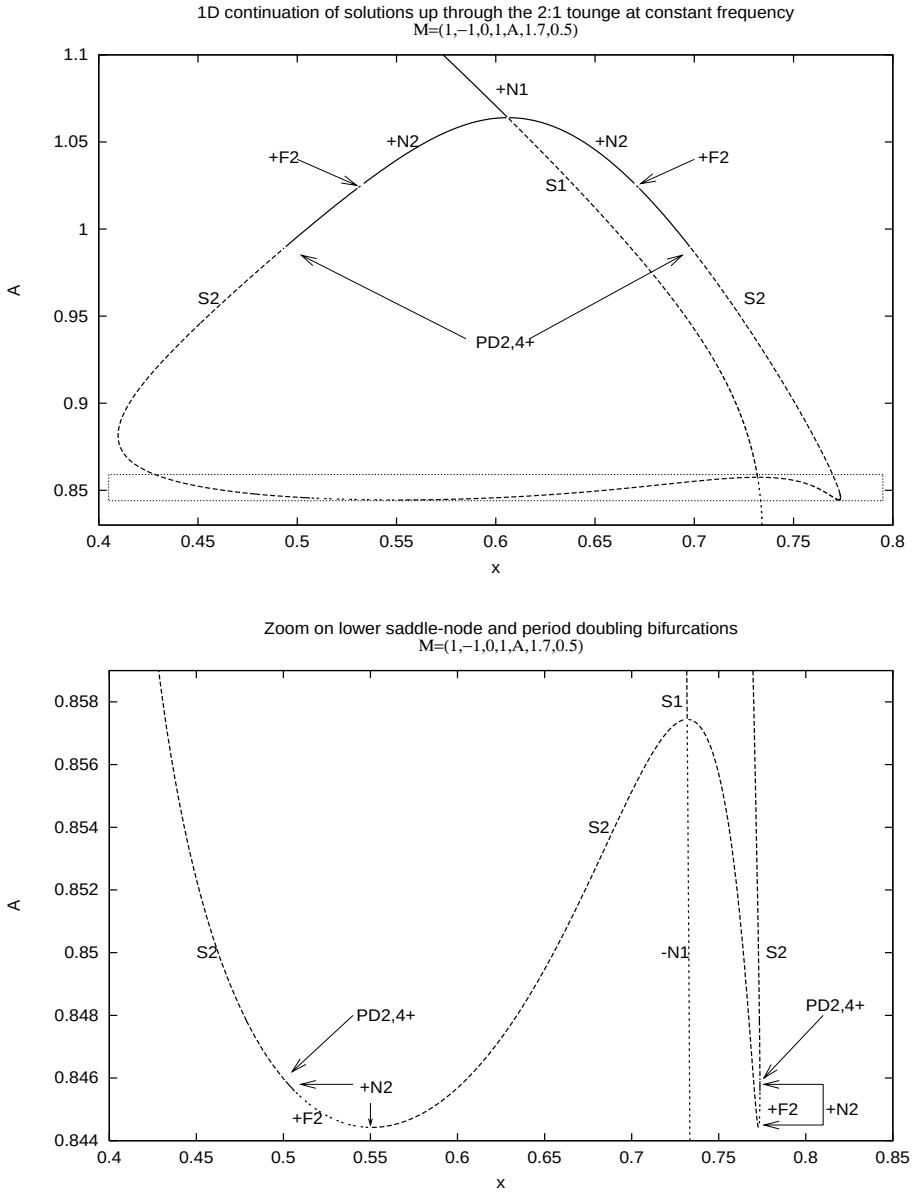

Figure 5.21 Co-existing period-one and two solutions in the 2:1 tongue at $\omega = 1.7$ - to the right of the Takens-Bogdanov point. The magnification illustrates the PD1,2+ and SN2+ bifurcations.

Since the +N2 solution is difficult to see in the small interval, it has been marked by arrows in addition to the label. The S2 solution with which it collides is born in the supercritical period-doubling of the S1 curve at an amplitude just below 0.858. This is at the bottom of the large PD1,2 loop.

To the left of the TB point a different set of bifurcations is encountered. The changes occur only at forcing amplitudes in the vicinity of the TB point, and can be seen in Fig. 5.22. Tracing the solutions from the bottom up, the lower saddle-node bifurcation is (just barely) seen to spawn an unstable node and a saddle - i.e. it is now an SN2- bifurcation. The multipliers of the node coincide and subsequently become complex conjugates through the EE2- transition. Increasing the amplitude brings this unstable focus through the second new bifurcation, namely the T2 torus bifurcation. This occurs at $A \approx 0.845$. Above this point the scenario is qualitatively the same as the one

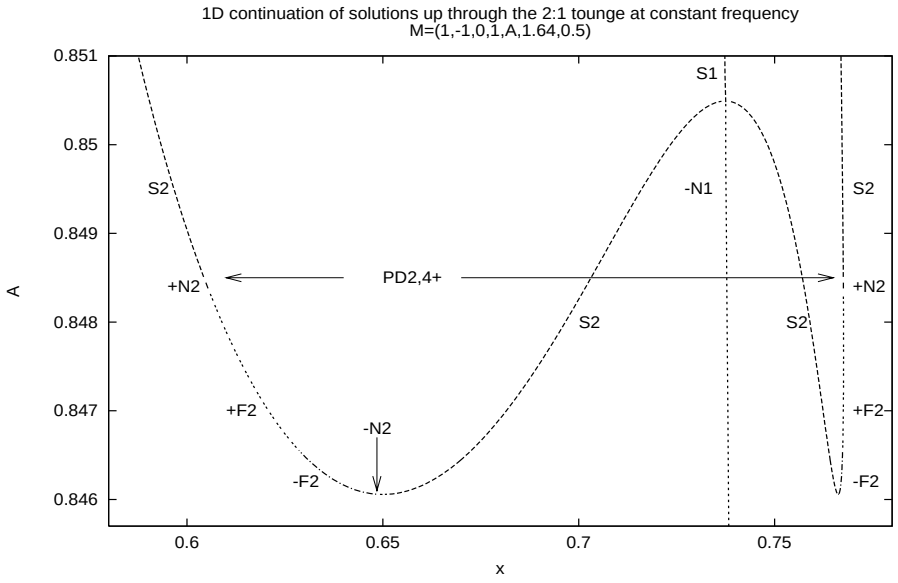

Figure 5.22 Co-existing period-one and two solutions in the 2:1 tongue at $\omega = 1.64$ - to the left of the Takens-Bogdanov point.

at $\omega = 0.7$.

The Degenerate Period-doubling and T-PD Connection Points

The SN2- curve connects to the bottom of the PD1,2 loop in an SN-PD (or DPD) point. At the left side of the PD1,2 loop is an important point marked T-PD/R2. Here two torus bifurcation curves connect to the loop of period-doubling bifurcations and furthermore, it is a R^2 point of the T1 curve with double multipliers in -1. It is necessarily so because of the simultaneous torus

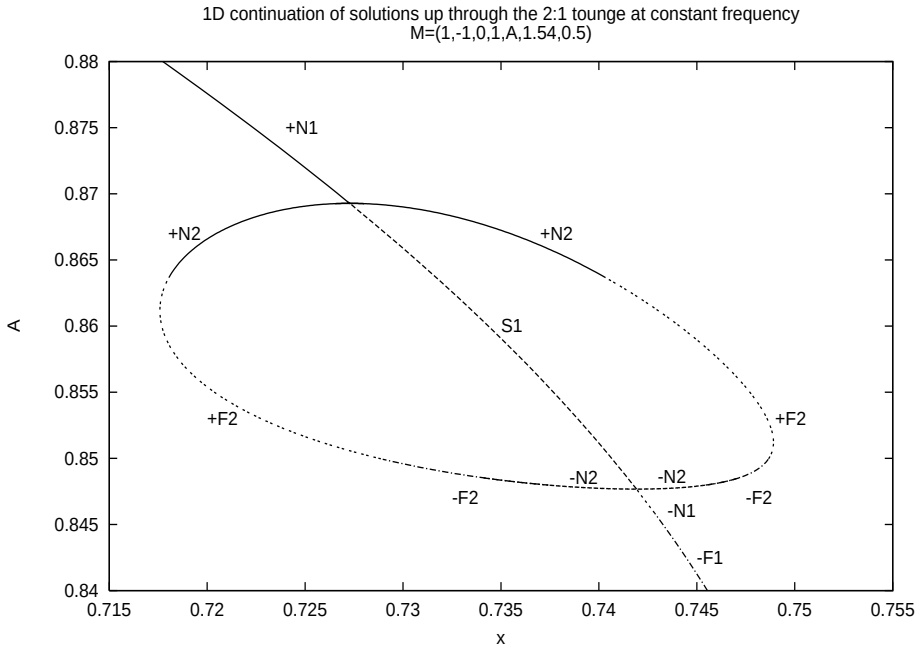

Figure 5.23 Co-existing period-one and two solutions in the 2:1 tongue at $\omega = 1.54$ - to the left of the degenerate period-doubling point and the cascade of period-doubling loops. The lower period-doubling is now subcritical.

bifurcation and period-doubling, which cause the multipliers of the period-one solution to be both complex conjugate and pass through -1 on the unit circle.
The period-one equal-eigenvalues curve is noted to change type while passing through it tangentially to the loop.
In Chapter 2 was illustrated how the period-doubling changes between super- and subcritical at the SN-PD and T-PD connection points. In accordance with this, the piece of the loop running between them is seen, in Fig. 5.20, to consists of subcritical period-doublings. This piece is now the lower boundary of the 2:1 entrainment region instead of the SN2- curve.
A full vertical scan through the loop at $\omega = 0.54$ is presented in Fig. 5.23. It passes through the 2:1 tongue between the T-PD and the DPD points. Thus, a period-one solution crosses both a subcritical and a supercritical period-doubling bifurcation point. The period-two solution no longer experiences a saddle-node bifurcation and is observed to undergo both an EE2+ and an EE2- transition. Between these transitions a T2 bifurcation occurs.

5.3.3 The Equal-Eigenvalues Curves

The EE1 Curves

The observations made with respect to the period-one equal-eigenvalues curves in the 1:1 tongue are in many ways similar to those made when examining the 2:1 tongue. This is not surprising, as the same 'rules' apply to the EE1 transitions in both cases.
There are two differences though; (i) at the 2:1 tongue the EE1 curves run through a T-PD point and not a TB point, and (ii) the EE1 curves lie outside the resonance tongue.
Both observations can be explained by the way in which the T1 curve connects to the PD1,2 loop. In Section 5.3.4 a scenario, in which the T1 curve crosses the SN2 curve and connects to the PD1,2 loop below the SN-PD point, will be discussed. Such a scenario would cause the EE1 curve to lie inside the tongue at least some of the way.

The EE2 Loops

Three closed loops of period-two equal-eigenvalues points have been observed in the 2:1 tongue and can be seen in Fig. 5.17. Two of these are located at the left side of the tongue, one inside the other. The outermost of these and the loop at the right side of the tongue are associated with torus bifurcations of period two solutions.
Inspection of Fig. 5.20 reveals how the outer loop runs through the T-PD and the TB codimension two points and changes type in both of these. The necessity of its presence and the change in type can be understood by arguments similar to those regarding the EE1 curves. However, a slightly different argument must be given for the presence of the innermost loop. Unlike the right side of the tongue, the left side has the above-mentioned cascade of period-doubling loops. These PD loops are enclosed by the EE2 rings. The extra EE2 curve is needed due to the PD2,4 loop. If the node-to-focus change caused by the outer EE2 transition is not 'reversed' the period two solution cannot period-double.

5.3.4 Possible Scenarios of the 2:q Tongues

Through investigations of the 2:1 tongue, under variation of both μ_0 and ϵ, certain features are consistently found: (i) At lower amplitudes the SN bifurcations of the tongue are SN2+ curves. (ii) At high amplitudes the upper part of the PD loop is supercritical, i.e. PD1,2+. (iii) The SN2 curves and the T1 curve connect to the PD loop in codimension two points.
Subject to these constraints, and the wish for the simplest possible bifurcation structure, three possible scenarios are found theoretically possible for the 2:q tongues. On each side of the tongue it is of importance whether the T-PD connection points are located below or above the DPD points. The possible tongue scenarios can either be symmetric or asymmetric depending on the loci of these codimension two connection points. A symmetric tongue has the same connection scenario on both sides while the asymmetric does not.

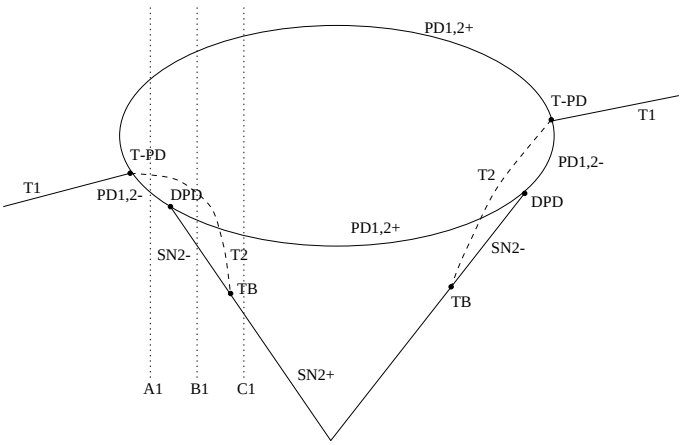

Figure 5.24 Bifurcation scenario 1. A symmetric tongue structure in which the DPD connections lie below the T-PD on both sides of the tongue. The scenario corresponds to the observed structure of the 2:1 Arnol'd tongue at $M = (1, -1, 0, 1, A, \omega, 0.5)$.

Scenario 1

Fig. 5.24 is a schematic representation of a symmetric scenario. The T-PD point is located above the DPD point on both sides of the tongue.
In accordance with the considerations made in Chapter 2, the SN curve below the PD+ loop is of the opposite sign, namely SN2-. As the lower part of the 2:1 tongue consists of SN2+ bifurcations, there must be a CD2 point marking a change from SN- to SN+ somewhere along the side. Furthermore, the -N2 solutions extend from the SN2- and the PD1,2- curve must change stability to +N2 solutions for consistence.
A simple way to solve the discrepancies is if a T2 curve extends from a TB point on the SN curve towards the PD loop, and connects in the already existing T-PD point. The codimension of the T-PD point is unaffected as the T1 and the T2 bifurcations involve two different solutions. Any other connection of the T2 to the PD$\pm$ curve would create a "new" codimension two point and destroy the organization of the $\pm$-shifts and thus change the

global scenario of the tongue. This could naturally be avoided if additional bifurcation curves where present but that would alter the simplicity of the tongue structure.

In Fig. 5.25 schematic bifurcation diagrams along the lines A1, B1 and C1 are presented. These are included, to help visualize the solutions passing through the bifurcation structure, but also to show that the organization of the tongue is consistent. In the figures EE transitions are included for completeness, but for simplicity they are not included in Fig. 5.24.
The bifurcation structure has been found in the present study, and also in many other systems of forced oscillators e.g. [Vance and Ross, 1989] and [Pavlou and Kevrekidis, 1992].

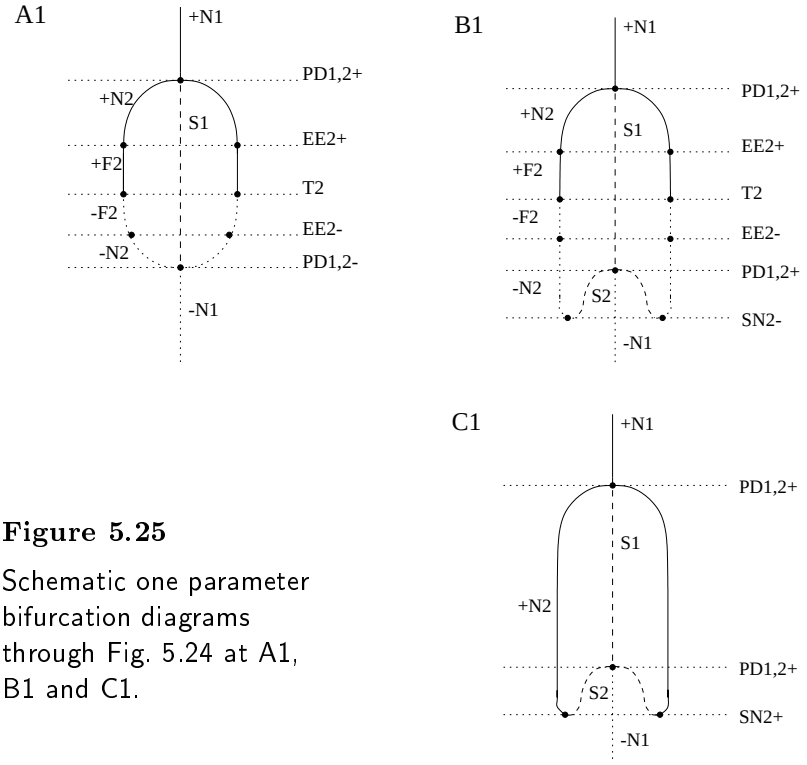

Figure 5.25

Schematic one parameter bifurcation diagrams through Fig. 5.24 at A1, B1 and C1.

The scan at A1 passes through the period-doubling loop between the T-PD and the DPD points. The period-1 solution experiences both a sub- and a supercritical PD, and the period-2 solution passes through a T2 bifurcation for the structure to be consistent.
B1 is between the DPD and the TB points. Both PD bifurcations are now supercritical and the period-two solution turns in an SN2- bifurcation.
C1 passes through the 2:1 tongue to the right of the TB point. The SN bifurcation has changed to an SN2+ and the T2 bifurcation no longer exists.

Scenario 2

The second consistent bifurcation scenario of the 2:1 tongue is also symmetric but with DPD points connecting above the T-PD points. The scenario is depicted in Fig. 5.26. Note that the overall characteristics of the tongue are unchanged from the first scenario. Supercritical bifurcations still dominate the PD loop, and the lower SN bifurcations are SN+ curves.
The structure does not involve additional bifurcation curves. In fact, the

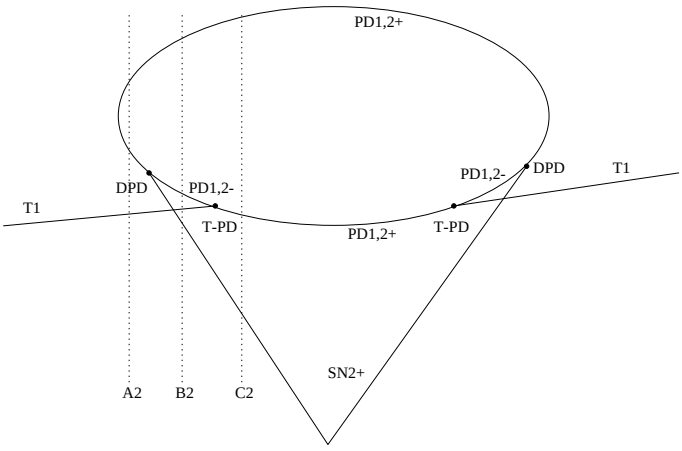

Figure 5.26 Bifurcation scenario 2 - a symmetric tongue structure in which the DPD connections occurs above the T-PD points on the period-doubling loop.

presence of a T2 bifurcation running between the PD loop and the SN curve would only destroy the already consistent organization of the tongue.

In Fig. 5.27 scans at A2 and B2 are illustrated. The scan at C2 passes through a bifurcation scenario similar to that at C1 in Fig. 5.25.
Scanning with increasing amplitude, a period-1 solution in figure A2 experiences a torus bifurcation and then passes through two supercritical period-doubling bifurcations. Moving from the left side of the DPD point to the right, the scan at B2 passes through both a sub- and a supercritical bifurcations. Period-2 solutions extend down from these period-doubling bifurcations and terminate at the SN2+ bifurcation curve.

In the present analysis this structure has not been observed, nor has it appeared in any work known to us.

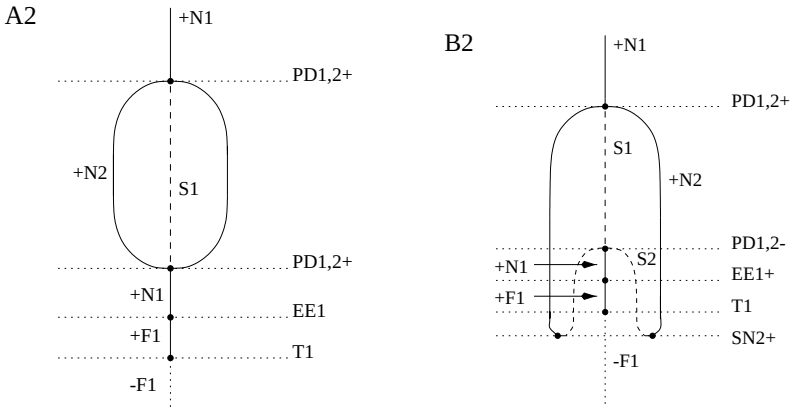

Figure 5.27 Illustrations of scans through Fig. 5.26 at A2 and B2.

Scenario 3

The last scenario considered to be possible is one in which the tongue is asymmetric: On one side the DPD lies below the T-PD point and on the other it lies above. Corresponding to Fig. 5.24, a T2 bifurcation line must run from a TB point on the SN curve to the T-PD point on the PD loop,

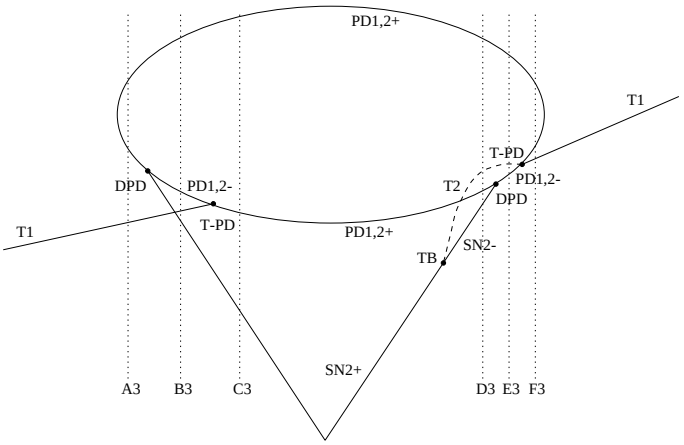

Figure 5.28 Bifurcation scenario 3. The bifurcation structure of the tongue is asymmetrical as the DPD connection lies above the T-PD point in the left side and beneath it in the right side. The lines passing through the tongue correspond to scans presented in relation to Fig. 5.24 and Fig. 5.26: A3=A2, B3=B2, C3=C2=C1, D3=B1, E3=A1, and F3=A3=A2.

when the DPD is below the T-PD point. Similar to Fig. 5.26, no bifurcations other than T1 and SN2+ are involved when the DPD lies above the T-PD. The scenario is portrayed in Fig. 5.28 and the scans through the structure correspond to the ones presented in Fig. 5.25 and Fig. 5.27. The asymmetric structure is observed in the present system. For the parameter values $M = (0.05, -1, 0, 1, A, \omega, 0.5)$ the 2:1 tongue is constructed in great detail and shown in Fig. 5.29. A zoom on the upper right connections of the saddle and the torus to the period-doubling loop is also included.

The change between scenarios 1 and 2 was caused by variation of the work-point with the strength of the coupling held constant. If this transition is to occur smoothly a singular point, at which the T-PD and the DPD points coincide, will exist in the limit between the scenarios. Such a point can be considered a codimension three point in which a T2 bifurcation is born/destroyed.

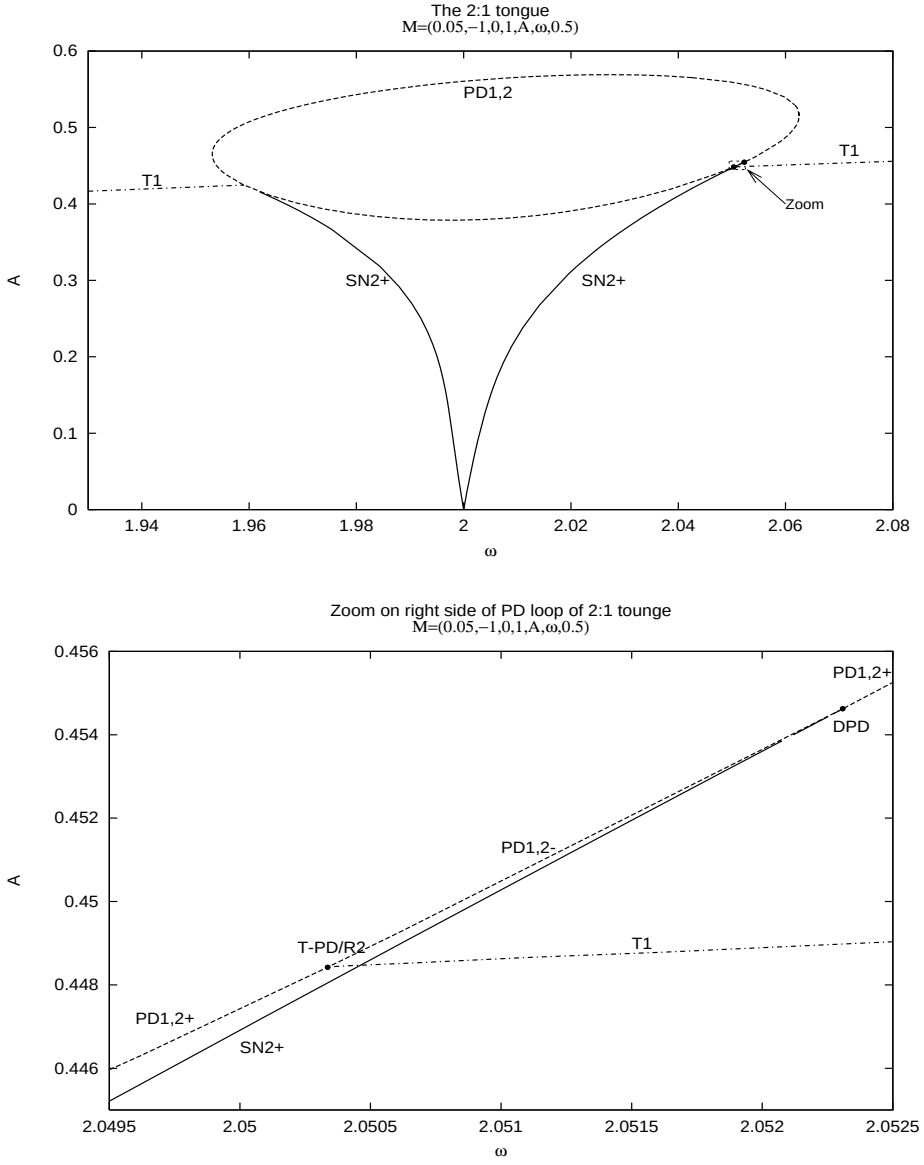

Figure 5.29 The 2:1 tongue. Note that the workpoint, relative to the point at which Fig. 3.3 was obtained, has moved closer to the Hopf bifurcation of the autonomous system. The overall structure corresponds to the 3rd scenario presented in Fig. 5.28 with the DPD point below the T-PD point on the left side of the tongue and above on the right side.

5.3.5 The 2:3 Tongue

The lesser 2:q tongues are of a structure similar to that of the 2:1 tongue. To exemplify this, the 2:3 tongue is presented in Fig. 5.30.

In addition to the outer bounding curves of the 2:3 resonance region, the figure also includes a zoom on the lower left part of the PD1,2 loop. Once again the T1 curve is observed to connect to the PD curve in a T-PD point. None of the codimension two points are marked in the figure as they are not determined with high accuracy. The structure of the 2:3 tongue is, however, found to correspond to the first scenario presented in Section 5.3.4. Inside the PD1,2 loop a period-doubling cascade leading to chaos has been located. It is interesting to note that the lower bound of the loops is also at an amplitude of approximately one, which corresponds to the forcing just touching the Hopf bifurcation of the unforced system. The loops are densely "packed" and this area of the parameter plane is rich on overlap of different entrainment regions. The 4:5 resonance tongue has been included, in the zoom of the 2:3 tongue, illustrating such an overlap. Note that the two tongues are of similar shape, but as is shown later, connect differently on the T1 curve.

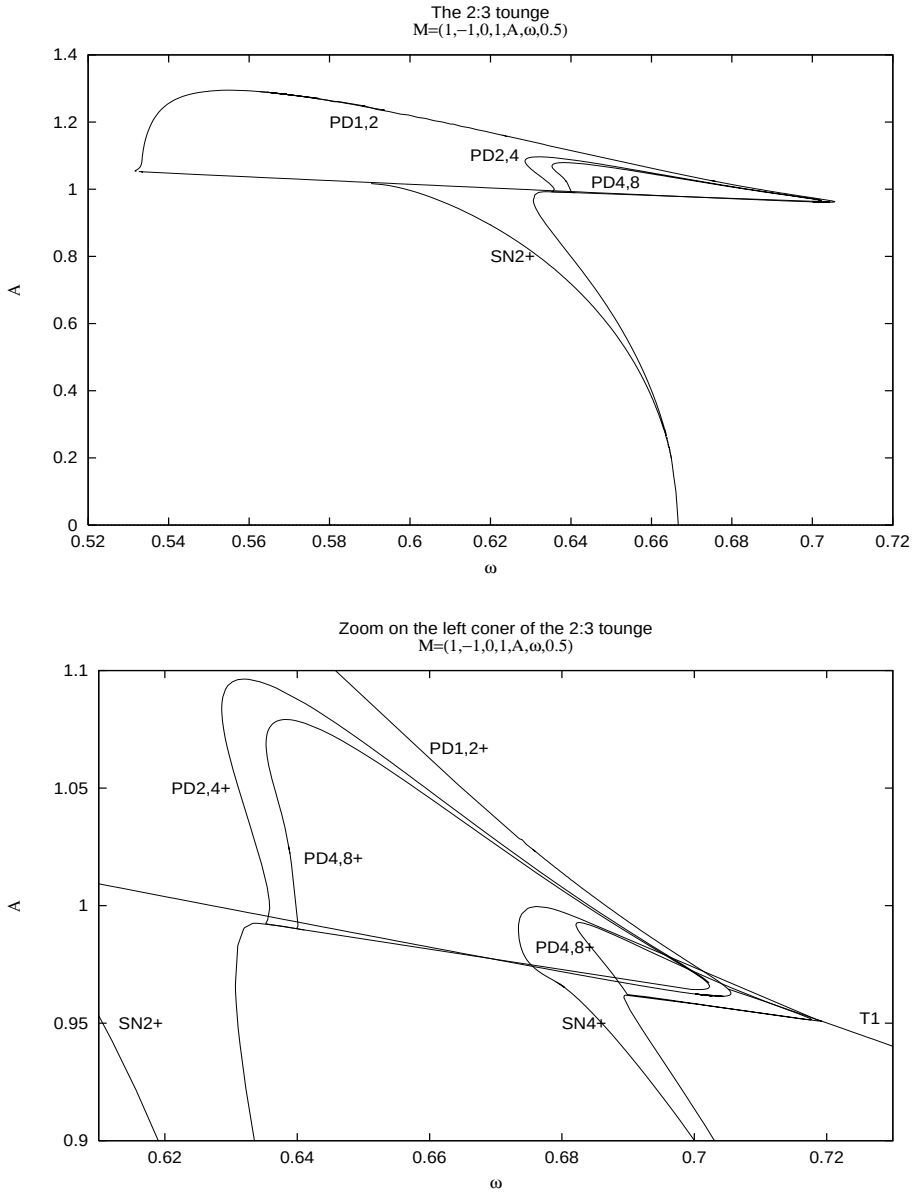

Figure 5.30 The 2:3 tongue. Notice the period-doubling loops inside the PD1,2 loop. In the magnification on the period-doubling loops the 4:5 tongue and the T1 bifurcation curve are included

The complex bifurcation structure in the neighbourhood of the 2:3 tongue is illustrated by a Brute Force scan passing up through the tongue at $\omega = 0.64$ in an amplitude interval from 0.5 to 1.1. In the diagram the 2:3 synchronization is not reached through a PD1,2 bifurcation. A series of catastrophic bifurcations, dominated by saddle node bifurcations, pass through different modes of synchronization and chaos. The 2:3 mode is finally reached through a backwards period-doubling cascade bringing the system out of the chaotic regions.

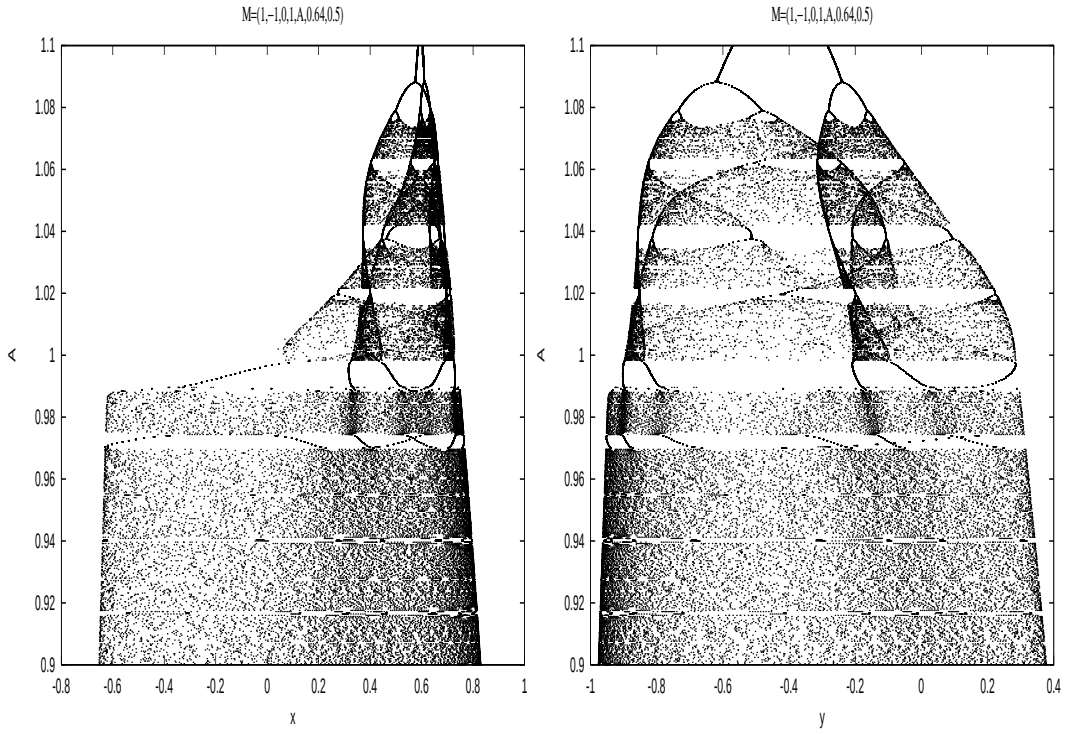

Figure 5.31 A Brute Force study of the 2:3 resonance region. The forcing amplitude is varied from 0.9 up to 1.1 at constant frequency.

An analysis of the Lyapunov exponents of the corresponding solutions reveals

that chaos is first introduced as an 5:q entrainment region ends in a saddle node bifurcation. In Fig. 5.32 the Lyapunov exponents are presented for the interval leading out of this synchronized state into chaos. The first positive Lyapunov exponent has been found at an amplitude just below 1.

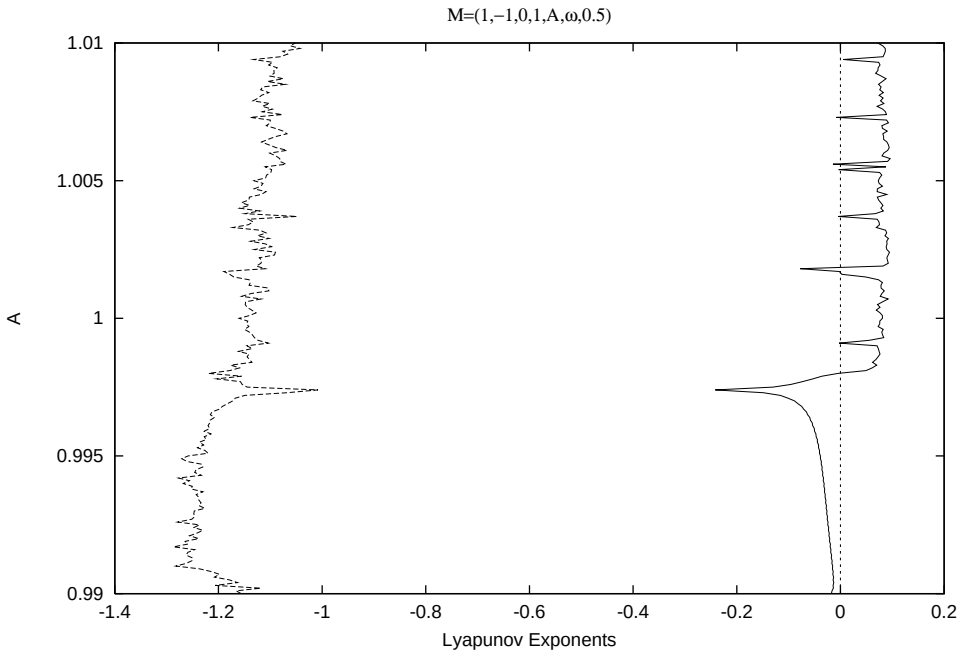

Figure 5.32 A study of the Lyapunov exponents for the corresponding solutions observed in the Brute Force examinations in Fig. 5.31

5.3.6 Summary

- The numerically constructed 2:1 and 2:3 tongues were presented. At lower amplitudes the Arnol'd tongues were cone shaped regions bounded by SN2 bifurcations. The SN2 curves connected to loops of PD1,2 bifurcations at higher amplitudes. Both of the period-two entrainment regions were closed by these loops.

- Codimension two points, related to the 2:1 tongue, were determined with high accuracy and the period-two solutions examined in a neighbourhood of these. Two resonant Hopf bifurcation points were associated with each of the entrainment regions. These coincided with T-PD points on both sides of the tongues.

- Three scenarios, in which the connections of codimension one curves differed, were postulated as possible in the 2:q tongues. Two of the scenarios have been found in the present study. If the transitions between the scenarios are to occur smoothly, a second order resonance point of codimension three must occur as a degenerate period-doubling point coincides with both a period-one and two torus bifurcation.

- Chaos was observed inside a cascade of PD loops in both tongues. This was determined by means of the Brute Force method and calculation of Lyapunov exponents. The analysis of a route to chaos inside the 2:3 tongue was presented.

- In addition to period-one equal-eigenvalues curves, which formed a tongue-like structure on the outside of the 2:1 resonance region, three loops of period-two equal-eigenvalues curves were found inside the boundaries of the region. Two of these were associated with torus bifurcations of period two solutions and the third was a necessary consequence of a PD2,4 loop located on the left side of the tongue.

5.4 The 3:1 and 3:2 Tongues

Originating at $\omega = 3$ is the third strong resonance region, the 3:1 tongue. This is traced and examined as a representative of the qualitatively similar 3:q entrainment regions. The 3:2 tongue is also discussed albeit in less detail. Fig. 5.33 shows the 3:1 tongue relative to the T1 bifurcation line which extends from the rightmost T-PD point of the 2:1 tongue. It is seen to be different from the previously considered 1:q and 2:q regions both in shape and relation to the T1 line. The 3:1 region is bounded solely by SN3+ bifurcation curves and has no EE1 curves associated with it. As expected, the tongue widens as the amplitude is increased but as the T1 line is approached, it gradually narrows in and closes on itself.

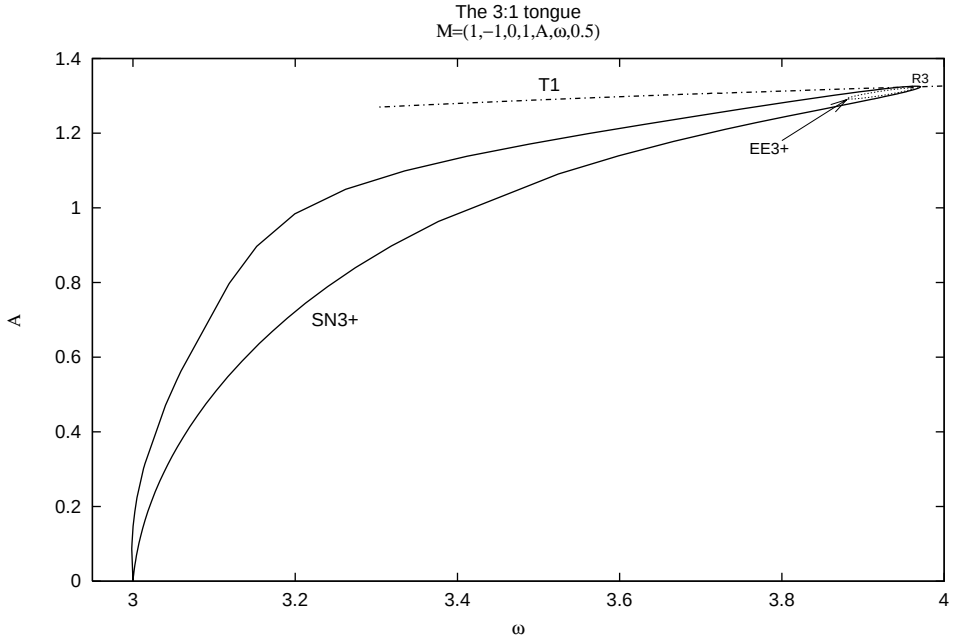

Figure 5.33 The 3:1 tongue.

The uppermost part of the tongue will be the focus of attention in the following as this is where the strong resonant, R^3, Hopf bifurcation is found along with period-three equal-eigenvalues transitions and global bifurcation curves.

5.4.1 The Top of the 3:1 Tongue

Details of the closing of the 3:1 tongue are presented in Fig. 5.34. The first frame reveals how the tongue closes smoothly in a loop above the curve of period-one torus bifurcations. The top encloses a single R^3 resonance point which, unlike the scenarios found in the 1:q and 2:q tongues, does not coincide with the tongue boundary.
In the overlap-region period-three saddles and nodes coexist with stable period-one focus solutions. Below the T1 curve, and the associated resonance point, lies a closed loop of EE3+ transition points. Contrary to the EE2 loops, this closed curve does not pass through any codimension two points, and does not change type correspondingly.
In addition to the resonance point, seven locations have been marked by bullets in the second subfigure of Fig. 5.34. These mark parameter values at which the solutions will be examined in depth. Stroboscopic phase portraits reveal the presence of homoclinic bifurcations in this tongue also. We have made observations regarding the pairing of saddle and node solutions which will be discussed and explained on the basis of the global bifurcations in the tongue.

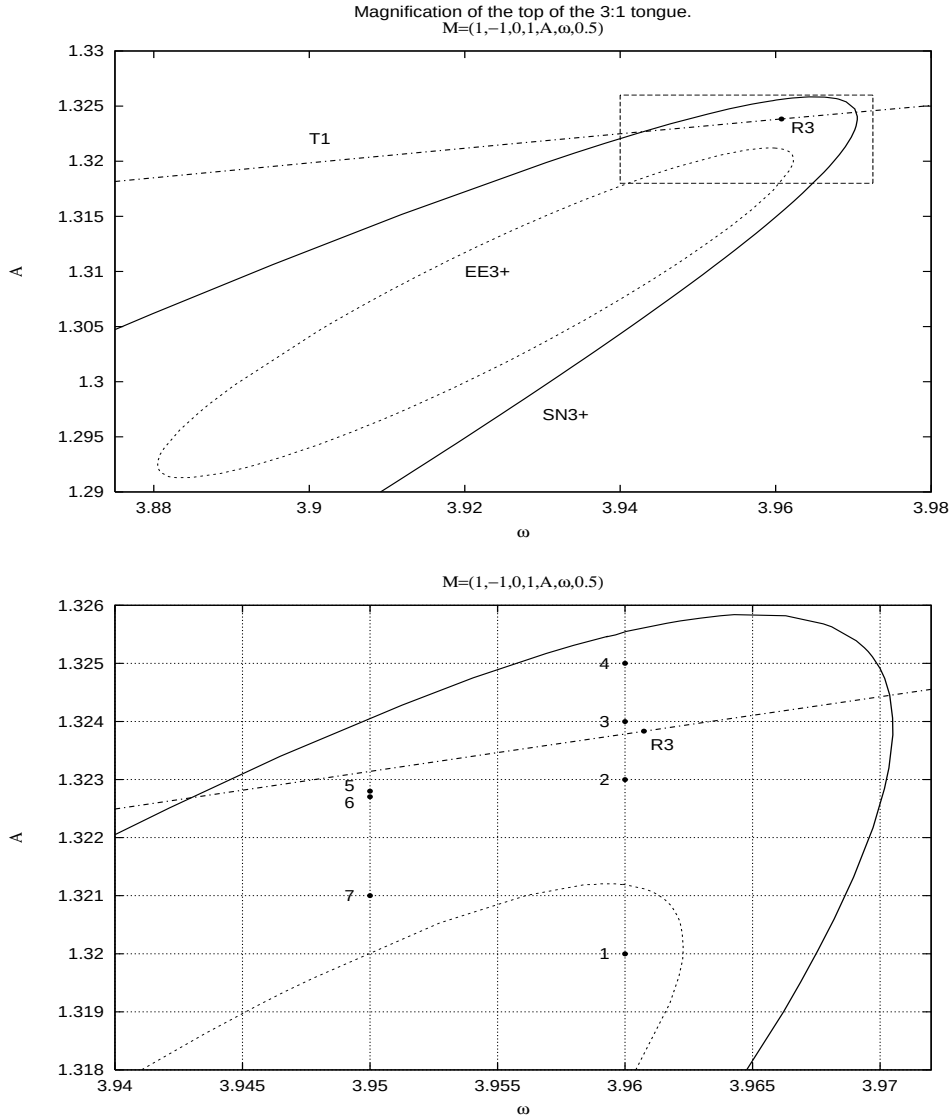

Figure 5.34 Enlargements of the top of the 3:1 tongue. The top subfigure shows the closed loop of EE3+ points relative to the T1 curve and the resonant Hopf bifurcation. A further magnification corresponding to the dashed box is presented in the bottom figure. The numbered bullets mark locations at which stroboscopic phase portraits are analyzed.

EE3+

Saddle-Node Pairing and the R^3 Resonance Point.

Fig. 5.35 through Fig. 5.37 are one-dimensional bifurcation diagrams across the tongue. The labels (1) - (4) and (R3), in the upper left corner, correspond to the numbered bullets in Fig. 5.34, hence, most of the diagrams are scans along grid-lines in the figure. To allow direct comparison, the plots are all shown in the same ω-x range.
Beginning at (1), the solutions in Fig. 5.35 are seen to be born in saddle-stable-node pairs on the left side of the tongue. This scan passes through the EE3+ loop. In agreement with this, the stable nodes become focus solutions in the range of frequencies between 3.95 and 3.962 approximately. At the other side of the tongue the solutions collide in a different configuration of saddle and node pairs, the solutions forming a single closed curve in the bifurcation diagram. Fig. 5.35, which is a scan at a higher amplitude, is qualitatively similar. The inset is a magnification of the details of the crossings.

Further increase of the amplitude causes a change in the bifurcation structure. At amplitudes corresponding to the points (3) and (4) above the T1 bifurcation curve, the solutions no longer form a single closed curve, but three separate loops. This is seen in Fig. 5.36. In the $\omega - x$ projection there is no longer a crossing of the saddle curves, but more importantly the S3,+N3 pairing is now the same on both sides of the tongue. The change is abrupt and it turns out to be the location of the resonance point that marks the transition amplitude.

Fig. 5.37 is a scan through the R^3 resonance. From the figure and the inset, the saddle solutions are seen to coincide and effectively become a period-one solution in this point. A plot involving the y-variable reveals the same crossing. This ensures that it is not merely an artifact of the projection as it is when the saddle solutions cross in the other bifurcation diagrams.
Based on the definition of the resonant Hopf bifurcation, and associated comments given in Chapter 2, this coalescence of saddles could have been anticipated as the R^3 point is located inside the entrainment region and not at a connection point of codimension one curves.

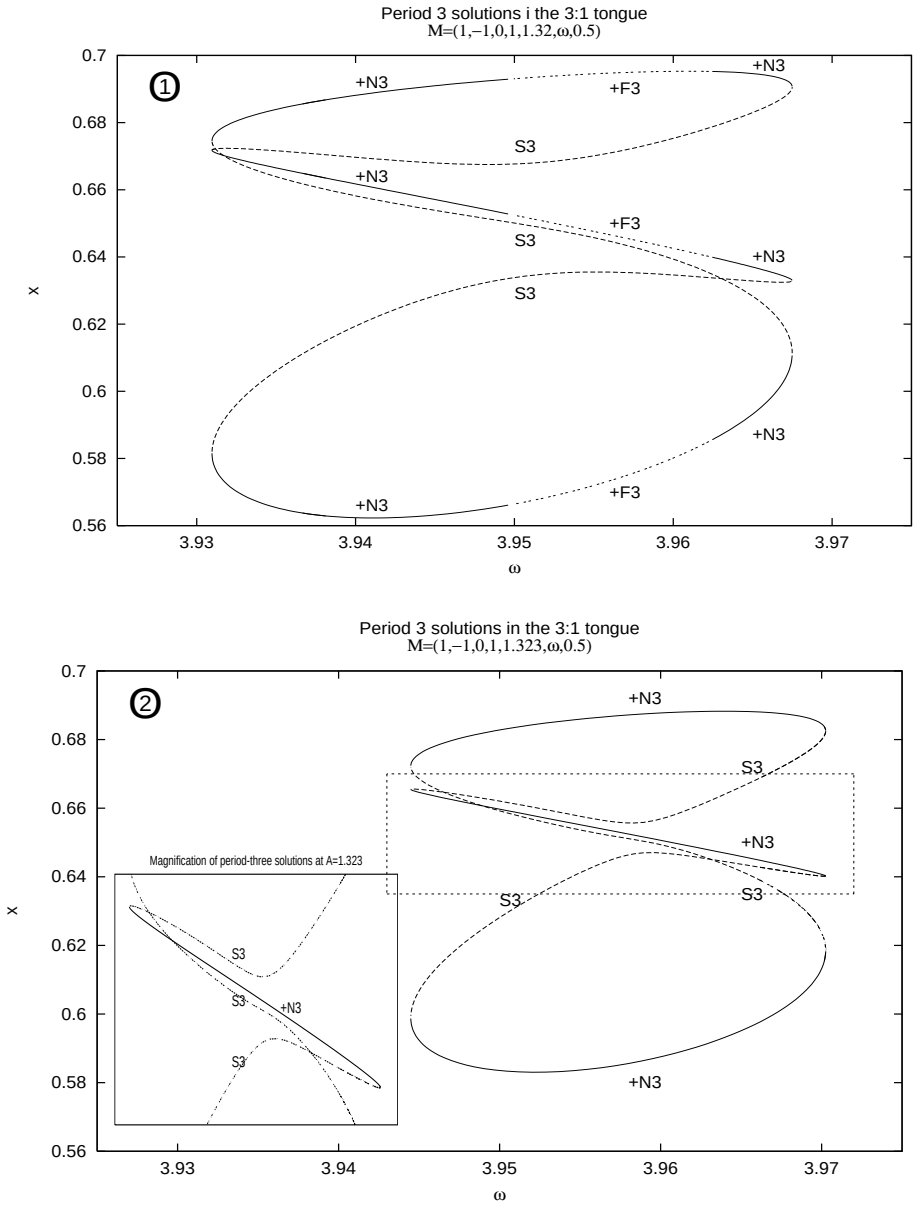

Figure 5.35 One-parameter bifurcation diagrams illustrating the scenario where the saddle-node pairing changes as the tongue is crossed.

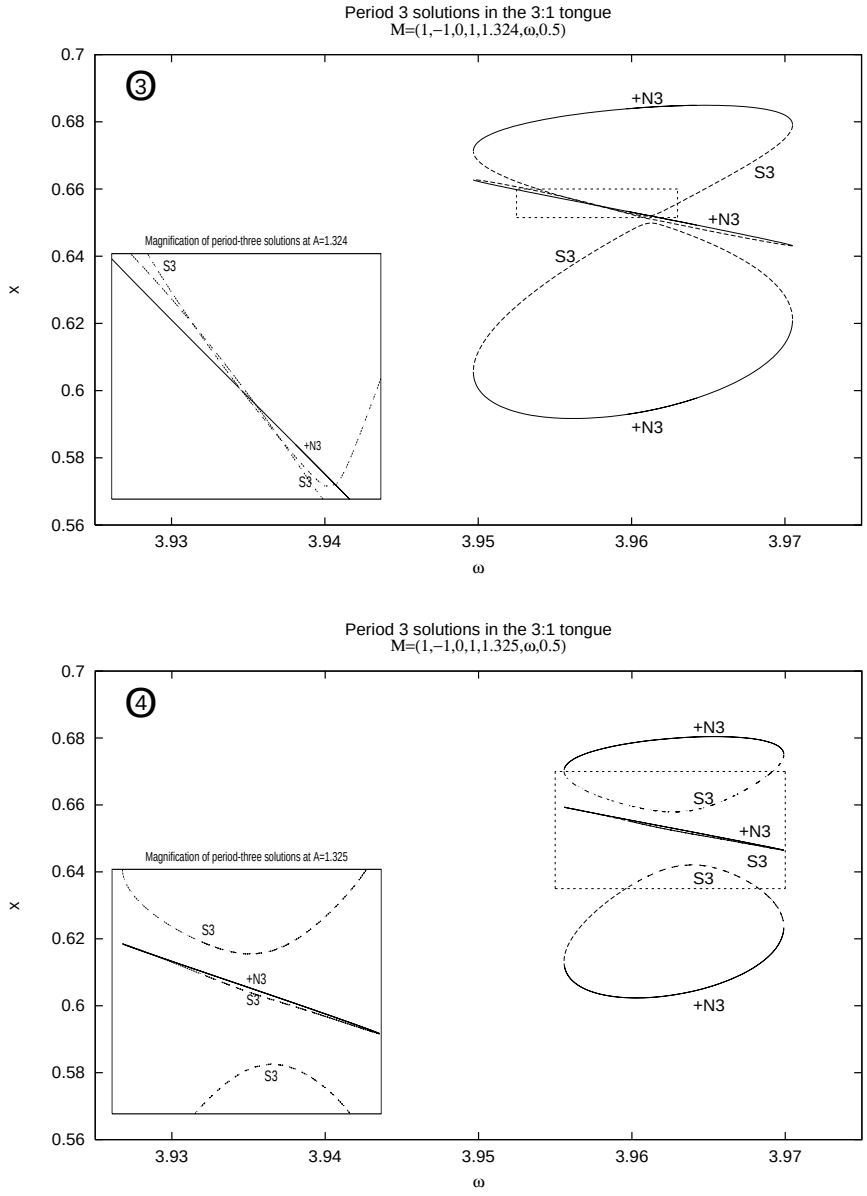

Figure 5.36 One-parameter bifurcation diagrams illustrating the scenario where the saddle-node pairing does not change as the tongue is crossed.

Besides the apparent symmetry, there is nothing in these observations which explains why the resonance point causes a change in saddle-node pairing. The answer to this question is found when considering the global bifurcations inside the entrainment region.

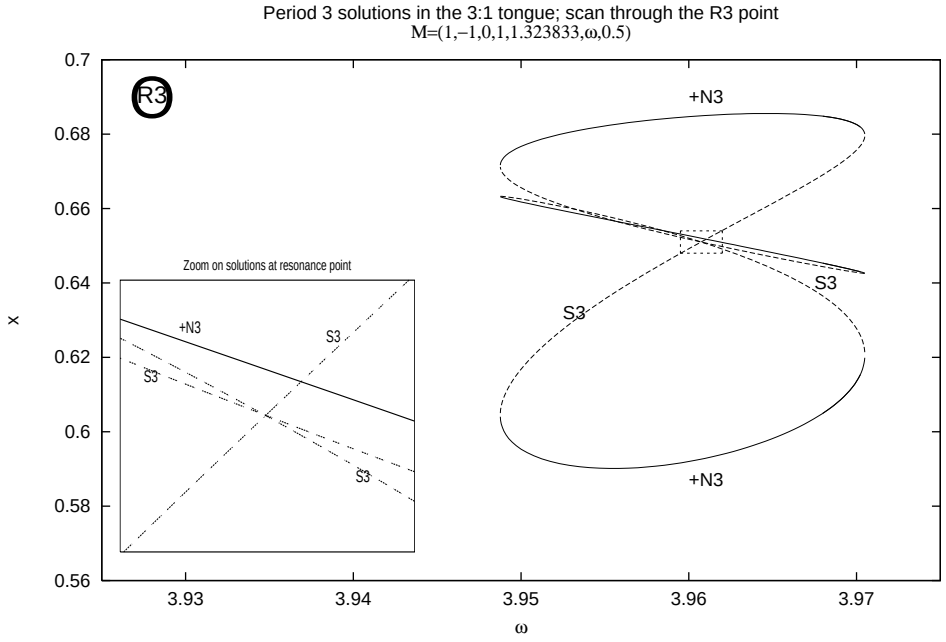

Figure 5.37 One-parameter bifurcation diagram through the R^3 resonance point. At this point the saddle curves coincide and effectively become a period one solution. The amplitude at which this scan is obtained marks the transition between the two different types of saddle-node pairing observed in Fig. 5.35 and Fig. 5.36.

Global Bifurcations

Analyses of the phase plane dynamics at points (1) through (7) have been carried out by determination of points on the invariant manifolds of the rel-

evant fixed points. These are presented in the following and establish the presence of homoclinic bifurcations qualitatively similar to the ones in the lower order resonance tongues.

The first four phase portraits in Fig. 5.38 to Fig. 5.41 paint a picture of the dynamics around the solutions seen in the previous bifurcation diagrams. At point (1) the solutions lie on a deformed invariant circle with cusps at the stable solutions. Enclosed by this is the unstable period-one focus. As the amplitude is increased, the saddle points approaches each other and the -F1 solution. Point (2) lies outside the EE3+ loop and thus the +F3 solutions of Fig. 5.38 have been replaced by +N3 solutions in Fig. 5.39. The strong invariant manifolds of the nodes are included in the figures. The lack of smoothness and cusp formation on the invariant circle indicate a previous heteroclinic tangle of the outset of the saddles and strong stable inset of the nodes. This is a scenario analogue to the one observed in the 1:1 tongue.

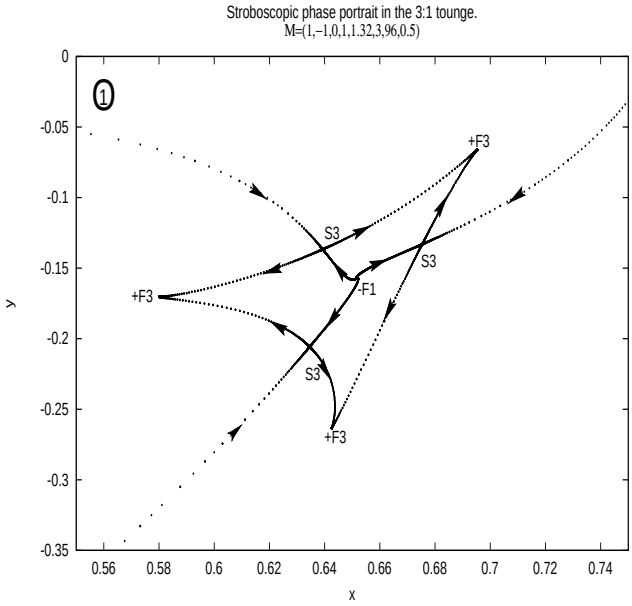

Figure 5.38

Stroboscopic phase portrait at point (1) in Fig. 5.34. The invariant circle is not smooth and has developed cusps at the stable period-three solutions. This is a result of a heteroclinic tangle occurring at lower amplitudes.

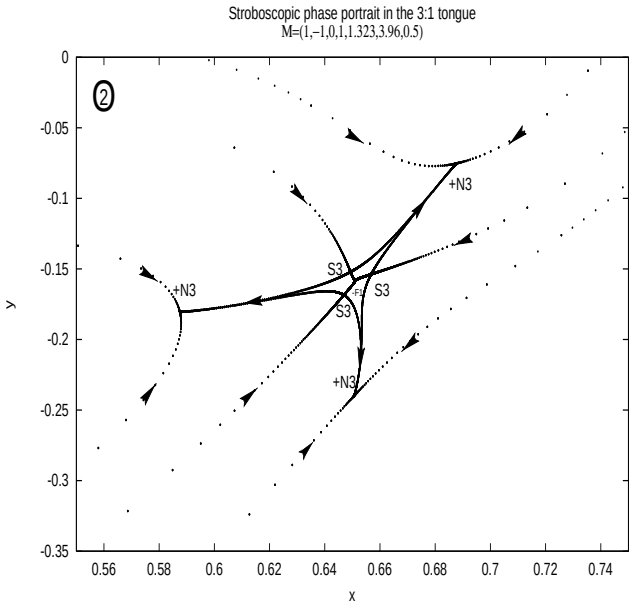

Figure 5.39

Stroboscopic phase portrait at point (2) in Fig. 5.34. The manifolds still form a closed curve, but the stable period-three solutions are now nodes.

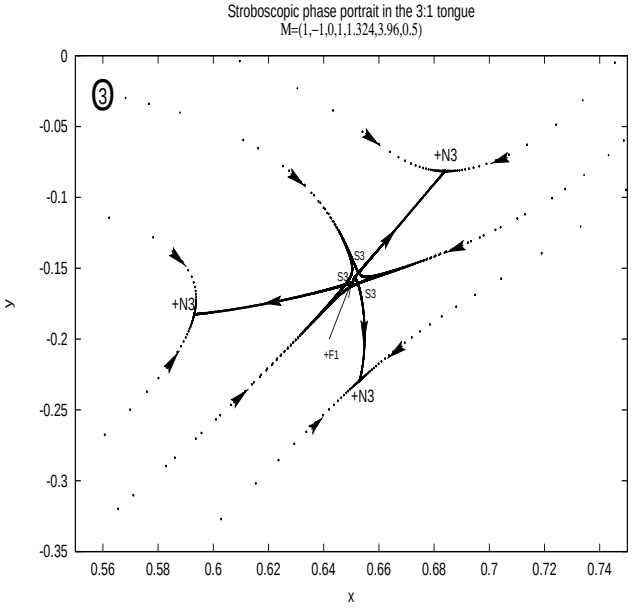

Figure 5.40

Stroboscopic phase portrait at point (3) in Fig. 5.34. As a result of a homoclinic bifurcation, the manifolds no longer form an invariant circle. The central period-one solution has become stable through a torus bifurcation.

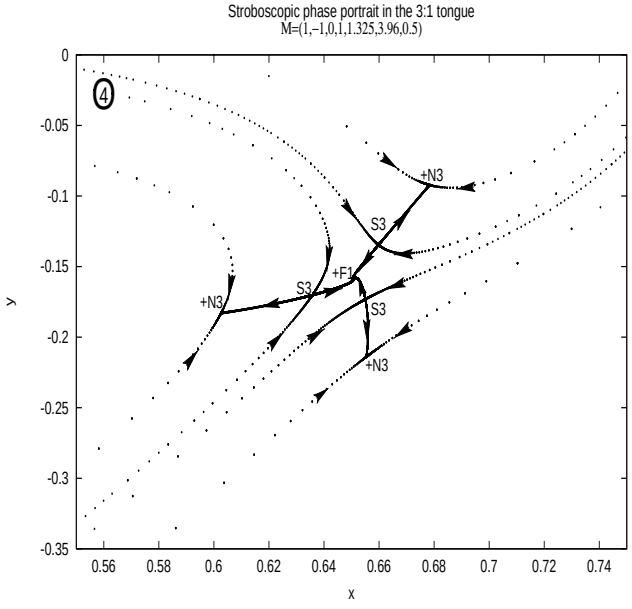

Figure 5.41

Stroboscopic phase portrait at point (4) in Fig. 5.34. This scenario is qualitatively similar to that of Fig. 5.40 but closer to the tongue boundary, consequently the saddle solutions have moved towards the nodes.

Somewhere between the points (2) and (3) a homoclinic bifurcation occurs. Above the T1 line the central period-one focus has become stable, and the invariant circle has been destroyed. In Fig. 5.40 the saddle solutions lie close to the +F1 point; this is a reflection of their collapse onto this solution in the nearby R^3 point. Increasing the amplitude towards (4) causes the saddles to move further away from the focus and closer to the nodes. Fig. 5.41 gives a clearer picture of the dynamics which are qualitatively similar at (3). A more accurate location of the global bifurcation is found at a frequency of 3.95. At this frequency the phase portraits have been obtained at amplitudes corresponding to the points (5) - (7), and are portrayed in Fig. 5.42, Fig. 5.43, and Fig. 5.44. The homoclinic bifurcation takes place between (5) and (6) i.e. at an amplitude in the range from 1.3228 to 1.322705. In Fig. 5.42 a quasiperiodic attractor coexists with the -F1, S3 and +N3 solutions, the unstable manifolds of the saddle solutions winding around it. Decreasing the amplitude causes the stable inset of the saddles to move closer to the outset and finally the homoclinic crossing occurs. The quasiperiodic attractor is destroyed and replaced by a closed invariant circle on which the period-three solutions lie. In Fig. 5.43 it is difficult to see this closure of the manifolds, but the destruction of the quasiperiodic attractor is clearly indicated by the stable manifolds of the saddles, which now spiral out from the enclosed focus. Fig. 5.44, which is a phase portrait obtained at point (7), has been included to give a better illustration of the distorted invariant circle formed in this process.

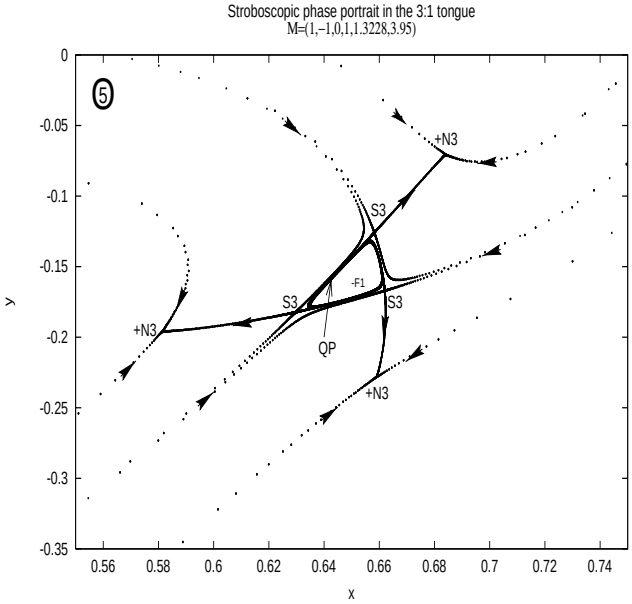

Figure 5.42

Stroboscopic phase portrait at point (5) in Fig. 5.34. The scenario is close to (above) a homoclinic crossing. A quasiperiodic attractor encloses the unstable period-one focus.

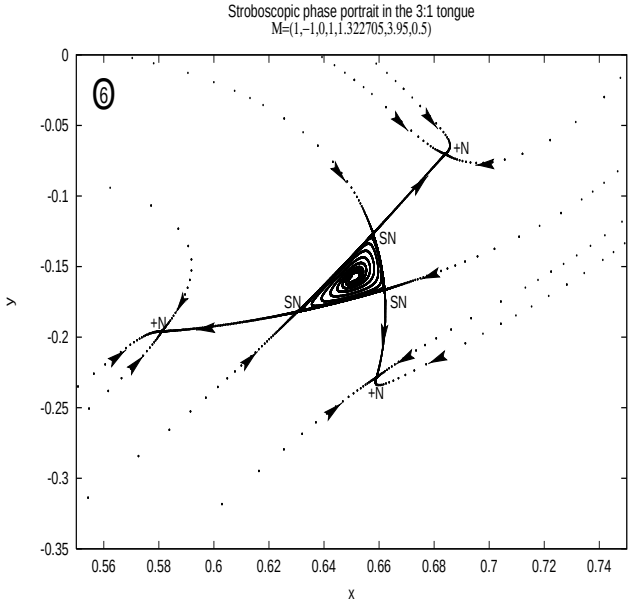

Figure 5.43

Stroboscopic phase portrait at point (6) in Fig. 5.34. Decreasing the amplitude has destroyed the quasiperiodic attractor of Fig. 5.42. The manifolds form a highly distorted invariant circle.

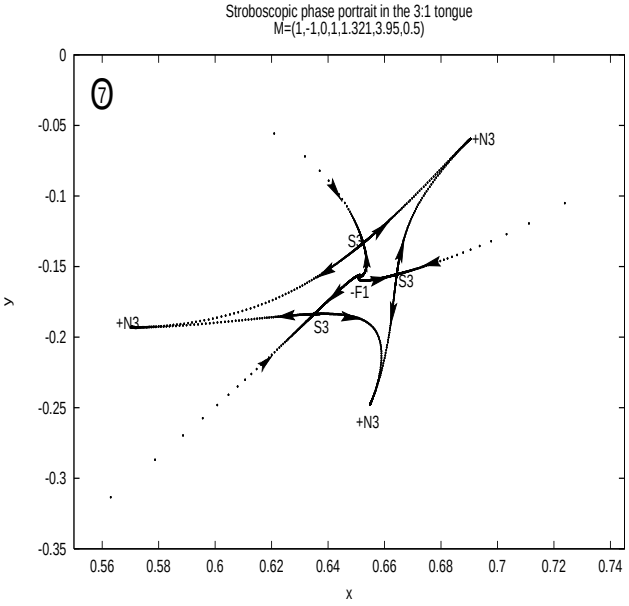

Figure 5.44

Stroboscopic phase portrait at point (7) in Fig. 5.34. The portrait is a clearer illustration of the manifold connections of Fig. 5.43.

Curves of global bifurcations are not followed in this thesis. The results presented in the previous are, however, in good agreement with observations made by [Pavlou and Kevrekidis, 1992] and [Vance and Ross, 1989] who have traced such bifurcations. The curves are found to connect to the resonant Hopf bifurcation point and the sides of the tongue in a fashion somewhat similar to the scenario in the 1:1 and 2:1 tongues. Fig. 5.45 is a schematic drawing of the bifurcation sets at the tongue top. This is not only in accord with the phase portraits we have obtained but also with the bifurcation diagrams of Fig. 5.35, Fig. 5.36, and Fig. 5.37.
The numbered bullets indicate some of the phase portraits, (1) through (7), that are representative of the different regions.

Returning now to the issue of saddle-node pairing, three scans through the schematic tongue are considered. These are labeled A, B, and C in Fig. 5.45. Below the G-SN connection the saddle-node solutions are born on an invariant circle. At low amplitudes this is smooth like it was observed in the 1:1 and 2:1 tongues. Above the connection point the manifolds of the emerging

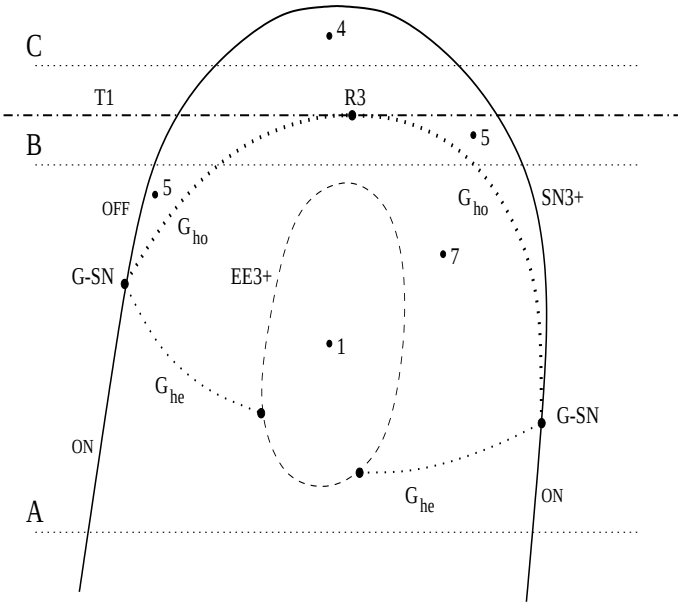

Figure 5.45 Schematic illustration of 3:1 homo- and heteroclinic transitions.

solutions do not form an invariant circle. As in Fig. 5.16 this is indicated by 'ON' and 'OFF' in the figure.

A bifurcation diagram obtained through a region corresponding to A will be of the same type as found in Fig. 5.35. The solutions appear in pairs on an invariant circle, move around it, and collide with the solutions of a neighbouring pair at the other side of the tongue.

At C the manifolds do not form an invariant circle on either side of the tongue, and thus the stable manifolds of the saddle points prevent any contact with the other pairs. When the tongue is crossed here, it is only possible for the solutions to collide with their initial partner. This results in a diagram as seen in Fig. 5.36.

Despite the fact that the solutions do not lie on an invariant circle at either tongue boundary, traversing the tongue at an amplitude between the G-SN and R^3 points (e.g. at B) yields a closed loop bifurcation diagram similar to

the one obtained at A. What might appear as an inconsistency is explained by the crossing of the global bifurcation curve. Even if there is only one possibility of saddle-node pairing on both sides, the homoclinic tangle provides the breaking of the pairs necessary for the explanation of the observed bifurcation diagrams of Fig. 5.35. This can be visualized by comparison of Fig. 5.42 and Fig. 5.44.
It should be noted that it is sufficient to cross only one of the G_{he} lines to achieve the change in pairing.

Consequently, R^3 is the point where the one-dimensional bifurcation diagrams are cut because it marks the upper bound on the global bifurcation curves. Above this the saddle-node pairs are always separated by the stable manifolds of the saddle solutions.

The lines representing heteroclinic transitions have been connected to the EE3+ loop, as this is the scenario observed by [Pavlou and Kevrekidis, 1992] and [Vance and Ross, 1989]. One could, however, imagine a single G_{he} curve running between the G-SN points below the EE3+ loop. This would not violate any of the principal aspects of the scenario.

5.4.2 The 3:2 Tongue

Between the 1:1 and 2:1 tongues lies the 3:2 tongue. The top of the tongue has another shape than that of the 3:1 region, but it also closes smoothly around an R^3 resonance point on the T1 curve. Fig. 5.46 shows the tongue along with this curve. It extends above the curve of Hopf bifurcations but unlike the 3:1 tongue, it has a beak-like structure pointing towards the 1:1 tongue. It is near the tip of this protrusion the resonance point is found. Inside the entrainment region, the T1 curve ends in an R^2 point where it

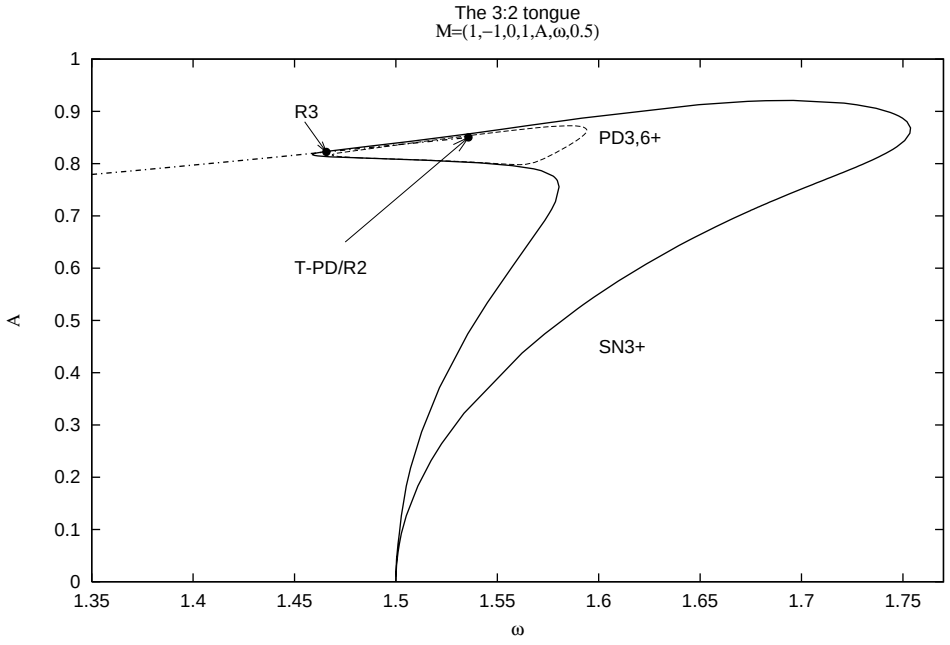

Figure 5.46 The 3:2 tongue closes smoothly over the T1 curve corresponding to the behavior of the 3:1 tongue. The associated R3 point lies just inside the tongue and not on the border. The T1 curve terminates in an R2/T-PD point. The tongue encloses a supercritical period-doubling loop marked PD3,6+.

connects to the 2:1 tongue. A significant overlap of the two tongues is thus observed in this area, which can also be seen in the excitation diagram of Fig. 5.1. An enlargement of the bifurcation set in the overlap region is presented in Fig. 5.47.

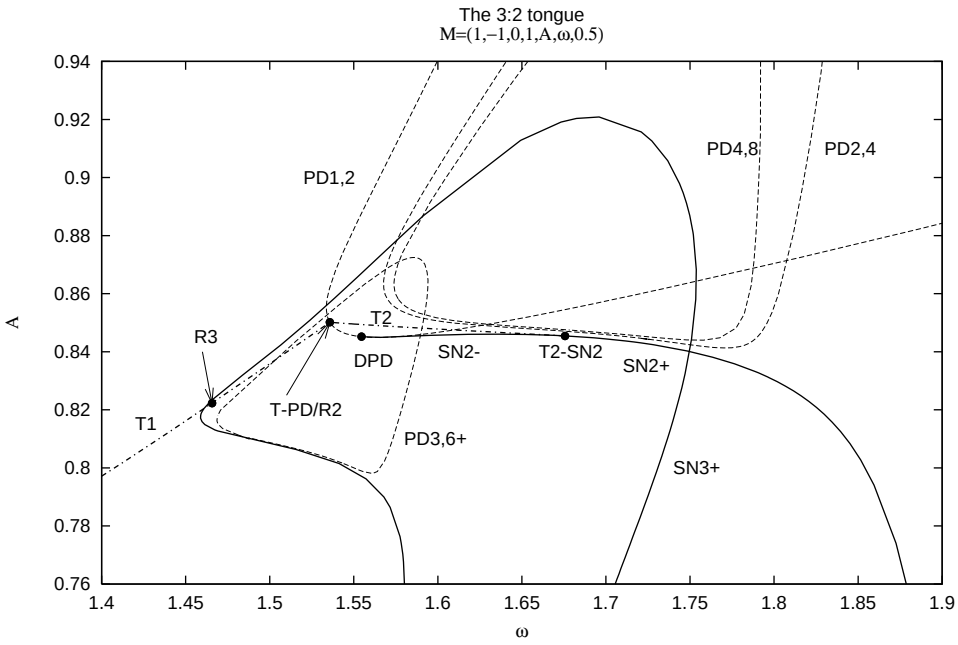

Figure 5.47 A zoom of the 3:2 tongue as it closes over the T1 curve. Also included are bifurcation curves that define the 2:1 entrainment regions.

Such overlap of entrainment tongues cause additional solutions to coexist at points in the region. In this case there is even an overlap of many loops of period-doubling bifurcations and torus bifurcation lines, so one can expect to observe some very complex behaviour. Most likely, this includes the simultaneous existence of periodic, chaotic, and quasiperiodic attractors.

The enlargement reveals a loop of period-doubling bifurcations inside the 3:2 tongue. As was the case in the period-two entrainment regions, the bifurcation is the first in a cascade leading to chaos.

In this work such period-doubling bifurcations have not been located in the 3:1 tongue, and we are unaware of any other examinations which have made similar observations in a period-three entrainment region.
The period-doubling bifurcations of higher period have not been traced, but their presence and the route to chaos is confirmed by the Brute-Force diagrams and Lyapunov exponents shown in Fig. 5.48 and Fig. 5.49 respectively.

In the Brute Force scan both the x and and the y variables are depicted. The scan is performed using decreasing forcing frequency, and initially the system is in a 3:1 synchronized state. The Lyapunov exponents are calculated for the solutions observed in the Brute Force diagram and presented in Fig. 5.49. The scan across the 3:2 tongue is performed at the amplitude at which the R3 point is located.

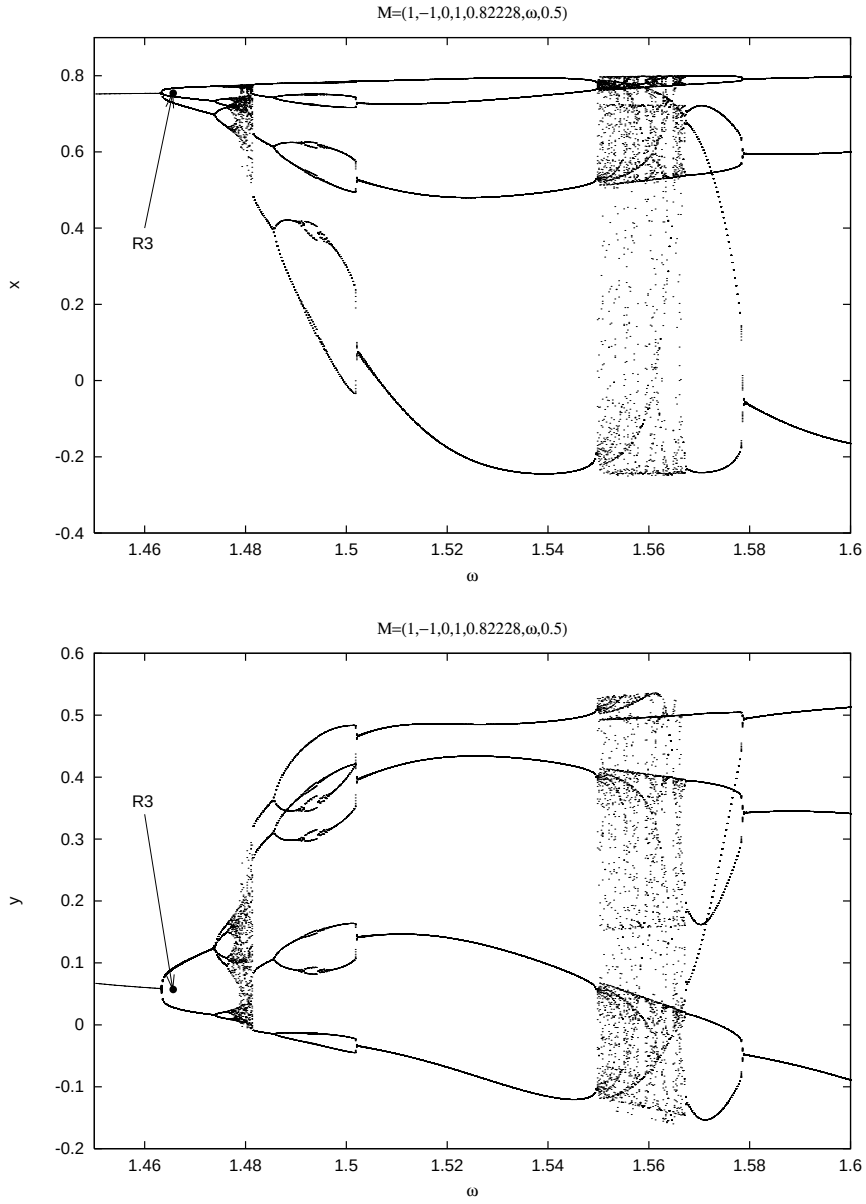

Figure 5.48 A Brute Force scan through the 3:2 tongue out into the 1:1 entrainment region. Both the x and the y variable is presented. R3 indicates the position of the resonance point located at $(x, y, \omega, A)|_{R3} = (0.753976, 0.0573065, 1.46566, 0.82228)$.

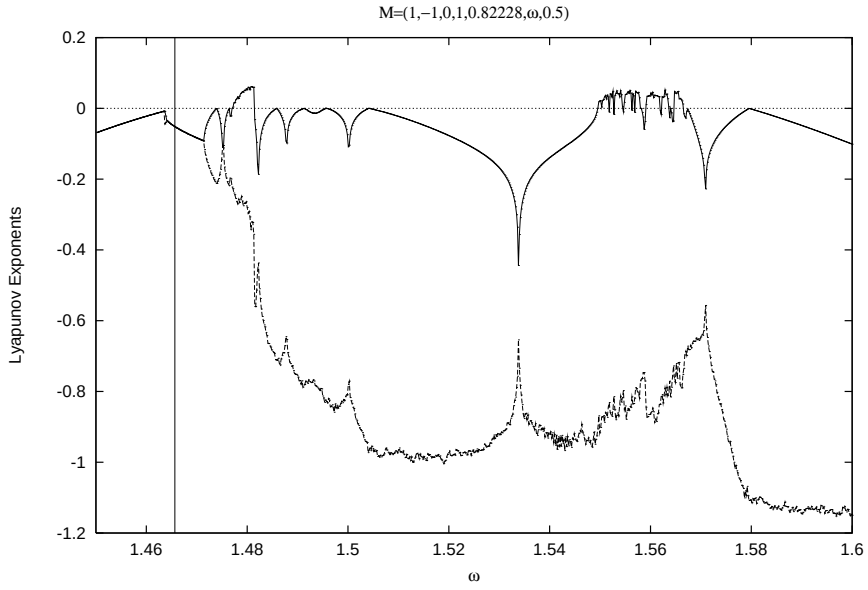

Figure 5.49 Lyapunov exponents calculated for the solutions observed in the Brute Force diagram Fig. 5.48. The vertical marker at approximately 1.46566 indicates the value of ω at which the R3 point for the 3:2 tongue is located.

Looking at the Brute Force diagrams it is seen that the period-three solution doubles to a period-six at approximately $\omega = 1.58$. It appears as if some bifurcation transient occur here. It is not easily seen from the figure but a cascade of period-doubling bifurcations accumulates at $\omega \approx 1.65$ which is also where the first positive Lyapunov exponents are observed.
Chaos is dominant in a short interval of the forcing frequency but destroyed as a window of period-four solutions is initiated through an SN4+ bifurcation. Inside the period-four window the system goes through a sequence of period-doubling bifurcations, but the route is reversed before accumulating in chaos. Here a delayed response of the Brute Force method is also observed. As the periodic window terminates, chaos is once again located as indicated by the Lyapunov exponents.

The chaotic motion disappears as the system passes through a backward PD route back "down" to the period-three solution. Finally, the 3:2 region has been traversed and 1:1 locking is located shortly after passing the R3 point.

5.4.3 Summary

- The structures of the 3:1 and 3:2 Arnol'd tongues were examined. These period-three entrainment regions were bounded solely by SN3+ bifurcations and closed smoothly above the T1 bifurcation line.
- One resonant Hopf bifurcation point was enclosed by each of the period-three tongues. At this point the period-three saddle solutions were observed to coincide and become a period-one solution.
- Global bifurcations, involving the destruction of quasiperiodic attractors through homoclinic bifurcations, were located. Based on these observations and examinations performed by [Pavlou and Kevrekidis, 1992] and [Vance and Ross, 1989] schematic illustration of the global bifurcation scenario was presented. In this global bifurcation curves passed through the R^3 point tangent to the T1 line, and connected to the SN boundary of the tongue.
- Below the resonance point one-dimensional bifurcation diagrams through the 3:1 tongue were found to exhibit a different saddle-node pairing than diagrams obtained above this point. This was explained by the fact that R^3 marks the upper bound on the homoclinic bifurcation curves.
- A cascade of period-doubling bifurcations, leading to chaos, was found inside the 3:2 tongue, but no such scenario was located in the 3:1 region.

5.5 The 4:1 and 4:5 Tongues

The 4:q entrainment regions are the last of the strong resonance tongues presented here. They are not examined in detail and have been traced primarily with the intent of clarifying how they close relative to the T1 curve.

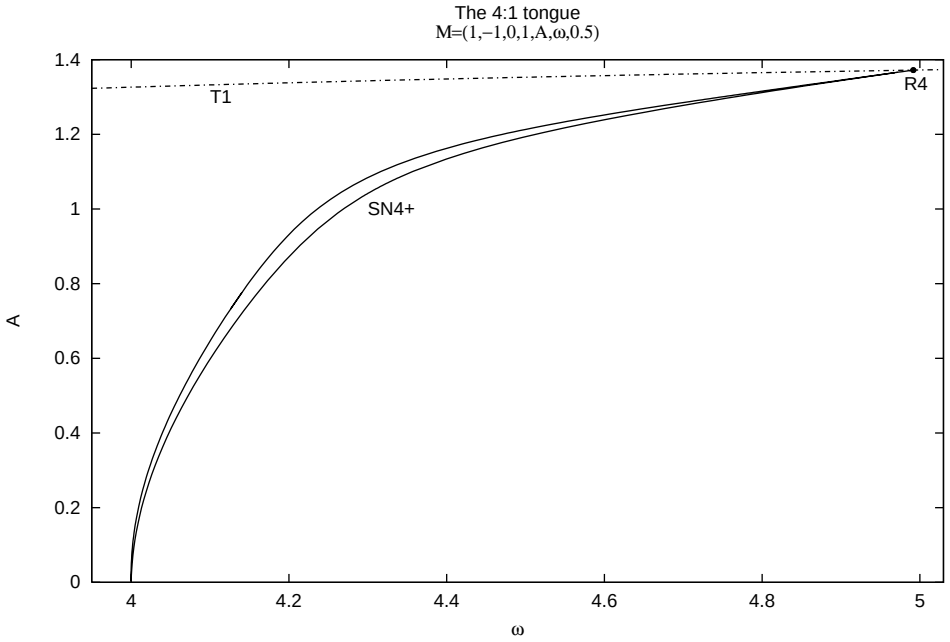

Figure 5.50 The 4:1 tongue. The tongue is very narrow and stays under the T1 curve. It closes in a wedge in a R4 point on the T1 curve.

The narrow 4:1 tongue is depicted in Fig. 5.50. The shape looks somewhat similar to that of the 3:1 entrainment region, but it closes differently at the resonance point. The boundary consists of SN4+ bifurcations which lie extremely close to each other as the T1 curve is approached and come together in the R^4 point. No overlap with the 1:1 entrainment region is observed.

A different scenario is found for the 4:5 resonance region. In the excitation diagram in Fig. 5.1 it is located between the 1:1 and 2:3 tongues. It was also presented in Fig. 5.30 where it was seen to overlap with the 2:3 tongue. A magnification of the region around the resonance point is shown in Fig. 5.51. Compared to the 4:1 tongue, the wedge, in which it closes at this point, is very wide, but the primary difference is the fact that this tongue crosses the T1 curve.

In [Pavlou and Kevrekidis, 1992] a scenario similar to the one observed for the 4:1 tongue is found, but it is also indicated that the closure of the 4:q

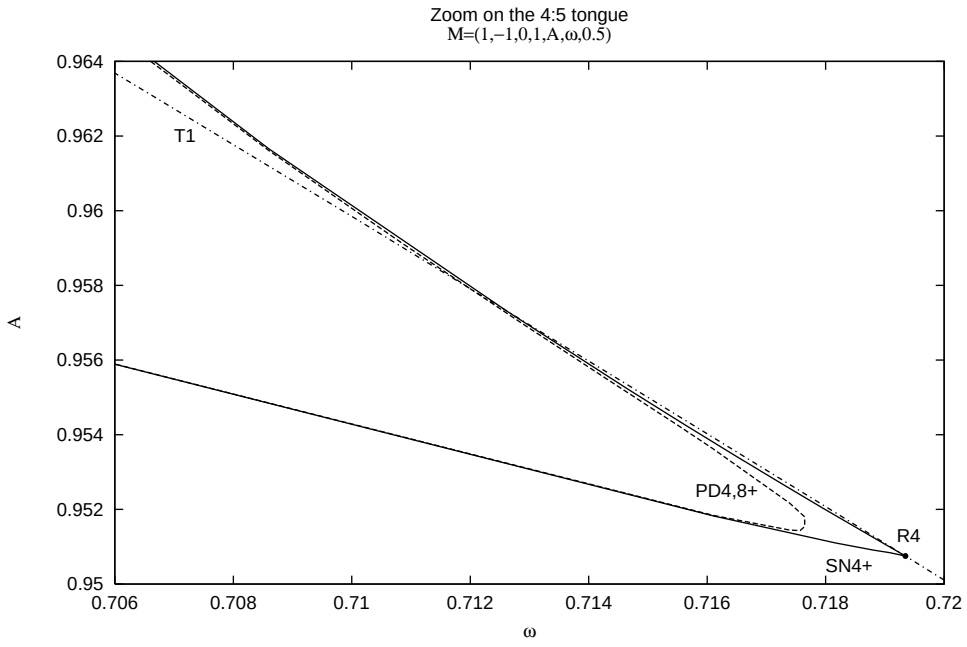

Figure 5.51 Zoom on the closure of the 4:5 tongue. Notice that the tongue encloses a PD4,8+ loop and that the T1 curve passes through the tongue. The 4:5 closes in a wedge at the R4 point on the T1 curve.

tongues has not been fully examined and understood. There does, however, seem to be a strong indication that they all close in wedges as observed here.

Another noteworthy feature of the 4:5 tongue is the period-doubling loop it encloses. This is another aspect which differs from the 4:1 region. No closer examinations have been carried out inside the PD loop, but it is suspected that a cascade of period-doubling bifurcations is present, similar to the ones in the 2:3 and 3:2 tongues.

5.5.1 Summary

- The 4:1 and 4:5 tongues were traced and found to have boundaries of period-four saddle-stable-node bifurcations. Both tongues closed in wedges at the R^4 resonance points on the T1 bifurcation curve.
- An overlap with the T1 curve, and thus the 1:1 entrainment region, was observed for the 4:5 tongue, but the boundaries of the 4:1 region stayed beneath this line.
- A loop of supercritical period-doubling bifurcations was found inside the 4:5 tongue.

5.6 Collapse of the Arnol'd Tongues

What is called the workpoint in this paper corresponds to the 'natural' state of an unperturbed autonomously oscillating system. Its position relative to the Hopf bifurcation will differ from system to system. A chemical oscillator is an example of a system in which the location of the workpoint can be altered. An externally imposed periodic variation of the concentration of a specific reactant would correspond to a forcing of the oscillator. Before subjecting the system to this forcing, the nature of its autonomous oscillations could be adjusted by means of other externally controllable parameters such as temperature, the amount of a catalyst or simply the mean value of the

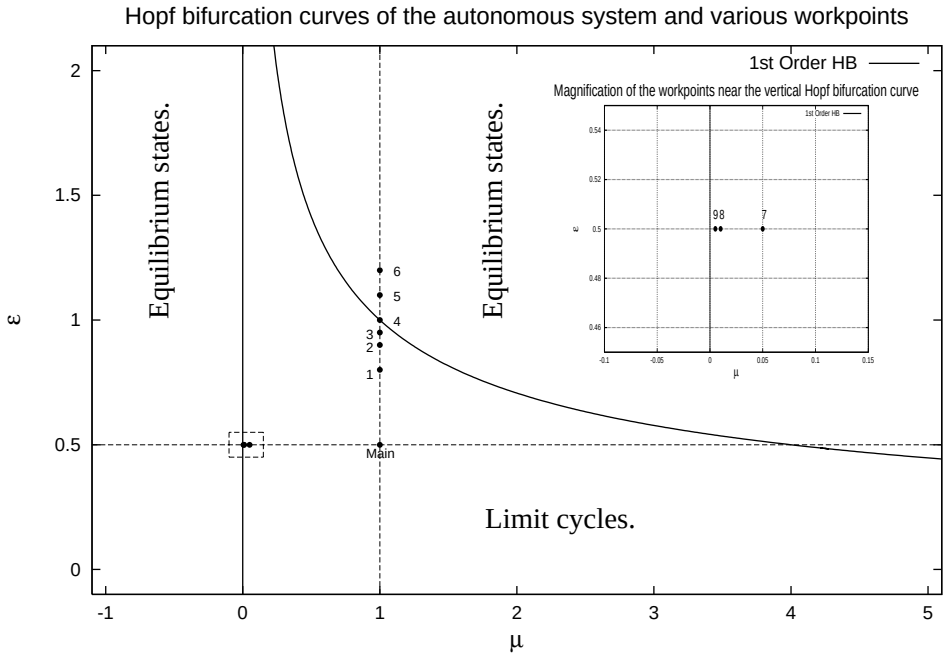

Figure 5.52 Hopf bifurcation curves and various workpoints. The numbers correspond to the excitation diagrams presented

reactant, thus effectively moving the workpoint.
The possible effects of such variations are examined this section.

To this point all the entrainment regions presented, save the one in Fig. 5.29, have been obtained at one particular set of parameters; $\mathbf{M} = (1, -1, 0, 1, A, \omega, 0.5)$. The choice of $\alpha = -1, \beta = 0$ and $\Omega = 1$ was discussed in Chapter 3. The workpoint is given by the other two parameters, μ_0 and ϵ. These were chosen to yield a representative excitation diagram. The workpoint corresponding to this choice is labeled 'Main' in Fig. 5.52. The effects of forcing around the other labeled points will be presented in the following.

Two primary approaches to the workpoint-variation have been employed; variation of ϵ at constant μ_0, and variation of μ_0 at constant ϵ. It turns out, the Arnol'd tongues are destroyed as the workpoint is moved into a region in which the autonomous oscillations are not sustained. There are, however, variations in some aspects of the tongue destruction depending on whether it is the $\mu = 0$ or the $\mu = 1/\epsilon^2$ bifurcation line that is crossed.

5.6.1 Variation of the Workpoint - Scenario One

Since the first attempts at forcing the normal form, it has been known that decreasing the parameter ϵ towards zero leads to a narrowing of all the entrainment regions. This low-ϵ collapse of the tongues is a result of the high degree of symmetry of the generic normal form. No 'coupling' between the forcing and the system occurs in this limit and subsequently no entrainment is observed. When the parameter is increased at constant $\mu > 0$ the upper Hopf bifurcation is approached. For $\mu = 1$ this bifurcation is situated at $\epsilon = 1$. The series of excitation diagrams in Fig. 5.53 show the 1:1 and 2:1 tongues at the points labeled 1 through 6 in Fig. 5.52. The tongues are somewhat crude compared to the ones presented previously, but the level of details is sufficient for the present discussion.

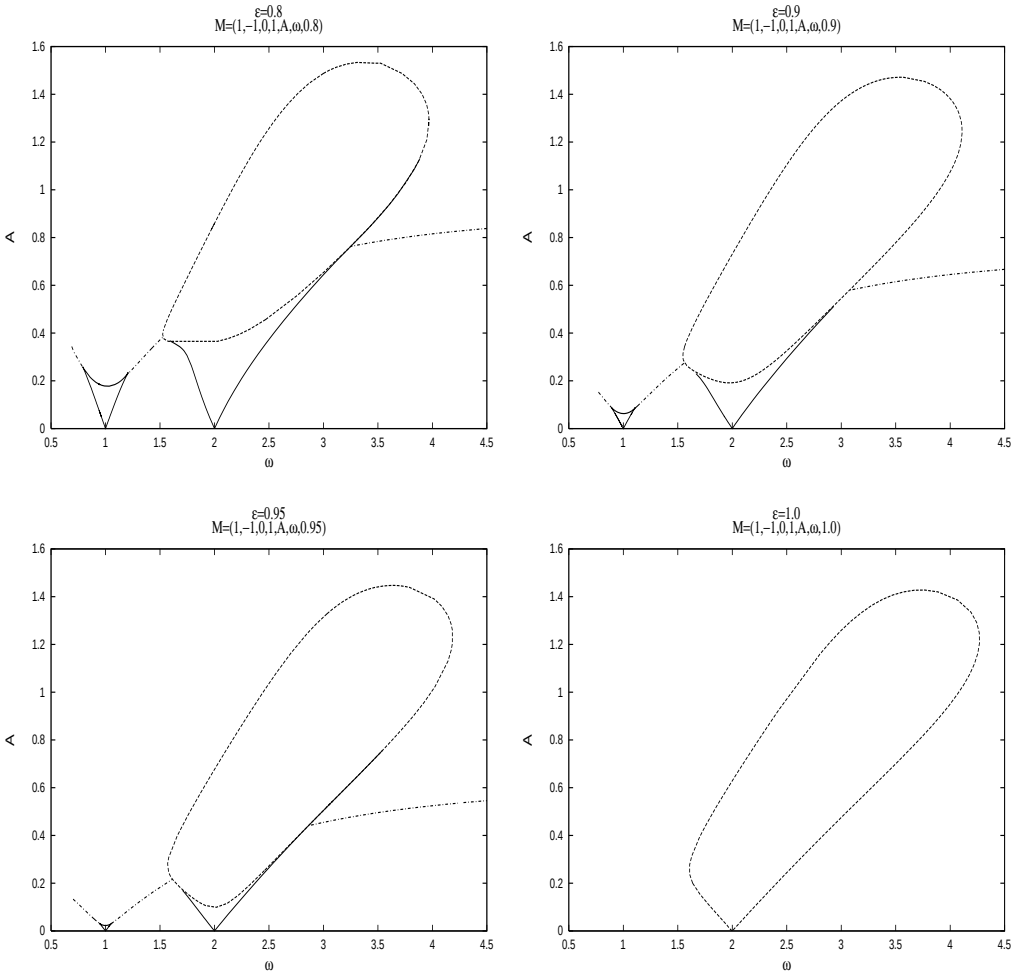
ε=0.8
M=(1,−1,0,1,A,ω,0.8)
ε=0.9
M=(1,−1,0,1,A,ω,0.9)
ε=0.95
M=(1,−1,0,1,A,ω,0.95)
ε=1.0
M=(1,−1,0,1,A,ω,1.0)
A
ω

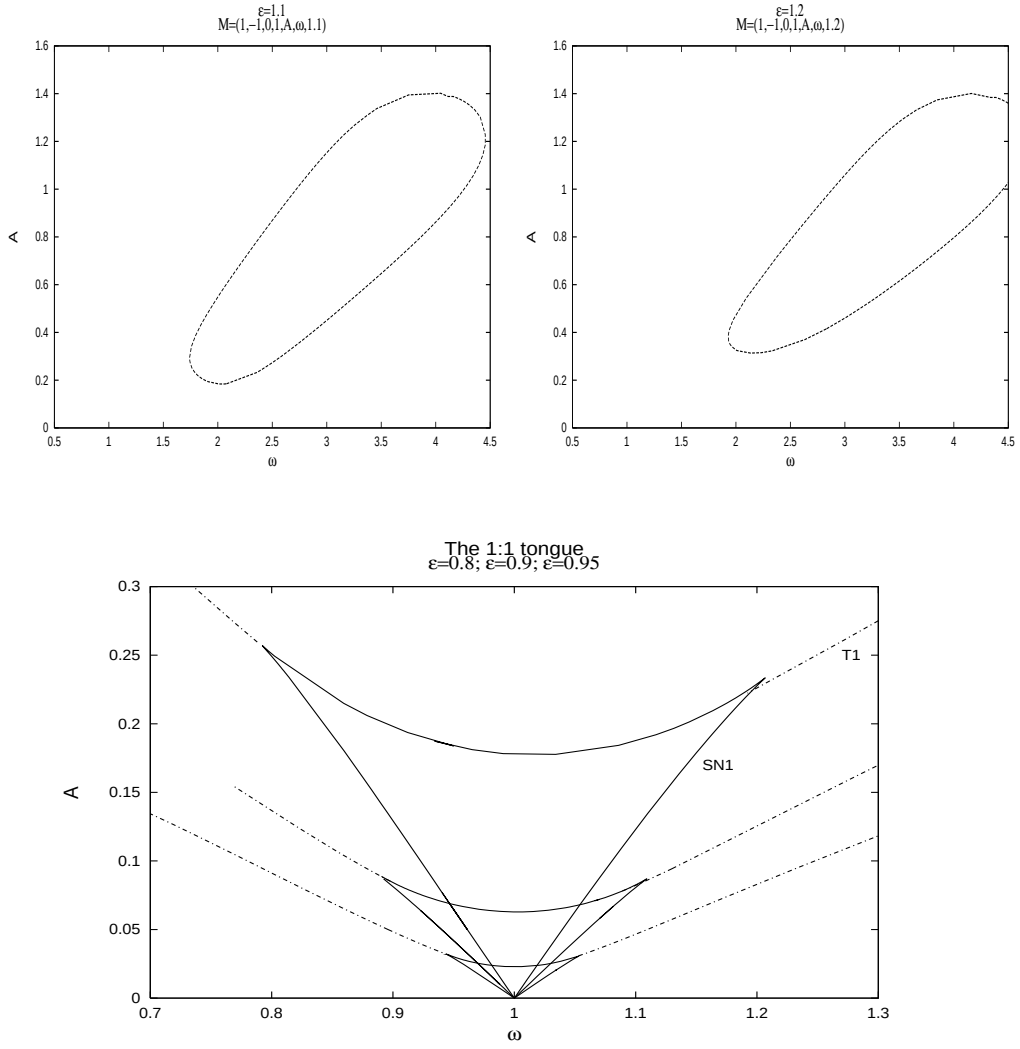

Figure 5.53 Destruction of the 1:1 and 2:1 tongues as ϵ is increased. As the Hopf bifurcation curve is crossed, the T1 tongue boundaries coincide with the ω axis. The bottom figure is an enlargement of the 1:1 tongue at the various stages. μ_0 is constant and equal to one.

When comparing the tongues in the first figure with those in the excitation diagram of Fig. 5.1, they are observed to have changed in size. Most notably the upper SN bound of the period-one tongue has moved from an amplitude of approximately 0.9 to somewhere in the vicinity of 0.2. As ϵ is further increased the 1:1 Arnol'd tongue continues to shrink. In addition to the reduction in height it opens at an increasing angle. The evolution of this tongue is emphasized in the last picture in Fig. 5.53. As the extent of the saddle-node boundary is decreased, the line of torus bifurcations running between the two tongues becomes longer and moves closer to the ω axis. Even if the size of the Arnol'd tongue is reduced, the 1:1 entrainment region as a whole becomes increasingly dominant at the expense of the quasiperiodic regime and the resonance regions that are known to terminate on the T1 bifurcation line. In the course of the first three frames, the gradual widening of the 1:1 tongue is accompanied by changes in the 2:1 tongue. While the top of the period-doubling loop does not move much, the bottom is pulled toward lower amplitudes, and the loop is thus elongated. At the same time the SN2 boundary is reduced in size in a manner somewhat similar to that of the 1:1 tongue. It does not widen significantly but the upper bound moves closer to the ω axis.

As the workpoint reaches the Hopf bifurcation, the T1 line and the resonance points located on it, coincide with the ω-axis. At this point the period-doubling loop has developed a tip at the bottom, which just touches the axis at a point in which the R^2 resonance points have collided. In short no SN bounded resonance tongues exist, and besides the quite large 2:1 locking region inside the loop, no entrainment regions other than the 1:1 are found. The loop seems to have been 'cut off' and is now floating upwards as the workpoint is shifted further into the equilibrium region.
A scenario qualitatively similar to the above is found in the forced Brusselator by [Knudsen et al., 1991].

5.6.2 Variation of the Workpoint - Scenario Two

Moving the workpoint towards the $\mu = 0$ bifurcation also causes the destruction of the Arnol'd tongues. Many aspects of the collapse are similar to those seen when approaching the high frequency equilibrium region. The saddle-node boundary of the 1:1 tongue is diminished while the period-one entrainment region widens, and eventually the T1 line comes all the way down to the ω axis.

A difference is observed, however, in the collapse of the period-two resonance region. The three plots in Fig. 5.54 clearly illustrate how the 2:1 tongue, including the period-doubling loop, shrinks both in height and width. It is difficult to distinguish the structure of the tongue in the last two frames, but by considering the magnification in Fig. 5.55, one should be convinced that the 2:1 tongue retains the structure characteristic of a period-two tongue. The upper curve of saddle-node bifurcations has not been included in the enlargement of the 1:1 tongue, but is still present.

After the destruction of the Arnol'd tongues, there is no remaining period-two entrainment. The loop of period-doubling bifurcations vanished along with the SN2 boundary. Further reduction of μ_0 does not alter the scenario.

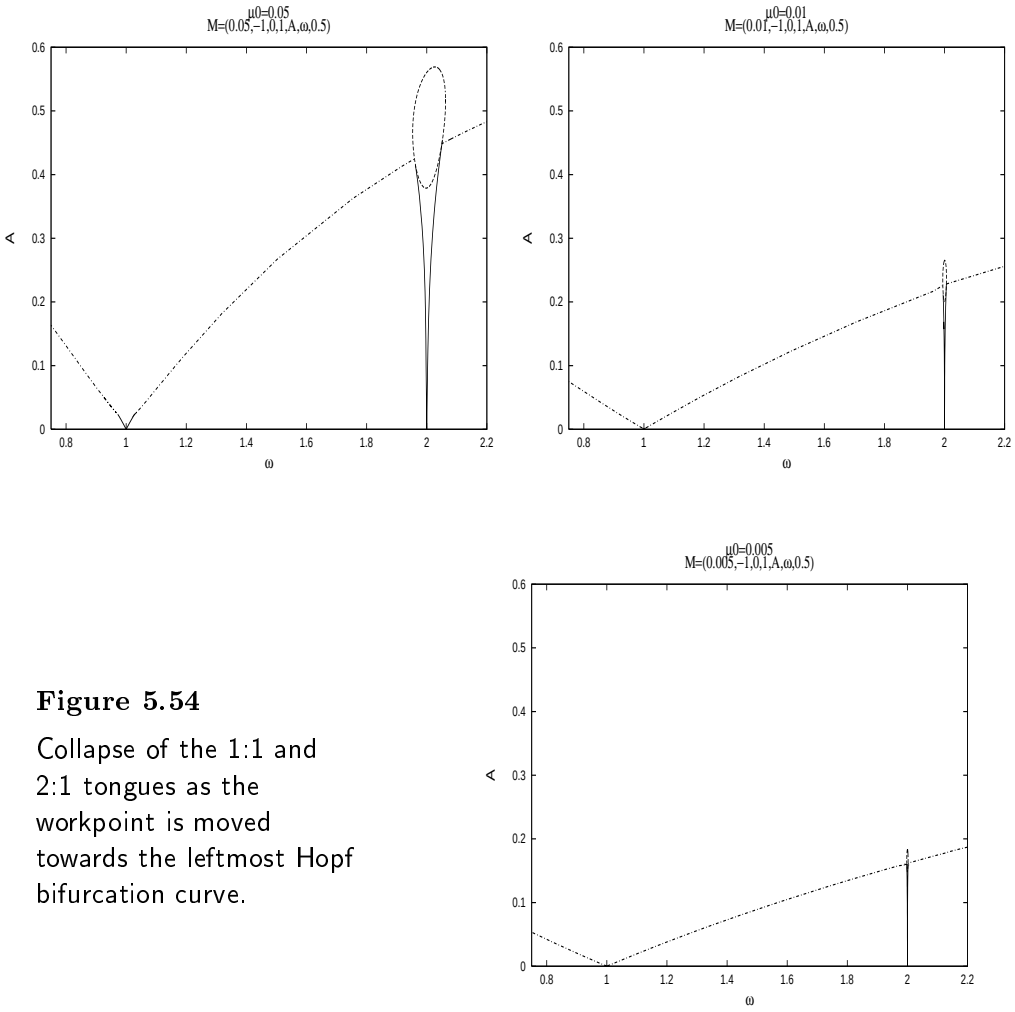

Figure 5.54

Collapse of the 1:1 and 2:1 tongues as the workpoint is moved towards the leftmost Hopf bifurcation curve.

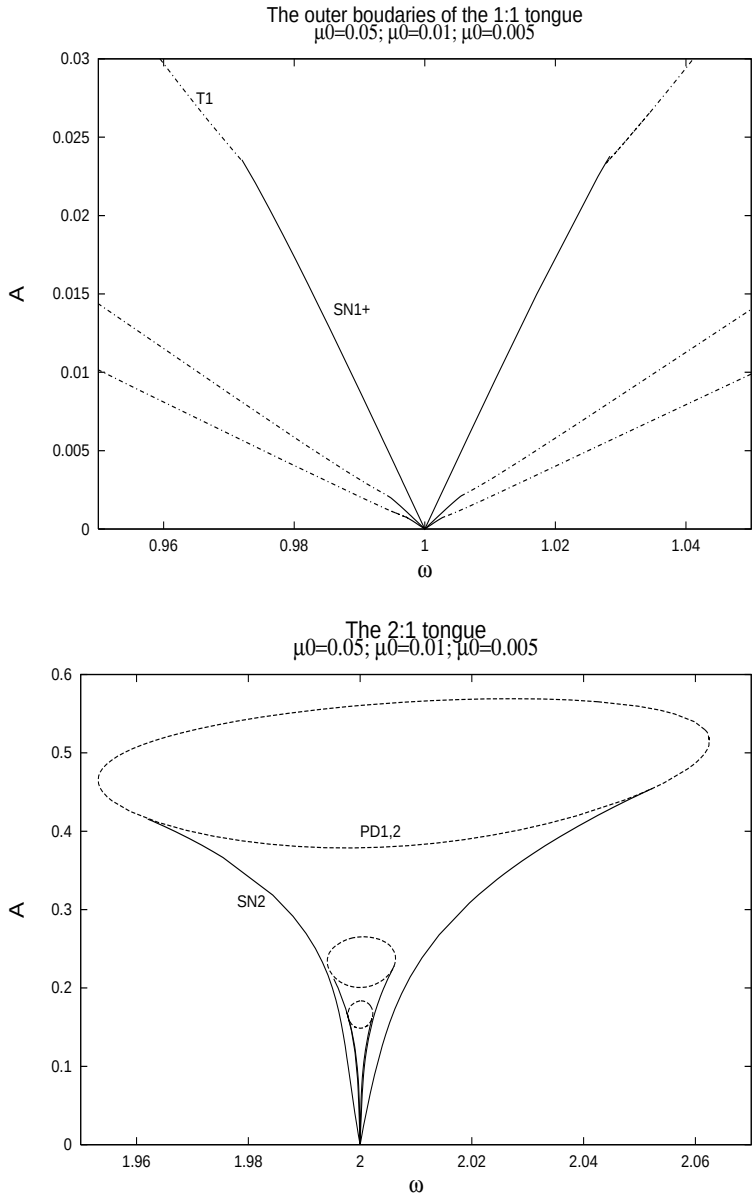

Figure 5.55 Magnification of the 1:1 and 2:1 tongues as μ_0 is decreased. The upper SN boundary of the 1:1 tongue has not been included in the figure. ϵ is constant and equal to 0.5.

5.6.3 Discussion

When forcing around a point inside an oscillatory region, the tongues were observed to close on the T1 curve at *critical amplitudes* large enough to bring the forcing parameter close to, or even across, the Hopf bifurcation.
After the destruction of Arnol'd tongues, in the first scenario, a region of 2:1 entrainment is observed. The onset of this entrainment also seems to occur at critical amplitudes. Its existence might thus be explained by the interaction with the underlying Hopf bifurcation.
However, since the interaction with the $\mu = 0$ bifurcation, in the second scenario, does not lead to a similar entrainment region, additional factors must be of consequence.
Reference is made to the analyses of the isoclines of the unforced system in Section 3.4. The analyses showed the equilibrium regions to differ, as only one of them ($\mu > 1/\epsilon^2$) contained areas of the state space in which the flow was repelled from the stable equilibrium solution.

We believe these variations in the transient dynamics to be the cause of the differences in the post-collapse entrainment scenarios. Since the forced Brusselator exhibits tongue destructions similar to the first scenario presented, an examination of the unforced Brusselator could be of interest.

5.6.4 Summary

- The effect of moving the workpoint across the Hopf bifurcations at $\mu = 0$ and $\mu = 1/\epsilon^2$ was examined. This was done along lines of constant μ_0 and ϵ respectively. The results were presented in an excitation diagram, containing the 1:1 and the 2:1 tongues.

- Arnol'd tongues existed only when the workpoint was located in a region containing oscillations of the unforced system.

- As the workpoint coincided with the first order Hopf bifurcation of the autonomous system, the 1:1 tongue vanished and the T1 bifurcation curve coincided with the ω-axis. This caused the destruction of all resonance horns. Subsequently, the resonant Hopf bifurcation points were located at rational values on the ω-axis.

- Moving the workpoint into the equilibrium regions of the autonomous system caused two different types of collapse of the 2:1 tongue. Only 1:1 synchronization was located for $\mu < 0$ whereas 2:1 entrainment was observed for $\mu > 1/\epsilon^2$. The period-two synchronization was found inside the period-doubling loop of the 2:1 tongue and remained after the collapse of the Arnol'd tongues.

CHAPTER 6

Conclusion

A detailed computational study of the dynamics of a forced oscillator was presented. The system examined was a modified version of the generic normal form for a Hopf bifurcation subjected to an external sinusoidal perturbation. A package in C++ containing numerical continuation methods was optimized and expanded with additional methods during the course of the project.
Breaking of the symmetry of the normal form proved to be necessary in order to achieve a coupling between the external forcing and the autonomous oscillations of the system. A parameter was, therefore, introduced enabling the strength of the coupling to be controlled.
The symmetry of the autonomous system was broken without losing control of the autonomous oscillations. Parameters controlling the stability and frequency of the oscillations were chosen, so that the system included two supercritical Hopf bifurcations enclosing a region of autonomous oscillations. Moreover, the frequency of these oscillations was kept constant throughout their stability region.

The investigation of a representative tongue structure in the forcing parameter plane was presented. Strong resonance tongues were examined in greater detail, more specifically the 1:1, 2:1, 2:3, 3:1, 3:2, 4:1, and the 4:5 tongues were studied. Attention was also given to the focus-node transitions of period-one and period-two solutions occurring in the parameter plane.
At low forcing amplitudes the tongues were found to be of a rather similar structure but as the amplitude was increased the characteristic features of the various tongues became evident. Complex nonlinear behaviour was observed, including chaos inside a cascade of period-doubling loops within the

2:1, 2:3, and 3:2 entrainment regions. The initial period-doubling loops were traced and presented. A period-doubling loop inside the 4:5 tongue was also observed, indicating possible chaos within that tongue.
Motivated by locating codimension two points, neighbouring regions to these points were examined by manifold analysis. These examinations revealed the presence of global bifurcations in the 1:1 and 3:1 tongues.
Based on considerations of the possible loci of codimension two points related to the 2:q tongues, three different possible scenarios were postulated. Two of these were detected in the present study.

Under variation of the workpoint, around which a system parameter of the autonomous system was perturbed, the resulting bifurcation structures of the dominant 1:1 and the 2:1 tongues were examined. The workpoint was moved between regions containing only one stable attractor of the underlying autonomous system. This included the movement out of a region of limit-cycles and into two different regions containing equilibrium solutions. The examinations were performed with and without varying the strength of the coupling between the forcing and the autonomous system. Hence, a four-parameter numerical bifurcation analysis was carried out.

Moving the workpoint into a region that does not sustain oscillations of the unforced system, caused the destruction of the Arnol'd tongue structure. The collapse was caused by an increasingly dominant 1:1 entrainment in the forcing parameter plane. The 1:1 Arnol'd tongue was continuously widened and reduced in height as the workpoint moved towards a Hopf bifurcation. This caused pairs of first- and second-order resonance points of codimension two to collide as the period-one torus bifurcation curve coincided with the forcing frequency axis at zero forcing amplitude. This, in effect excluded the possibility of Arnol'd tongues.
Differences were observed in the destruction of the dominant 2:1 tongue. It is suggested that the differences in their collapse are due, primarily, to the differences in the transient dynamics of the autonomous system.

Workpoint variation, and the forcing of systems with various underlying bifurcation structures, provide many interesting aspects for further examinations. We are convinced that the numerical analyses presented in this

thesis have elucidated features common to oscillators forced across a Hopf bifurcation. In addition to this, the model constructed here provides a high degree of control of the bifurcations and dynamics of the autonomous system. Hence, it is our hope that our work can provide a foundation for future investigations of forced oscillators.

APPENDIX A

Additional Figures

In this appendix vector fields, isoclines and limit cycles of the autonomous system are portrayed. These corresponds to different pairs of the system parameters μ and ϵ for $\alpha = -1, \beta = 0$, and $\omega = 1$. Isoclines are drawn with thick lines and limit cycles with thin lines.
The stability regions of the unforced system, in the (μ, ϵ) parameter plane are indicated in the figure below:

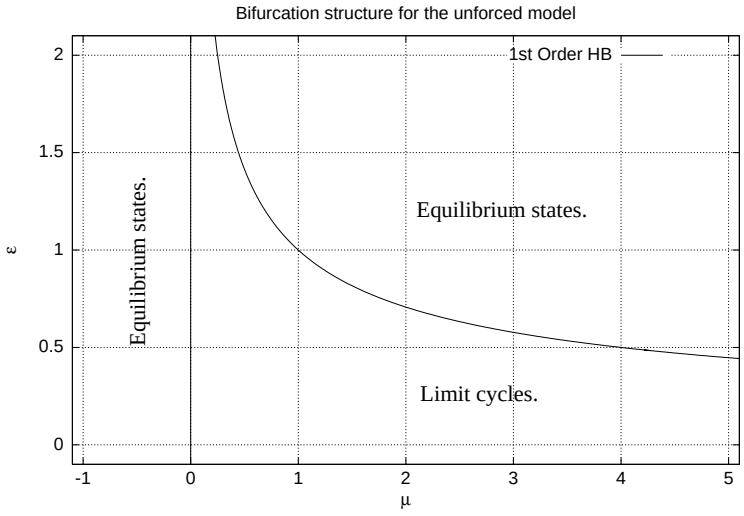

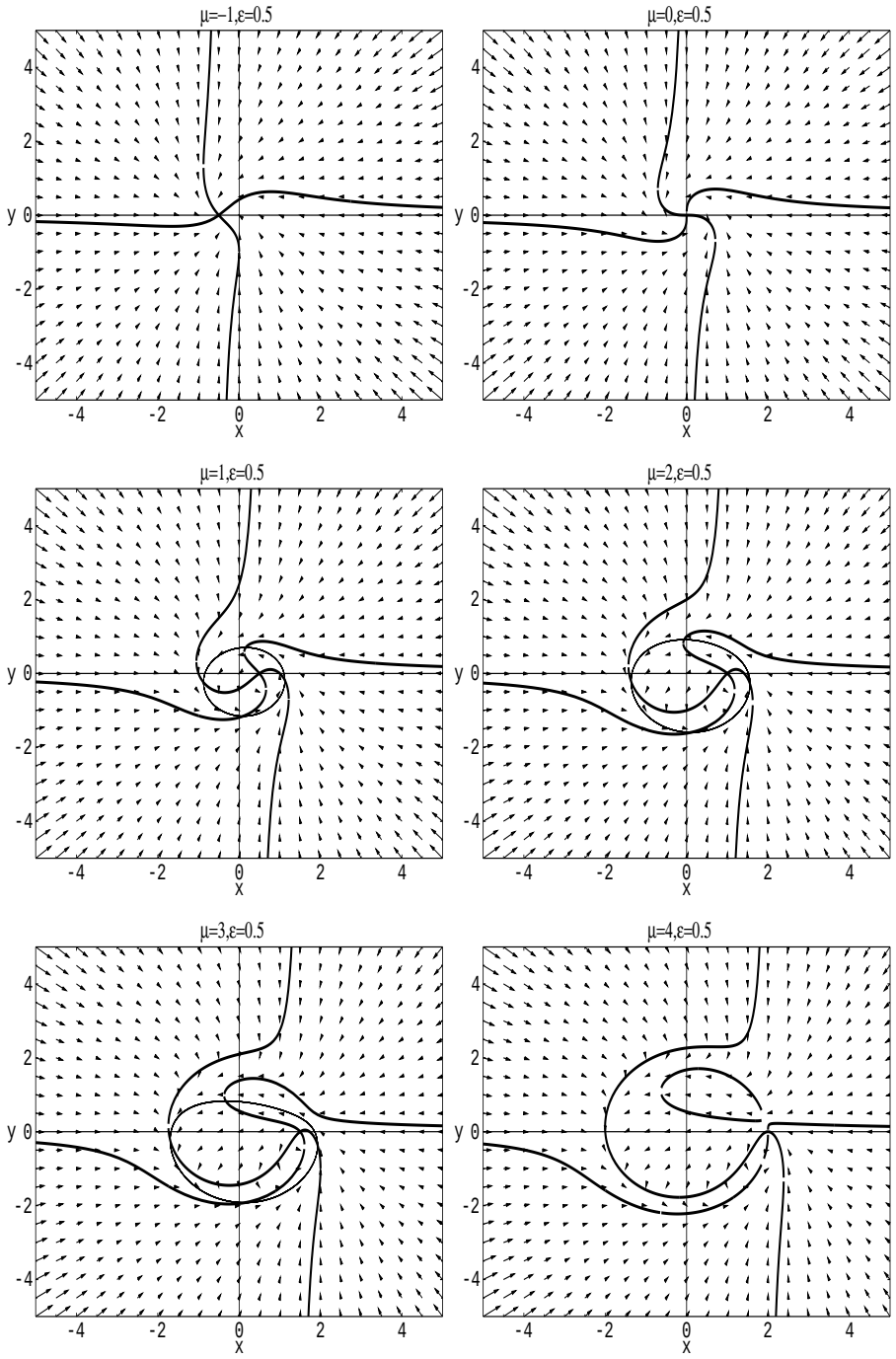
μ=−1,ε=0.5
μ=0,ε=0.5
μ=1,ε=0.5
μ=2,ε=0.5
μ=3,ε=0.5
μ=4,ε=0.5
y
x
4
2
0
-2
-4

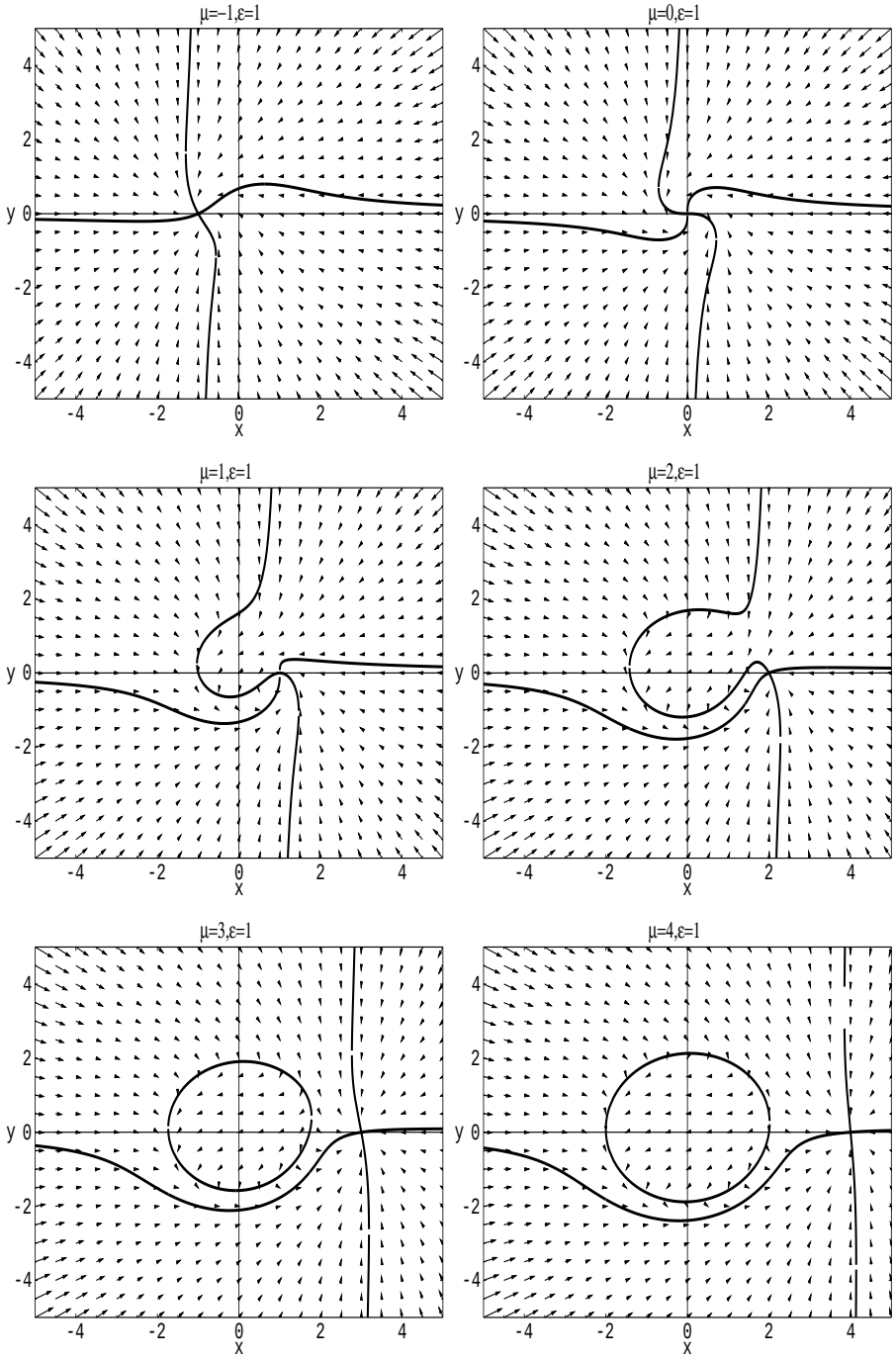
μ=−1,ε=1
μ=0,ε=1
μ=1,ε=1
μ=2,ε=1
μ=3,ε=1
μ=4,ε=1
y
x
4
2
0
-2
-4

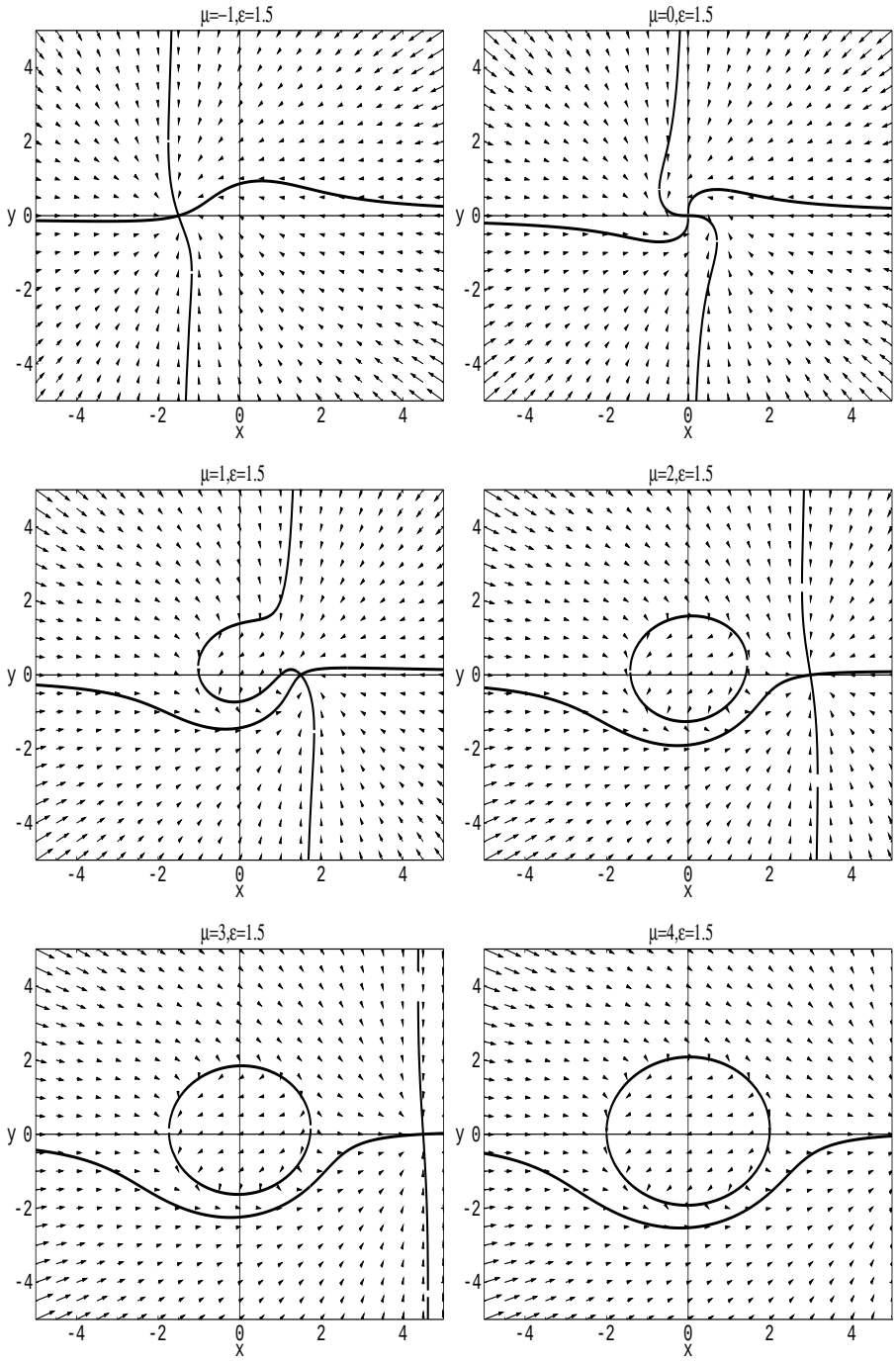
μ=−1,ε=1.5
μ=0,ε=1.5
μ=1,ε=1.5
μ=2,ε=1.5
μ=3,ε=1.5
μ=4,ε=1.5
y
x
4
2
0
-2
-4

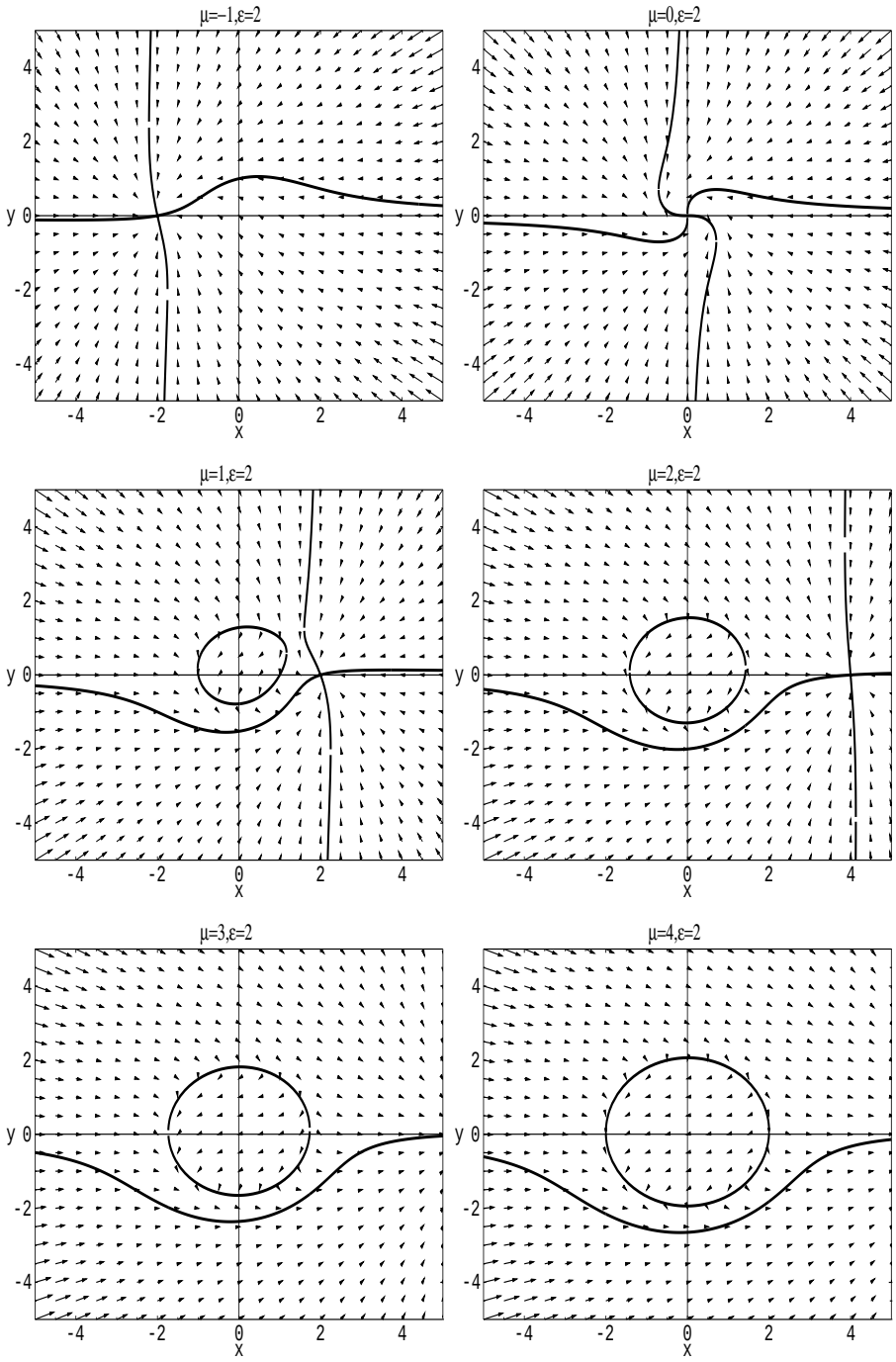
μ=−1,ε=2
μ=0,ε=2
μ=1,ε=2
μ=2,ε=2
μ=3,ε=2
μ=4,ε=2
y
x
4
2
0
-2
-4

APPENDIX B

Numerical Methods

THE PURPOSE of this appendix is, to explain in some depth, the different numerical routines which have been implemented and used in the analysis of the nonlinear dynamical system.

We shall explain (i) a numerical integration scheme (i.e. Runge-Kutta), (ii) how to set up a Stroboscopic Poincaré-section, (iii) a method of constructing one dimensional invariant manifolds, (iv) a root solving scheme (i.e. Newton-Raphson), and finally (v) the Continuation method.

B.1 Numerical Integration

B.1.1 General

Consider a N dimensional nonautonomous system of ordinary differential equations. The equations describing the flow are of the form

$$\dot{\mathbf{x}} = \mathbf{F}(\mathbf{x}, t, \mathbf{M}) = \begin{pmatrix} F_1(\mathbf{x}, t, \mathbf{M}) \\ F_2(\mathbf{x}, t, \mathbf{M}) \\ \vdots \\ F_N(\mathbf{x}, t, \mathbf{M}) \end{pmatrix}. \tag{B.1}$$

Here $\mathbf{x} \in \mathbb{R}^N$ is the state vector, $t \in \mathbb{R}$ is time, and $\mathbf{M} \in \mathbb{R}^P$ is a P dimensional parameter vector. We wish to approximate the solution to the initial value problem:

$$\mathbf{x}(t) = \mathbf{x}_0 + \int_{t_0}^{t} \mathbf{F}(\mathbf{x}(\tau), \tau, \mathbf{M}) d\tau, \text{ where } \mathbf{x}_0 \equiv \mathbf{x}(t_0), \tag{B.2}$$

which often cannot be solved analytically.

Numerical integration schemes can be classified into two groups: one-step and multi-step methods. One-step methods estimate the solution at a time t_n only based on the information of the state of the system at time t_{n-1}. An i-order multi-step method requires information to a time series describing the system at different times $t_{n-i}, t_{n-i+1}, \ldots, t_{n-1}$ before an estimate of the state of the system at time t_n can be calculated.

Many arguments can be made in favor of both methods. Generally, one-step methods have better and more robust error estimates. Furthermore, they avoid the problem of generating an initial time series, thus being relatively easy to implement. In the following we will describe two so-called Runge-Kutta (RK) methods. Both of them are one-step methods. The first method is the RK-4 integration scheme which uses a fixed time step; the second one is the RK-56 method which uses a variable step-length.

B.1.2 The Runge-Kutta Methods

The simplest of all numerical integration methods is Euler method,

$$\mathbf{x}_{n+1} = \mathbf{x}_n + h\mathbf{F}(\mathbf{x}, t). \tag{B.3}$$

Clearly, this is a one-step method which takes the step h in the direction of the gradient $\mathbf{F}$. It is easy to change the step-length in Euler's method but the method is not very stable for large step-length. The Runge-Kutta methods use the same principle as Euler's method, which can indeed be called a 1st order Runge-Kutta method (RK-1). The idea behind the methods is to calculate the gradient in a number of points along the step h from the state $\mathbf{x}(t)$, and to use these in the estimate of the state of the system at $\mathbf{x}(t+h)$. Hence,

$$\mathbf{x}(t+h) \cong , ^{p}(\mathbf{x}(t), t, h, \mathbf{F}) = x(t) + h\sum_{i=1}^{n} b_i k_i. \tag{B.4}$$

$, ^{p}$ is a p'th-order estimate of the state $\mathbf{x}(t+h)$, h is the step-length and n is the number of sub-steps the method is using. The constants b_i are used to weight the gradients k_i which are calculated from

$$k_i = \mathbf{F}(\mathbf{x}(t) + h\sum_{j=1}^{n} a_{ij}k_i,\ \ t + c_i h), \tag{B.5}$$

where c_i and a_{ij} are constants which are related by

$$c_i = \sum_{j=1}^{n} a_{ij}. \tag{B.6}$$

The constants are called Butcher coefficients. They describe the method and determine the order of the estimate. In methods where $a_{ij} = 0, j \geq i, j = 1, 2, \cdots, n$, every k_i is given explicitly by previously calculated $k_j, j = 1, 2, \cdots, i-1$, which naturally eases the implementation. Such methods are called explicit/classical Runge-Kutta methods.

Every numerically calculated solution is only an estimate of the unique solution of a well-posed initial value problem. The unique solution can be thought of as a single integral curve in the extended state space $\mathbb{R}^{N+1}$. Due to truncation and round-off error, the numerical solution will always wander off from this curve. The numerical solution is therefore inevitably going to be affected by the dynamics of the neighboring integral curves. Thus, the family of integral curves and their dynamics are of importance. The Runge-Kutta methods gather information on the family of curves and use this to make an estimate of the unique solution.

Fig. B.1 visualizes the principle of an n'th order Runge-Kutta method. First, as described by Eq. (B.5)-Eq. (B.6), we calculate the gradients $k_1 = \mathbf{F}(\mathbf{x}_0, t_0)$, $k_2 = \mathbf{F}(\mathbf{x}_0 + c_2 h k_1, t_0 + c_2 h)$, $\cdots$, $k_n = \mathbf{F}(\mathbf{x}_0 + c_n h k_n, t_0 + c_n h)$. We have thus gathered information on the family of integral curves. Now, by Eq. (B.4), an estimate , ^{p} can be made to describe the state of the system at the time $t_1 = t_0 + h$.

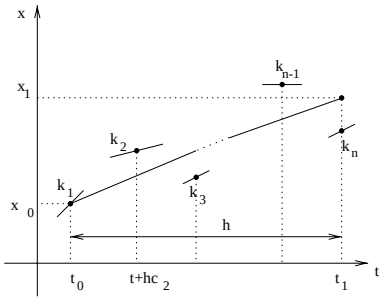

Figure B.1 Illustration of a RK-n method.

The local errors are due to truncation and round-off error. For the Runge-Kutta methods the truncation error is generally proportional to h^{p+1} and the round-off error with h^{-1}. The global error is the accumulation of the local errors over several integration steps.

We have chosen to implement a 4th-order Runge-Kutta method. Looking at the Butcher coefficients presented in Table B.1, we immediately notice some attractive features of this method. Several of the coefficients are either zero or one, keeping the numerical work during calculations to a minimum.

The step-length, h, used in the methods is easy to change, but it is difficult to tell when to either increase or decrease the step-length in order to optimize numerical speed and precision.

The RK-56 method is a numerical scheme that, with a minimum of work, calculates two estimates at the 5th- and 6th-order. Notice that we have two sets of b-coefficients in Table B.2. Naturally, at each time-step, the numerical work is much larger for the RK-56 compared to the RK-4 method. But the RK-56 has the advantage that it allows us to use the difference between its two estimates as a measure of how well the integration is proceeding. Thus, by studying this error estimate, one can get a hint on how to control the step-length. The stability of the numerical scheme is now increasingly dependent on the specific system we are integrating. Therefore, one should be careful to adjust relevant tolerances when introducing a new system. Moreover, one should check whether the integration routine is stable to variations of system parameters. If one succeeds in adjusting the RK-56 tolerances with respect to the step-control, the method often becomes an attractive alternative to RK-4. Optimally reducing the total amount of numerical work done when integrating a system, while maintaining a high order of precision. Numerical integration schemes that use variable step-length can be implemented to stop at the desired time either by interpolating between states or simply by posing restrictions on the final time-step. A 7th-order interpolation scheme is presented in [Enright et al., 1986].

B.2 Stroboscopic Poincaré-sections

B.2.1 Setting up the Poincaré-Section

A Stroboscopic Poincaré-section (P-section) is a typical choice of P-section when working with nonautonomous system; even more so, when working with forced systems. The P-section simply registers the state of the system

$$\begin{array}{c|c} c & A \\ \hline & b \end{array} = \begin{array}{c|cccc} 0 & 0 & 0 & 0 & 0 \\ \frac{1}{2} & \frac{1}{2} & 0 & 0 & 0 \\ \frac{1}{2} & 0 & \frac{1}{2} & 0 & 0 \\ 1 & 0 & 0 & 1 & 0 \\ \hline & \frac{1}{6} & \frac{1}{3} & \frac{1}{3} & \frac{1}{6} \end{array}$$

Table B.1 RK-4 Butcher Tableau [Lambert et al., 1990]

$$\begin{array}{c|c} c & A \\ \hline & b^1 \\ \hline & b^2 \end{array} = \begin{array}{c|cccccccc} 0 & 0 & 0 & 0 & 0 & 0 & 0 & 0 & 0 \\ \frac{1}{6} & \frac{1}{6} & 0 & 0 & 0 & 0 & 0 & 0 & 0 \\ \frac{4}{15} & \frac{4}{75} & \frac{16}{75} & 0 & 0 & 0 & 0 & 0 & 0 \\ \frac{2}{3} & \frac{5}{6} & \frac{-8}{3} & \frac{5}{2} & 0 & 0 & 0 & 0 & 0 \\ \frac{5}{6} & \frac{-165}{64} & \frac{55}{6} & \frac{-425}{64} & \frac{85}{96} & 0 & 0 & 0 & 0 \\ 1 & \frac{12}{5} & -8 & \frac{4015}{612} & \frac{-11}{36} & \frac{88}{255} & 0 & 0 & 0 \\ \frac{1}{15} & \frac{-8263}{15000} & \frac{124}{75} & \frac{-643}{680} & \frac{-81}{250} & \frac{2484}{10625} & 0 & 0 & \\ 1 & \frac{3501}{1720} & \frac{-300}{43} & \frac{297275}{52632} & \frac{-319}{2322} & \frac{24068}{84065} & 0 & \frac{3850}{26703} & 0 \\ \hline & \frac{13}{160} & 0 & \frac{2375}{5984} & \frac{5}{16} & \frac{12}{85} & \frac{3}{44} & 0 & 0 \\ \hline & \frac{3}{40} & 0 & \frac{875}{2244} & \frac{23}{72} & \frac{264}{1955} & 0 & \frac{125}{11592} & \frac{43}{616} \end{array}$$

Table B.2 RK-5/6 Butcher Tableau [Enright et al., 1986]

at evenly spaced time intervals T. For forced systems T is normally chosen as the period of the forcing. We can now define our P-section, $\mathbf{x}_0 \to \mathbf{P}(\mathbf{x}_0) = \mathbf{x}_1$, such that the i'th iterate will be given by,

$$\mathbf{P}^i(\mathbf{x}(t_0)) = \mathbf{x}(t_0 + iT) = \mathbf{x}_0 + \int_{t_0}^{t_0+iT} \mathbf{F}(\mathbf{x}(\tau), \tau, \mathbf{M}) d\tau. \tag{B.7}$$

Introducing the stroboscopic P-section, we reduce the order of the space of the solution by one, going from extended state space to state space. Furthermore, the analysis of the system can now be based on the theory for discrete dynamical systems. In order to apply the P-section in other more advanced numerical techniques, it is important to be able to determine it's derivatives with respect to the system variables and parameters.

B.2.2 Derivatives of the Poincaré-Section

Given an N dimensional nonautonomous system by Eq. (B.2) and an initial state $\mathbf{x}_0 = \mathbf{x}(t_0)$. The trajectory, defined as $\zeta_t(\mathbf{x}_0, t, \mathbf{M})$, that passes through $\mathbf{x}_0$ at t_0 is described by

$$\frac{d\zeta_t}{dt} = \dot{\zeta}_t(\mathbf{x}_0, t_0, \mathbf{M}) = \mathbf{F}(\zeta_t(\mathbf{x}_0, t_0, \mathbf{M}), t, \mathbf{M}). \tag{B.8}$$

Differentiating with respect to the initial condition $\mathbf{x}_0$ we find

$$D_{x_0}\dot{\zeta}_t(\mathbf{x}_0, t_0, \mathbf{M}) = D_x\mathbf{F}(\zeta_t(\mathbf{x}_0, t_0, \mathbf{M}), t, \mathbf{M}) D_{x_0}\zeta_t(\mathbf{x}_0, t_0, \mathbf{M}), \tag{B.9}$$

where $D_{x_0}\zeta_{t_0}(\mathbf{x}_0, t_0, \mathbf{M}) = I$.

Defining,

$$\varphi_t \equiv D_{x_0}\zeta_t(\mathbf{x}_0, t_0, \mathbf{M}) \in \mathbb{R}^{N\times N}, \tag{B.10}$$

we can rewrite Eq. (B.9) to the so-called *variation equation*:

$$\dot{\varphi}_t = D_x\mathbf{F}(\zeta_t(\mathbf{x}_0, t_0, \mathbf{M}), t, \mathbf{M}) \cdot \varphi_t \tag{B.11}$$

where $\varphi_{t_0} = I$.

Let us also differentiate Eq. (B.8) with respect to $\mathbf{M}$ such that

$$D_{\mathbf{M}}\dot{\zeta}_t(\mathbf{x}_0, t_0, \mathbf{M}) = D_x\mathbf{F}(\zeta_t(\mathbf{x}_0, t_0, \mathbf{M}), t, \mathbf{M}) D_{\mathbf{M}}\zeta_t(\mathbf{x}_0, t_0, \mathbf{M}) + D_{\mathbf{M}}\mathbf{F}(\zeta_t(\mathbf{x}_0, t_0, \mathbf{M}), \tag{B.12}$$

where $D_{\mathbf{M}}\zeta_{t_0}(\mathbf{x}_0, t_0, \mathbf{M}) = 0$. Defining,

$$\chi_t \equiv D_{\mathbf{M}}\zeta_t(\mathbf{x}_0, t_0, \mathbf{M}) \in \mathbb{R}^{N \times P} \tag{B.13}$$

we find the *parameter-variation equation.*

$$\dot{\chi}_t = D_x\mathbf{F}(\zeta_t(\mathbf{x}_0, t_0, \mathbf{M}), t, \mathbf{M}) \cdot \chi_t + D_{\mathbf{M}}\mathbf{F}(\zeta_t(\mathbf{x}_0, t_0, \mathbf{M}), t, \mathbf{M}) \tag{B.14}$$

where $\chi_{t_0} = 0$.

Now 'adding' the equations Eq. (B.11) and Eq. (B.14) to the original system Eq. (B.2), we have a $N(1 + N + P)$ dimensional system where we simultaneously can solve for ζ_t, φ_t and χ_t.

Define the total system $\mathbf{y} \equiv (\zeta_t, \varphi_t, \chi_t) \in \mathbb{R}^{N \times (1+N+P)}$, which will be described by

$$\begin{aligned} \frac{d\mathbf{y}}{dt} &= \mathbf{F}^y(x, t, \mathbf{M}) = \begin{pmatrix} \dot{\mathbf{x}} \\ \dot{\varphi}_t \\ \dot{\chi}_t \end{pmatrix} \\ &= \begin{pmatrix} \mathbf{F}(\mathbf{x}, t, \mathbf{M}) \\ D_x\mathbf{F}(\zeta_t(\mathbf{x}_0, t_0, \mathbf{M}), t, \mathbf{M}) \cdot \varphi_t \\ D_x\mathbf{F}(\zeta_t(\mathbf{x}_0, t_0, \mathbf{M}), t, \mathbf{M}) \cdot \chi_t + D_{\mathbf{M}}\mathbf{F}(\zeta_t(\mathbf{x}_0, t_0, \mathbf{M}), t, \mathbf{M}) \end{pmatrix}, \end{aligned} \tag{B.15}$$

where $\mathbf{y}_0 = (\mathbf{x}_0, I, 0)$.

Applying the Stroboscopic P-section to this set of equations, we find that the i'th iterate of $\mathbf{y}_0$ contains the derivatives of the P-section,

$$\begin{aligned}
\mathbf{y}_i &= \mathbf{P}^i(\mathbf{y}(t_0)) = \mathbf{y}(t_0 + iT) \\
&= \mathbf{y}_0 + \int_{t_0}^{t_0+iT} \mathbf{F}^y(\mathbf{x}(t), t, \mathbf{M})dt \\
&= \begin{pmatrix} \mathbf{x}_i \\ \varphi_i \\ \chi_i \end{pmatrix} = \begin{pmatrix} \mathbf{P}^i(\mathbf{x}_0, t_0, \mathbf{M}) \\ D_x\mathbf{P}^i(\mathbf{x}_0, t_0, \mathbf{M}) \\ D_\mathbf{M}\mathbf{P}^i(\mathbf{x}_0, t_0, \mathbf{M}) \end{pmatrix}.
\end{aligned} \tag{B.16}$$

B.3 Equilibrium Points and Periodic Solutions

In this section we shall simply state the equations which describe equilibrium points and periodic solutions. The equations are presented as functions in which the roots are the system state solutions.

Equilibrium points are found as the root to the function H:

$$\mathbf{H} = \mathbf{F}(\mathbf{x}, t, \mathbf{M}) = 0. \tag{B.17}$$

Note that the derivatives, with respect to $\mathbf{x}$ and $\mathbf{M}$, are found as

$$D_\mathbf{x}\mathbf{H} = D_\mathbf{x}\mathbf{F}(\mathbf{x}, t, \mathbf{M}) \tag{B.18}$$

and

$$D_\mathbf{M}\mathbf{H} = D_\mathbf{M}\mathbf{F}(\mathbf{x}, t, \mathbf{M}) \tag{B.19}$$

respectively.

Having already described our P-section, we can easily state an equation that can be used to determine a period k orbit:

$$\mathbf{H} = \mathbf{P}^k(\mathbf{x}, \mathbf{M}) - \mathbf{x} = 0. \tag{B.20}$$

Again, differentiating with respect to the state variable and the parameter vector gives

$$D_{\mathbf{x}}\mathbf{H} = D_{\mathbf{x}}\mathbf{P}^k(\mathbf{x}, \mathbf{M}) - I \tag{B.21}$$

and

$$D_{\mathbf{M}}\mathbf{H} = D_{\mathbf{M}}\mathbf{P}^k(\mathbf{x}, \mathbf{M}) \tag{B.22}$$

respectively.

B.4 Construction of Invariant Manifolds

B.4.1 General

This section is a brief summary of the technique used in constructing invariant manifolds of periodic solutions.

For the fixed point $\mathbf{x}^*$ of a period k solution we have the following eigenvalue problem

$$\eta_N D_{\mathbf{x}}\mathbf{P}^k(\mathbf{x}^*, \mathbf{M}) = \eta_N \lambda_N, \tag{B.23}$$

where η_N represents the eigenvectors, and λ_N the corresponding eigenvalues.

The eigenvectors, whose corresponding eigenvalues lie inside the unit circle, span the stable subspace E^s (the stable manifold). Eigenvectors, whose corresponding eigenvalues lie, on the unit circle, span the center subspace E^c (the center manifold). Finally, the unstable subspace E^u (the unstable manifold) is spanned by the eigenvectors whose corresponding eigenvalues lie outside the unit circle.
Hence,

$$\begin{aligned} E^s &= span\{\eta_1, \eta_2, \cdots, \eta_s\}, |\lambda_{1\cdots s}| < 1, \\ E^c &= span\{\eta_{s+1}, \eta_{s+2}, \cdots, \eta_{s+c}\}, |\lambda_{s+1\cdots s+c}| = 1, \text{ and} \\ E^u &= span\{\eta_{s+c+1}, \eta_{s+c+2}, \cdots, \eta_{s+c+u}\}, |\lambda_{s+c+1\cdots s+c+u}| > 1. \end{aligned} \tag{B.24}$$

Initial states contained in the stable subspace cause the system to approach the periodic solution as $t \to \infty$. States initialized in the unstable subspace, lead to the periodic solution as $t \to -\infty$. Solutions initiated in the center subspace neither grow nor decay in time.

B.4.2 The Numerical Technique

Note: The following method of construction is restricted to one dimensional invariant manifolds.

Consider a first order fixed point $\mathbf{x}^*$ for which we wish to study the dynamics along the unstable manifold. The Hartman-Grobman theorem states that the local nonlinear dynamics $\mathbf{P}(\mathbf{x}, \mathbf{M})$ near a fixed point, $\mathbf{x}^*$, is qualitatively similar to the dynamics of the associated linear system $\mathbf{P}_L(\mathbf{x}, \mathbf{M}) = \mathbf{x}^* + D_{\mathbf{x}}\mathbf{P}(\mathbf{x}^*, \mathbf{M})(\mathbf{x} - \mathbf{x}^*)$.

We assume that an α exists such that the vector $\mathbf{x} = \mathbf{x}^* + \alpha\eta_u$ can be constructed to lie on the invariant unstable manifold, when η_u is the unstable eigenvector for the linearized system with the corresponding real eigenvalue $\lambda_u > 1$.

As a relative-absolute error estimate we use

$$|\mathbf{P}(\mathbf{x}^* + \alpha\eta_u, \mathbf{M}) - \mathbf{P}_L(\mathbf{x}^* + \alpha\eta_u, \mathbf{M})| < \epsilon_r \mathbf{x}^* + \epsilon_a, \tag{B.25}$$

where ϵ_r and ϵ_a are the relative and the absolute tolerances.

We now construct two windows (lists) containing states of the system $L^x = \{x_1, x_2, \cdots, x_{n_x}\}$ and $L^{px} = \{px_1, px_2, \cdots, px_{n_{px}}\}$ related in such ways that $x_{n_x} = \mathbf{P}(x_1, \mathbf{M})$ and $px_i = \mathbf{P}(x_i, \mathbf{M})$.

L^x is a list of states that have been accepted under the condition $|x_i - x_{i+1}| \leq \tilde{\epsilon_r} x_i + \tilde{\epsilon_a}$ for each i. This criteria ensure that the constructed manifolds are sufficiently smooth. We let the windows slide along the manifold accepting px_1 if it lies close to px_2. If px_1 is accepted, it is removed from L^{px} and added as the last element in L^x, simultaneously x_1 is removed from L^x. In the case where px_1 cannot be accepted, we simply expand our lists using linear interpolation so that $L^x = \{x_1, (x_1 + x_2)/2, x_2, \cdots, x_{n_x}\}$ and $L^{px} = \{px_1, \mathbf{P}((x_1 + x_2)/2), px_2, \cdots, px_{n_{px}}\}$. When implementing this method of construction much is gained by creating small procedures that manipulate the lists. Points, that within a certain tolerance lie on a straight line, can easily be reconstructed by interpolation and can thus be removed from the lists. Moreover, this helps save memory by maintaining short lists and keeps the amount of numerical work at a minimum when sliding the windows along the manifold.

The method extends to the study of higher order period k solutions substituting $\mathbf{P}(\mathbf{x}, \mathbf{M})$ with $\mathbf{P}^o(\mathbf{x}, \mathbf{M})$. *Direct invariant manifolds* for which $\lambda_u > 1$ are constructed choosing $J = k$. Because of the 'flipping' dynamics along the *inverse invariant manifolds* where $\lambda_u < -1$, we simply choose to study the manifold as if it were of twice the order of k, setting $J = 2k$.

Although the method cannot be used to construct higher order invariant manifolds it is not entirely meaningless to apply it to one dimensional subspaces within these. After calculating eigenvectors for the linearized system of a stable or unstable node, we can use the above technique to construct the dominant one-dimensional subspace of a high order invariant manifold in the neighborhood of the fixed point. For stabile (unstable) nodes we can find the manifolds with the largest flow towards (away) the fixed point. Stable manifolds of fixed points are constructed by reversing time.

B.5 The Newton-Raphson Method

Assume that the function $H(x)$ has the root x^*. In order to locate the root we approximate

$$\mathbf{y} = \mathbf{H}(\mathbf{x}) \tag{B.26}$$

by a linearization. The change in y, dependent on the change in x, is now given by

$$\delta\mathbf{y} = D_x\mathbf{H}(\mathbf{x})\delta x \tag{B.27}$$

To locate the root in H, we now choose $\delta y = -\mathbf{H}(x)$ solving Eq. (B.27) with respect to δx we find

$$\delta\mathbf{x} = -D_x\mathbf{H}^{-1}(\mathbf{x})\mathbf{H}(x) \tag{B.28}$$

From this it is possible to write the iteration formula known as the Newton-Raphson (NR) iteration scheme. Let $\delta x = x_{i+1} - x_i$ so that

$$\mathbf{x}_{i+1} = \mathbf{x}_i - D_x\mathbf{H}^{-1}(\mathbf{x}_i)\mathbf{H}(x_i) \tag{B.29}$$

Note, that the method does not guarantee convergence, but only in a certain neighborhood of x^*. The method diverges when D_xH becomes singular, but is attractive typically as a numeric corrector since it includes quadratic convergence.

Substituting the equations, that determine equilibrium points and periodic solution in Eq. (B.31), we get the following iterations schemes:

Equilibrium points:

$$\mathbf{x}_{i+1} = \mathbf{x}_i - D_x\mathbf{F}^{-1}(\mathbf{x}_i)\mathbf{F}(x_i) \tag{B.30}$$

Periodic solutions:

$$\mathbf{x}_{i+1} = \mathbf{x}_i - (D_x\mathbf{P}^k(\mathbf{x}_i) - I)^{-1}(\mathbf{P}^k(\mathbf{x}_i) - x_i) \tag{B.31}$$

B.6 Continuation

This last section of the appendix describes the Continuation methods.

B.6.1 General

Consider a solution described as the root to the function $H = H(\mathbf{x}, \mathbf{M})$. The solution can be followed into system space by Euler-integration along the gradient from a point $(\mathbf{x}_0, \mathbf{M}_0)$. Determining the differential $DH(\mathbf{x}, \mathbf{M})$ we find that

$$D\mathbf{H}(\mathbf{x}, \mathbf{M}) = D_x\mathbf{H}(\mathbf{x}, \mathbf{M})d\mathbf{x} + D_{\mathbf{M}}\mathbf{H}(\mathbf{x}, \mathbf{M})d\mathbf{M} = 0 \tag{B.32}$$

This is a singular system of N equations with $N + P$ variables. Defining

$$\mathbf{DH}(\mathbf{x}, \mathbf{M}) \equiv [D_x\mathbf{H}(\mathbf{x}, \mathbf{M}) \quad D_{\mathbf{M}}\mathbf{H}(\mathbf{x}, \mathbf{M})] \tag{B.33}$$

we can rewrite Eq. (B.32) as

$$\mathbf{DH}(\mathbf{x}, \mathbf{M}) \begin{bmatrix} d\mathbf{x} \\ d\mathbf{M} \end{bmatrix} = 0$$

Note, that if $\mathbf{DH}(\mathbf{x}, \mathbf{M})$ has full rank the vector $[d\mathbf{x}^T \; d\mathbf{M}^T]^T$ lies in a P-dimensional subspace (L) of the former system space. The vector will be the tangent to the curve $\mathbf{H} = 0$ in the point $(\mathbf{x}, \mathbf{M})$. By adding P extra equations to Eq. (B.32) it becomes possible to solve the system and calculate the tangent.

B.6.2 1D Continuation

First consider the case where $P = 1$, $\mathbf{M} = m \in \mathbb{R}$. We are interested in developing a method that can follow a solution in the subspace $\mathbb{R}^{N+1}$ of the system space. As an extra equation to add Eq. (B.32) we use the normalization constraint

$$|| \, [d\mathbf{x}^T \; dm]^T || = 1 \tag{B.34}$$

This constraint limits $[d\mathbf{x}^T \; dm]^T$ to one of two unit vectors in the space defined by Eq. (B.6.1), thus generating a vector field $\mathcal{H} : \mathbb{R}^{n+1} \to \mathbb{R}^{n+1}$

$$\mathcal{H} = [d\mathbf{x}^T \; dm]^T \tag{B.35}$$

Solving for this vector field it is possible to follow a solution curve in a bifurcation diagram. We can use the method to study both equilibrium and periodic solutions.

Implementation

In practice, the solving of the vector field $\mathcal{H}$ is done by a method of prediction and correction although other techniques are also possible. Here we use a Euler step as predictor and the Newton-Raphson iteration scheme as a corrector.

Rewriting Eq. (B.32) as

$$D_x\mathbf{H}(\mathbf{x}, m)d\mathbf{x} = -D_m\mathbf{H}(\mathbf{x}, m)dm \tag{B.36}$$

and choosing in which direction we wish to travel in parameter space,

$$dm = \pm 1 \tag{B.37}$$

Solving Eq. (B.36) for $d\mathbf{x}$, normalizing the vector $[d\mathbf{x}^T \; dm]^T$ via. Eq. (B.34) we find

$$d\gamma^p \equiv [d\mathbf{x}^T \; dm]^T, \tag{B.38}$$

and take a step h into system space to the predictor point $\gamma^p = \gamma^p(\mathbf{x}, m)$:

$$\gamma^p \equiv [\mathbf{x}_0^T \ m_0]^T + h \ d\gamma^{pT}, \tag{B.39}$$

The state γ^p is typically close to, but seldom satisfies $H(\gamma^p) = 0$. Therefore, we use a corrector to reduce the error from the Euler integration step. Let the corrector be initialized with the predictor point:

$$\gamma^c_{i=0} = \gamma^p(\mathbf{x}, m) \tag{B.40}$$

The iteration scheme is described by the following equations:

$$\begin{bmatrix} \mathbf{DH}(\gamma^c_i) \\ d\gamma^{pT} \end{bmatrix} d\gamma^p = \begin{bmatrix} -\mathbf{H}(\gamma^c_i) \\ 0 \end{bmatrix} \tag{B.41}$$

γ^c_{i+1} is calculated from

$$\gamma^c_{i+1} = \gamma^c_i + d\gamma^c \tag{B.42}$$

In Eq. (B.41) we have imposed a constraint on the corrector steps restricting the search to a subspace perpendicular to $d\gamma^p$. This is necessary because the system $\mathbf{DH}(\gamma^c_i)d\gamma^p = -\mathbf{H}(\gamma^c_i)$ is singular.

Depending on how fast the NR-method converges/diverges, we can adjust our step-length h. If the method diverges, one can simply calculate a new predictor point using a shorter step-length, and if the method converges after just a few iterations one might want to increase the step-length.

Locating Bifurcation Points

With the means of 1D continuation it is possible to follow solutions as they pass bifurcation points or equal-eigenvalues points (EE points). One can use different techniques in locating both of these, for instance by applying the NR-method searching for a particular bifurcation. This is probably one of the faster techniques. Neglecting saddle-node bifurcations the problem is rather where along the solution curve to look for the bifurcation points. When

searching for points involving transversal intersection of different solutions one can use a check of the matrix

$$M(\mathbf{x}, m) = \begin{bmatrix} \mathbf{DH}(\mathbf{x}, m) \\ d\gamma^{pT} \end{bmatrix} \tag{B.43}$$

M only becomes singular when $\mathcal{H}$ is not well defined implying a transversal intersection.

The amount of work it takes, to calculate the eigenvalues in every point constructed on the solution curve, is relatively low for lower dimensional systems. It can also be of interest exactly how the eigenvalues behave along the curve away from the bifurcation points. We have thus chosen to calculate the eigenvalues in all points. This allows us to use a technique to locate bifurcation/EE points that work in the same manner as the Time-Half method known from construction of P-sections.

After accepting a new point along the solution curve, we check whether a change of (i) stability of the solution or (ii) the complexity of the eigenvalues has occurred. If we wish to locate the bifurcation or EE point that we have just over-stepped, we simply go back to our initial state and decrease our step-length into system space. How to decrease the step-length can be optimized using the information of the norm of the relevant eigenvalue in the initial point and in the point that has over-stepped the bifurcation/EE point. The method is relatively fast, guarantees convergence - and has another great advantage: Because of the numerical limits, a bifurcation point can only be located within a certain accuracy. Generally, we will always be a little off from the true point, and when using, say the NR-method, we may end up on either side of the bifurcation point. This detail is of importance while doing advanced analysis on the system, maneuvering along the solution curves in system space, while changing control parameter. Using the Step-Reducing (SR) method we avoid the problem and are guaranteed to locate the desired point from the 'incoming' side on the solution curve.

B.6.3 2D Continuation

Having located a bifurcation point it is possible to follow this bifurcation into $\mathbb{R}^{N+2}$ system subspace with the technique 2D continuation. In princi-

ple, the method works in the same manner as 1D continuation, we just need to add two equation to Eq. (B.32). Again we choose to use the normalization constraint as the first equation. As the second we wish to formulate an equation that attempts to 'lock' the critical eigenvalue λ_c. Say we are studying a periodic solution. We then pose the following restricting equation

$$D_x\lambda_c d\mathbf{x} + D_{\mathbf{M}}\lambda_c d\mathbf{M} = 0 \tag{B.44}$$

here $D_x\lambda_c = [D_{x_1}\lambda_c \; D_{x_2}\lambda_c \; \cdots \; D_{x_N}\lambda_c]$ and $D_{\mathbf{M}}\lambda_c = [D_{m_1}\lambda_c \; D_{m_2}\lambda_c]$.

Again we choose a direction to travel in the , choosing $dm_2 = \pm 1$. This allows us to solve the system of N+1 equations and variables:

$$\begin{bmatrix} D_x\mathbf{H}(\mathbf{x},\mathbf{M}) & D_{m_1}\mathbf{H}(\mathbf{x},\mathbf{M}) \\ D_x\lambda_c(\mathbf{x},\mathbf{M}) & D_{m_1}\lambda_c(\mathbf{x},\mathbf{M}) \end{bmatrix} \begin{bmatrix} d\mathbf{x} \\ dm_1 \end{bmatrix} = - \begin{bmatrix} D_{m_2}\mathbf{H}(\mathbf{x},\mathbf{M}) \\ D_{m_2}\lambda_c(\mathbf{x},\mathbf{M}) \end{bmatrix} dm_2 \tag{B.45}$$

Note: For equilibrium solutions λ_c should be substituted with $\mathrm{Re}[\lambda_c]$.

Normalizing the vector $d\gamma^p = ||\; [d\mathbf{x}^T \; d\mathbf{M}]^T|| = 1$ and taking a step h to the predictor point $\gamma^p = [\mathbf{x}^T \; \mathbf{M}^T]^T$. We use the following NR-iteration scheme as a corrector:

$$\begin{bmatrix} \mathbf{D}\mathbf{H}(\gamma_i^c) \\ \mathbf{D}\Lambda(\gamma_i^c) \\ d\gamma^{p^T} \end{bmatrix} d\gamma^c = \begin{bmatrix} -\mathbf{H}(\gamma_i^c) \\ -\mathbf{H}_\Lambda(\gamma_i^c) \\ 0 \end{bmatrix} \tag{B.46}$$

Where $\mathbf{D}\Lambda$ and $\mathbf{H}_\Lambda(\gamma_i^c)$ are defined by

$$\mathbf{D}\Lambda = \begin{cases} [D_x\mathrm{Re}[\lambda_c(\gamma_i^c)] \;\; D_{\mathbf{M}}\mathrm{Re}[\lambda_c(\gamma_i^c)]]\,, & \text{for equlibrium solutions} \\ [D_x\lambda_c(\gamma_i^c) \;\; D_{\mathbf{M}}\lambda_c(\gamma_i^c)]\,, & \text{for periodic solutions} \end{cases} \tag{B.47}$$

and

$$\mathbf{H}_\Lambda(\gamma_i^c) = \begin{cases} \mathrm{Re}[\lambda_c(\gamma_i^c)], & \text{for equlibrium solutions} \\ \lambda_c(\gamma_i^c) - 1, & \text{for periodic solutions} \end{cases} \tag{B.48}$$

γ_{i+1}^c is determined from $\gamma_{i+1}^c = \gamma_i^c + d\gamma$.

It might seem as if 2D continuation is easy to control, and in some cases it does indeed easily travel the bifurcation curves. But one should not be surprised if in some cases it is difficult to force the method along one's specified direction. This is mainly because our attempt to control the travel direction, through the predictor step, can be 'overruled' by the NR-method. Furthermore, the NR-method may have a lot of problems when bifurcation curves lie close in the system space. Here it really has to struggle in an attempt to convert. This is due to the fact that NR is jumping between the neighborhoods of the different solutions.

One can only try to adjust step-length and tolerances in order to help 2D continuations past its problems, but these might have to be adjusted several places along a bifurcation curve.

References

[Aronson et al., 1986] Aronson, D.G., McGhee, R.P., Kevrekidis, I.G., and Aris, R., *Entrainment Regions for Periodically Forced Oscillators*, Physical Review A, Vol. 33, No. 3, pp. 2190-2192, 1986.

[Baesens and Nicolis, 1983] Baesens, C. and Nicolis, G., *Complex Bifurcations in a Periodically Forced Normal Form*, Condensed Matter, Vol. 52, No. 4, pp. 345-354, 1983.

[Bryant and Jeffries, 1987] Bryant, P. and Jeffries, C., *The Dynamics of Phase Locking and Points of Resonance in a Forced Magnetic Oscillator*, Physica, Vol. 25D, Nos. 1-3, pp. 196-232, 1987.

[Enright et al., 1986] Enright, W.E. et al., *Interpolants for Runge-Kutta Formulars*, ACM, Transactions on Mathematical Software, Vol. 12, #3, pp.193-218, 1986.

[Glass and Sun, 1994] Glass, L. and Sun, J., *Periodic Forcing of a Limit-Cycle Oscillator: Fixed Points, Arnold Tongues, and the Global Organization of Bifurcations*, Physical Review E, Vol. 50, No. 6, pp. 5077-5084, 1994.

[Guckenheimer and Holmes, 1986] Guckenheimer, J. and Holmes, P., *Nonlinear Oscillations, Dynamical Systems, and Bifurcations of Vector Fields*, Applied Mathematical Sciences, Springer-Verlag, New York, 2nd edition, 1986.

[Kampmann, 1995] Kampmann, C.E., *Note on Numerical Integration of Ordinary Differential Equations*, Notes from 1293, Tech. Uni. of Denmark, 1995.

[Kevrekidis et al., 1986] Kevrekidis, I.G., Schmidt, L.D., and Aris, R., *Some Common Features of Periodically Forced Reacting Systems*, Chemical Engineering Science, Vol. 41, No. 5, pp. 1263- 1276, 1986.

[Knudsen et al., 1991] Knudsen, C., Sturis J., and Thomsen J. S., *Generic bifurcation sturctures of Arnol'd tongues in forced oscillators*, Physical Review A, Vol. 44, No. 6, pp. 3503-3510, 1991.

[Lambert et al., 1990] Lambert, J.D., et al. *Numerical Methods for Ordinarey Differential Systems*, J.Wiley & Sons, 1991.

[Mosekilde et al., 1990] Mosekilde, E., Feldberg, R., Knudsen, C., Hindsholm, M., *Mode locking and spatiotemporal chaos in periodically driven Gunn diodes*, Physical Review B, vol 41-4, pp. 2298-2306, 1990.

[Mosekilde and Feldberg, 1994] Mosekilde, Erik and Rasmus Feldberg, *Ikke-lineær Dynamik og Kaos*, Polyteknisk Forlag, 1994.

[Norris, 1993] Norris, J.W., *The Closing of Arnol'd Tongues for a Periodically Forced Limit Cycle*, Nonlinearity, Vol. 6, No. 6, pp. 1093-1114, 1993.

[Nayfeh and Balachandran, 1995] Nayfeh, Ali H. and Balachandran,Balakumar., *Applied nonlinear dynamics; Analytical, Computational and Experimantal Methods*, Wiley series in Nonlinear Science, 1995.

[Olesen and Knudsen, 1994] Olesen, M. and Kudsen, C., *Destruction of Dominant Arnol'd Tongues in Forced Oscillators*, International Journal of Bifurcation and Chaos, Vol. 4, No. 3, pp. 737-739, 1994.

[Ott, 1994] Ott, E., *Chaos in dynamical systmes*, Cambridge University Press, 1994.

[Parker and Chua, 1989] Parker T.S., Chua L.O., *Practical Numerical Algorithms for Chaotic Systems*, Springer-Verlag, 1989.

[Pavlou and Kevrekidis, 1992] Pavlou, S. and Kevrekidis I.G., *Microbial Predation in a Periodically Operated Chemostat: A Global Study of the Interaction Between Natural and Externally Imposed Frequencies*, Mathematical Biosciences, Vol. 108, pp. 1-55, 1992.

[Press et. al, 1992] Press, William H., William T. Vetterling, Saul A. Teukolsky, and Brian P. Flannery, *Numerical Recipes in C*, Cambridge University Press, 1992.

[Sturis et al., 1995] Sturis, J., Knudsen, C., O'Meara, N.M., Thomsen, J.S., Mosekilde, E., Van Cauter, E., and Polonsky, K.S., *Phase-locking Regions in a Forced Model of Slow Insulin and Glucose Oscillations*, Chaos, Vol. 5, No. 1, 1995.

[Sørensen et al., 1996] Sørensen, C.B., Mosekilde, E., and Granasy, P., *Nonlinear Dynamics of a Vectored Thrust Aircraft*, Physica Scripta, Vol. T67, pp. 176-183, 1996.

[Taylor and Kevrekidis, 1991] Taylor, M.A. and Kevrekidis, I.G., *Some Common Dynamic Features of Coupled Reacting Systems*, Physica, Vol. D 51, pp. 274-292, 1991.

[Thompson and Stewart, 1986] Thompson, J.M.T & Stewart, H.B., *Nonlinear Dynamics and Chaos*, Wiley Interscience, 1986.

[Tsarouhas and Ross, 1987] Tsarouhas, G.E. and Ross, J., *Explicit Solutions of Normal Form of Driven Oscillatory Systems*, The Journal of Chemical Physics, Vol. 87, No. 11, pp. 6538-6543, 1987.

[Tsarouhas and Ross, 1988] Tsarouhas, G.E. and Ross, J., *Explicit Solutions of Normal Form of Driven Oscillatory Systems in Entrainment Bands*, The Journal of Chemical Physics, Vol. 89, No. 9, pp. 5715-5720, 1988.

[Tsarouhas and Ross, 1989] Tsarouhas, G.E. and Ross, J., *Critical Slowing Down, Phase Relations, and Dissipation in Driven Oscillatory Systems*, The Journal of Physical Chemistry, Vol. 93, No. 7, pp. 2833-2836, 1989.

[Vance et al., 1989] Vance, W., Tsarouhas, G.E., and Ross, J., *Universal Bifurcation Structures of Forced Oscillators*, Progress of Theoretical Physics Supplement, No. 99, pp. 331-338, 1989.

[Vance and Ross, 1989] Vance, W. and Ross, J., *A Detailed Study of a Forced Chemical Oscillator: Arnol'd Tongues and Bifurcation Sets*, The Journal of Chemical Physics, Vol. 91, No. 12, pp. 7654-7670, 1989.